AEDC-TR-73-126
AFATL-TR-73-150

Cy. 1

EXPERIMENTAL MAGNUS CHARACTERISTICS OF BALLISTIC PROJECTILES WITH ANTI-MAGNUS VANES AT MACH NUMBERS 0.7 THROUGH 2.5

Leroy M. Jenke and Jack B. Carman

ARO, Inc.

December 1973

PROPULSION WIND TUNNEL FACILITY
ARNOLD ENGINEERING DEVELOPMENT CENTER
AIR FORCE SYSTEMS COMMAND
ARNOLD AIR FORCE STATION, TENNESSEE

NOTICES

When U. S. Government drawings specifications, or other data are used for any purpose other than a definitely related Government procurement operation, the Government thereby incurs no responsibility nor any obligation whatsoever, and the fact that the Government may have formulated, furnished, or in any way supplied the said drawings, specifications, or other data, is not to be regarded by implication or otherwise, or in any manner licensing the holder or any other person or corporation, or conveying any rights or permission to manufacture, use, or sell any patented invention that may in any way be related thereto.

Qualified users may obtain copies of this report from the Defense Documentation Center.

References to named commercial products in this report are not to be considered in any sense as an endorsement of the product by the United States Air Force or the Government.

EXPERIMENTAL MAGNUS CHARACTERISTICS OF BALLISTIC PROJECTILES WITH ANTI-MAGNUS VANES AT MACH NUMBERS 0.7 THROUGH 2.5

Leroy M. Jenke and Jack B. Carman
ARO, Inc.

FOREWORD

The work reported herein was conducted by the Arnold Engineering Development Center (AEDC) for the Naval Weapons Laboratory (NWL) under sponsorship of the Air Force Armament Laboratory (AFATL), Air Force Systems Command (AFSC), under Program Element 62602F, Project 2547. AFATL Project Monitor was Mr. E. Sears.

The results presented herein were obtained by ARO, Inc. (a subsidiary of Sverdrup & Parcel and Associates, Inc.), contract operator of AEDC, AFSC, Arnold Air Force Station, Tennessee. The tests were conducted from February 26 through March 15, 1973, under ARO Project Number PA298. The final data analysis was completed on April 25, 1973, and the manuscript was submitted for publication on May 18, 1973.

This technical report has been reviewed and is approved.

L. R. KISSLING
Lt Colonel, USAF
Chief Air Force Test Director, PWT
Directorate of Test

FRANK J. PASSARELLO
Colonel, USAF
Director of Test

ABSTRACT

An experimental investigation was conducted to determine static-stability and Magnus characteristics of three spin-stabilized ballistic shell configurations with small anti-Magnus vanes on the boattail. The models (slightly larger than full scale) were tested at Mach numbers 0.7 through 2.5 over an angle-of-attack range from -2 to 8 deg. The Reynolds number, based on a model diameter of 5.2 in., was 1×10^6 (for M_∞ = 0.7 to 1.3) and 1.7×10^6 (for M_∞ = 1.76 to 2.5), and the spin parameter ($pd/2V_\infty$) ranged from 0 to 0.4 radians. Results are presented showing the effects of spin, Mach number, angle of attack, and anti-Magnus vanes. These results show that the vanes were effective in reducing both Magnus force and moment for two of the basic configurations and that the canted (7.2-deg) vanes were more effective than the straight vanes.

CONTENTS

		Page
	ABSTRACT	iii
	NOMENCLATURE	viii
I.	INTRODUCTION	1
II.	APPARATUS AND PROCEDURE	
	2.1 Test Articles and Test Mechanism	1
	2.2 Test Facilities	2
	2.3 Instrumentation	3
	2.4 Test Procedure	3
III.	TEST CONDITIONS AND DATA PRECISION	
	3.1 Test Conditions	4
	3.2 Data Precision	5
IV.	RESULTS AND DISCUSSION	6
V.	CONCLUDING REMARKS	8
	REFERENCES	9

APPENDIX
Illustrations

Figure

1.	Model Photographs	
	a. Tunnel 4T Installation	13
	b. Complete Configurations	14
	c. Knurl Pattern	15
2.	Model Details	
	a. Configuration 0	16
	b. Configuration 2	17
	c. Configuration 3	18
	d. Anti-Magnus Vanes	19
3.	Magnus-Force Test Mechanism	20
4.	Balance Details	21
5.	Variation of C_N and C_m with Angle of Attack, Configuration 0	
	a. Without Vanes	22
	b. With Four Canted Vanes	23
	c. With Eight Straight Vanes	24
	d. With Eight Canted Vanes	25

Figure | Page

6. Variation of C_N and C_m with Angle of Attack, Configuration 2
   a. With Eight Straight Vanes 26
   b. With Eight Canted Vanes 27
7. Variation of C_N and C_m with Angle of Attack, Configuration 3
   a. Without Vanes. 28
   b. With Eight Canted Vanes 29
8. Variation of C_{N_α} and C_{m_α} with Mach Number
   a. Configuration 0 30
   b. Configuration 2 31
   c. Configuration 3 32
9. Typical Variation of C_Y and C_n with $pd/2V_\infty$, $M_\infty = 1.76$ 33
10. Variation of C_Y and C_n with $pd/2V_\infty$ for Configuration 0 without Vanes
    a. $M_\infty = 1.0$ 34
    b. $M_\infty = 1.2$ 35
11. Variation of C_Y and C_n with $pd/2V_\infty$ for Configuration 0 with Four Canted Vanes
    a. $M_\infty = 1.0$ 36
    b. $M_\infty = 1.2$ 37
12. Variation of C_Y and C_n with $pd/2V_\infty$ for Configuration 0 with Eight Straight Vanes
    a. $M_\infty = 0.9$ 38
    b. $M_\infty = 1.0$ 39
    c. $M_\infty = 1.1$ 40
    d. $M_\infty = 1.2$ 41
    e. $M_\infty = 1.3$ 42
13. Variation of C_Y and C_n with $pd/2V_\infty$ for Configuration 0 with Eight Canted Vanes
    a. $M_\infty = 0.9$ 43
    b. $M_\infty = 1.0$ 44
    c. $M_\infty = 1.1$ 45
    d. $M_\infty = 1.2$ 46

Figure | Page

13. (Continued)
e. M_∞ = 1.3 47
f. M_∞ = 1.76 48
g. M_∞ = 2.50 49

14. Variation of C_Y and C_n with $pd/2V_\infty$ for Configuration 2 with Eight Straight Vanes
a. M_∞ = 0.9 50
b. M_∞ = 1.0 51
c. M_∞ = 1.1 52
d. M_∞ = 1.2 53
e. M_∞ = 1.3 54

15. Variation of C_Y and C_n with $pd/2V_\infty$ for Configuration 2 with Eight Canted Vanes
a. M_∞ = 0.7 55
b. M_∞ = 0.9 56
c. M_∞ = 1.0 57
d. M_∞ = 1.1 58
e. M_∞ = 1.2 59
f. M_∞ = 1.3 60

16. Variation of C_Y and C_n with $pd/2V_\infty$ for Configuration 3 without Vanes
a. M_∞ = 0.9 61
b. M_∞ = 1.2 62
c. M_∞ = 1.3 63

17. Variation of C_Y and C_n with $pd/2V_\infty$ for Configuration 3 with Eight Canted Vanes
a. M_∞ = 0.9 64
b. M_∞ = 1.0 65
c. M_∞ = 1.1 66
d. M_∞ = 1.2 67
e. M_∞ = 1.3 68

18. Variation of C_{Y_p} and C_{n_p} with Angle of Attack for Configuration 0
a. Without Vanes 69
b. With Four Canted Vanes 70
c. With Eight Straight Vanes 71
d. With Eight Canted Vanes 72

Figure		Page
19.	Variation of C_{Y_p} and C_{n_p} with Angle of Attack for Configuration 2	
	a. With Eight Straight Vanes.	73
	b. With Eight Canted Vanes	74
20.	Variation of C_{Y_p} and C_{n_p} with Angle of Attack for Configuration 3	
	a. Without Vanes	75
	b. With Eight Canted Vanes	76
21.	Variation of $C_{Y_{p_\alpha}}$ and $C_{n_{p_\alpha}}$ with Mach Number	
	a. Configuration 0	77
	b. Configuration 2	78
	c. Configuration 3	79
22.	Comparison of the Variation of $C_{Y_{p_\alpha}}$ and $C_{n_{p_\alpha}}$ with Mach Number for Configurations with Eight Canted Vanes	80
23.	Onset of Transition on the Leeward Surface of Configuration 0 at Supersonic Mach Numbers in Tunnel A	81
24.	Typical Shadowgraph of Configuration 0 at $M_\infty = 1.76$, $\alpha = 6.37$ deg (Tunnel A)	82

NOMENCLATURE

A	Reference area, model maximum cross-sectional area (see Fig. 2), $in.^2$
C_m	Pitching-moment coefficient, pitching moment/$q_\infty Ad$
C_{m_α}	Pitching-moment coefficient derivative, $\partial C_m/\partial\alpha$, per deg
C_N	Normal-force coefficient, normal force/$q_\infty A$
C_{N_α}	Normal-force coefficient derivative, $\partial C_N/\partial\alpha$, per deg
C_n	Yawing- (Magnus-) moment coefficient, yawing moment/$q_\infty Ad$ (see Fig. 2)
C_{n_p}	Magnus-moment spin derivative coefficient for $(pd/2V_\infty) < 0.15$, $\partial^2 C_n/\partial(pd/2V_\infty)$, per radian

$C_{n_{p_\alpha}}$	Magnus-moment coefficient derivative, $\partial^2 C_n / \partial(pd/2V_\infty)\partial\alpha$, per radian^2
C_Y	Side-(Magnus) force coefficient, side force/$q_\infty A$ (see Fig. 2)
C_{Y_p}	Magnus-force spin derivative coefficient for $(pd/2V_\infty) < 0.15$, $\partial C_Y / \partial(pd/2V_\infty)$, per radian
$C_{Y_{p_\alpha}}$	Magnus-force coefficient derivative, $\partial^2 C_Y / \partial(pd/2V_\infty)\partial\alpha$, per radian^2
d	Reference diameter, model maximum diameter (see Fig. 2), in.
M_∞	Free-stream Mach number
p	Model spin rate (positive, clockwise viewing from the base), radians/sec
$pd/2V_\infty$	Spin parameter, radians
p_o	Tunnel stilling chamber pressure, psia
q_∞	Free-stream dynamic pressure, psia
Re	Free-stream unit Reynolds number, ft^{-1}
T_o	Tunnel stilling chamber temperature, °R
V_∞	Free-stream velocity, ft/sec
x_t	Axial distance from model nose to onset of transition, in.
α	Angle of attack, deg

SECTION I
INTRODUCTION

The present test was conducted as part of a continuing investigation by the Naval Weapons Laboratory (NWL) for development work on ballistic shells. These projectiles are not statically stable and must be spin-stabilized. The spin velocity tends to induce Magnus effects, which can lead to dynamic instabilities. Both of these factors will influence the flight path. This test was initiated to obtain Magnus-force and -moment and static-stability data on three configurations with small anti-Magnus vanes (vanes to reduce the Magnus forces). The results will be used in estimating the performance of actual projectiles. Data were obtained at Mach numbers from 0.7 to 2.5 at Reynolds numbers, based on a model diameter of 5.2 in., of 1.0×10^6 and 1.7×10^6. The angle of attack was varied from -2 to 8 deg, and values of the spin parameter ($pd/2V_\infty$) ranged from 0 to 0.4 radians.

SECTION II
APPARATUS AND PROCEDURE

2.1 TEST ARTICLES AND TEST MECHANISM

The aluminum models were supplied by NWL and had been tested previously at AEDC. The models were modified for the anti-Magnus vanes, and model details are presented in Figs. 1 and 2, Appendix. The configurations of these projectiles have not been finalized, but the models are approximately full scale. Two sets of vanes (Fig. 2d) were supplied. One set (eight vanes) was canted 7.2 deg, and the other set had no cant angle; all were attached on the boattail of the models. The knurl pattern on the boattail portion of configuration 0 (Fig. 1c) is used on the actual projectiles to secure a plastic sabot which serves as the spin band to spin the projectile in the gun barrel. The plastic sabot is destroyed in the gun barrel and, therefore, is not included on the test models.

The models were mounted on the Magnus-force test mechanism shown in Fig. 3. Basically, the Magnus-force test mechanism has a sting-mounted, water-jacketed, four-component balance with a shell mounted on ball bearings over the water jacket. A two-stage, air-driven turbine is mounted inside the model mounting shell at a fixed

axial position near the forward end of the sting. The turbine is used to spin the model to some desired speed and then is disengaged with an air-operated sliding clutch to allow the model to spin freely on the ball bearings. It is estimated that the turbine will produce a starting torque of 50 in.-lb and a developed torque of approximately 100 in.-lb. The mechanism is designed to operate under normal-force loads up to 500 lb and axial-force loads of 125 lb and for a maximum spin rate of approximately 25,000 rpm.

2.2 TEST FACILITIES

Supersonic Wind Tunnel (A) is a continuous, closed-circuit, variable density wind tunnel with an automatically driven flexible-plate-type nozzle and a 40- by 40-in. test section. The tunnel can be operated at Mach numbers from 1.5 to 6 at maximum stagnation pressures from 29 to 200 psia, respectively, and stagnation temperatures up to 750°R (M_∞ = 6). Minimum operating pressures range from about one-tenth to one-twentieth of the maximum at each Mach number. In most instances, Mach number changes may be made without stopping the tunnel. The model can be injected into the tunnel for a test run and then retracted for model changes without stopping the tunnel flow.

The Aerodynamic Wind Tunnel (4T) is a closed-circuit, continuous flow, variable density tunnel capable of being operated at Mach numbers from 0.20 to 1.30. At all Mach numbers the stagnation pressure can be varied from about 2 to 27 psia. The test section is 48 in. square and 150 in. long with perforated, variable porosity (0.5 to 10 percent) walls. It is completely enclosed in a plenum chamber from which the air can be evacuated, allowing part of the tunnel airflow to be removed through the perforated walls of the test section. The wall perforations are 0.50-in.-diam holes inclined 60 deg from the normal to the wall surface. This design allows control of wave attenuation and blockage effects. Further control of wall interference effects can be accomplished by converging or diverging the top and bottom test section walls by as much as 0.50 deg. The tunnel model support system consists of a pitch sector, strut, and sting attachment receptacle, and the system has a pitch capability of from -12 to 28 deg with respect to the tunnel centerline.

2.3 INSTRUMENTATION

Model forces and moments were measured with the VKF four-component, moment-type, strain-gage balance shown in Fig. 4. The small outrigger side beams of the balance, with semiconductor strain gages, were used to obtain the sensitivity required to measure small side loads while maintaining adequate balance stiffness for the larger pitch loads. When a yawing moment is imposed on the balance, secondary bending moments are induced in the side beams. Thus, the outrigger beams act as mechanical amplifiers, and a normal-force to side-force capability ratio of 20 was achieved for a 500-lb normal-force loading. Before testing, static loads in each plane and combined static loads were applied to the balance, simulating the range of model loads anticipated for the test. The following uncertainties represent the bands for 95 percent of the measurement residuals based on differences between the applied loads and the corresponding values calculated from the final data reduction equations.

Balance Component	Design Load	Range of Static Loads	Measurement Uncertainty
Normal force, lb	500	0 to 100	±0.20
Pitching moment*, in.-lb	2500	0 to 200	±0.50
Side force, lb	25	0 to 16	±0.07
Yawing moment*, in.-lb	125	0 to 50	±0.10

*About balance forward moment bridge

The transfer distance to the model moment reference was measured with a precision of ±0.005 in.

2.4 TEST PROCEDURE

The test procedure was to prespin the model to the desired spin rate, disengage the clutch, and record data as the model spin rate decayed. For the models with canted vanes, some additional data were obtained by holding the model with the brake, releasing the brake, and taking data as the model spin rate increased. Model spin rates were monitored using an internally mounted photocell-diode tachometer.

SECTION III
TEST CONDITIONS AND DATA PRECISION

3.1 TEST CONDITIONS

The configurations tested and the corresponding test conditions are listed in the table below. (X indicates Magnus data generally obtained from α = -2 to 8 deg.)

	Configuration						
	0			2		3	
M_∞	No Vanes	8 Straight Vanes	4 Canted Vanes	8 Canted Vanes	8 Straight Vanes	8 Canted Vanes	No Vanes	8 Canted Vanes
0.70						X		
0.90		X		X	X	X	X	X
1.00	X	X	X	X	X	X	X	X
1.10		X		X	X	X		X
1.20	X	X	X	X	X	X	X	X
1.30		X		X	X	X	X	X
1.76				X				
2.50				X				

The nominal test conditions at which the tests were conducted are given below.

M_∞	p_o, psia	T_o, °R	q_∞, psia	V_∞, ft/sec	Re x 10^{-6}/ft
0.70	9.4	550	2.3	765	2.4
0.90	8.3	↓	2.8	960	↓
1.00	8.0		3.0	1049	
1.10	7.9		3.1	1134	
1.20	7.8		3.3	1215	
1.30	7.9	↓	3.4	1292	↓
1.76	14.7	560	5.9	1609	4.0
2.50	21.0	560	5.4	1939	4.0

3.2 DATA PRECISION

Uncertainties (bands which include 95 percent of the calibration data) in the basic tunnel parameters, p_o, T_o, and M_∞, were estimated from repeat calibrations of the instrumentation and from the repeatability and uniformity of the test section flow during tunnel calibration. These uncertainties were then used to estimate uncertainties in other free-stream properties, using the Taylor series method of error propagation, as follows:

	Uncertainty, percent					
M_∞	M_∞	p_o	T_o	q_∞	V_∞	Re
0.70	±1.00	±0.30	±0.75	±1.03	±0.75	±0.98
0.90	±0.72	↓	↓	±0.59	±0.56	±0.99
1.00	±0.55			±0.42	±0.47	±0.99
1.10	±0.73			±0.46	±0.57	±1.00
1.20	±1.00			±0.47	±0.74	±1.01
1.30	±1.30			±0.40	±0.94	±1.02
1.76	±0.70	±0.50	±0.36	±0.70	±0.51	±0.73
2.50	±0.30	±0.50	±0.36	±0.78	±0.30	±0.83

Measurements of the model pitch attitude, including the model-balance deflection, are precise within ±0.05 deg based on repeat calibrations. The rpm precision is estimated to be ±5 rpm.

The balance uncertainties listed in Section 2.3 were combined with uncertainties in the tunnel parameters, assuming a Taylor series error propagation, to estimate the precision of the aerodynamic coefficients. The following uncertainties are those that were computed for the test conditions at which most of the data were obtained:

	Coefficient Uncertainty			
M_∞	C_N	C_m	C_Y	C_n
0.70	±0.0023	±0.0035	±0.0014	±0.0008
0.90	±0.0020	±0.0028	±0.0012	±0.0007
1.00	±0.0020	±0.0027	±0.0011	±0.0006
1.10	±0.0020	±0.0023	±0.0011	±0.0006
1.20	±0.0025	±0.0020	±0.0010	±0.0006
1.30	±0.0023	±0.0019	±0.0010	±0.0006
1.76	±0.0028	±0.0030	±0.0006	±0.0006
2.50	±0.0030	±0.0030	±0.0006	±0.0005

Derivative Coefficient Uncertainty

M_∞	C_{N_α}, deg^{-1}	C_{m_α}, deg^{-1}	C_{Y_p}, rad^{-1}	C_{n_p}, rad^{-1}	$C_{Y_{p_\alpha}}$, rad^{-2}	$C_{n_{p_\alpha}}$, rad^{-2}
0.70	±0.0011	±0.0018	±0.009	±0.005	±0.26	±0.14
0.90	±0.0010	±0.0014	±0.008	±0.005	±0.23	±0.14
1.00	±0.0010	±0.0013	±0.007	±0.004	±0.20	±0.11
1.10	±0.0010	±0.0011	±0.007	±0.004	±0.20	±0.11
1.20	±0.0012	±0.0010	±0.007	±0.004	±0.20	±0.11
1.30	±0.0011	±0.0010	±0.007	±0.004	±0.20	±0.11
1.76	±0.0014	±0.0015	±0.004	±0.004	±0.12	±0.11
2.50	±0.0015	±0.0015	±0.004	±0.003	±0.12	±0.10

It should be noted that data repeatability, which is a measure of the random-type errors, was generally well within the maximum propagated uncertainties quoted.

SECTION IV
RESULTS AND DISCUSSION

These tests were conducted to determine static stability and the change in the Magnus force and moment produced by small vanes on the boattail of three ballistic shell configurations which were tested previously. Data were obtained at Mach numbers 0.7 through 2.5 for values of the spin parameter ($pd/2V_\infty$) up to 0.4 radians. The angle of attack ranged from -2 to 8 deg.

The variations of normal force (C_N) and pitching moment (C_m) with angle of attack are presented in Figs. 5, 6, and 7 for all configurations tested. Since gun-launched projectiles are spin-stabilized, they are all statically unstable, as expected. For angles of attack up to 6 deg, C_N and C_m are essentially linear functions of α. The variations of C_{N_α} and C_{m_α} with Mach number are shown in Fig. 8 for the three models. For configurations 0 and 2, C_{N_α} increased and C_{m_α} decreased with increasing Mach number for $M_\infty > 0.9$. For configuration 3, both C_{N_α} and C_{m_α} generally increased with increasing Mach number. As expected, the vanes increased C_{N_α} and decreased C_{m_α}, and the cant angle had no effect on either parameter.

Figure 9 presents the typical variation of C_Y and C_n with $pd/2V_\infty$ for configuration 0 with eight canted vanes at $M_\infty = 1.76$. The data typify the type of data, the amount of scatter, and the number of points that were obtained as the model spin rate changed. The data presented hereafter in this report show a computer fairing through the data points (a third-degree least-squares curve fit) instead of symbols for each data point. The complete C_Y and C_n versus $pd/2V_\infty$ results are presented in Figs. 10 through 17. It should be noted that some scatter exists in the data that were obtained at $M_\infty = 1.0$. This scatter was caused primarily by sting and sector vibration at this operating condition. The results generally indicate that both C_Y and C_n were nonlinear with $pd/2V_\infty$ at the higher angles of attack ($\alpha > 4$ deg) and higher spin rates ($pd/2V_\infty > 0.2$). In addition, the usual negative C_Y and positive C_n for positive values at $pd/2V_\infty$ and α were obtained for all configurations with the exception of configurations 0 and 2 with eight canted vanes (Figs. 13a and 15a).

The linear portion of the data (slopes of C_Y and C_n versus $pd/2V_\infty$ for $pd/2V_\infty < 0.15$) were used to examine the effects of angle of attack. These variations of C_{Y_p} and C_{n_p} with angle of attack are presented in Figs. 18 through 20. The results indicate that the magnitudes of both C_{Y_p} and C_{n_p} generally increased continuously with angle of attack and were linear up to about 2 deg, except for configuration 0 with eight canted vanes (Fig. 18d), which had negative C_{n_p} values at the lower angles of attack at $M_\infty = 0.9$. Thus, the canted vanes appreciably reduced the Magnus moment, and this is shown more effectively in Figs. 21 and 22. The results also show that the canted vanes caused rather erratic variations at the larger angles of attack. Figures 21 and 22 present the variation of $C_{Y_{p_\alpha}}$ and $C_{n_{p_\alpha}}$ with Mach number. The data for configurations 0 and 2 (Figs. 21a and b) show a peak in both $C_{Y_{p_\alpha}}$ and $C_{n_{p_\alpha}}$ near $M_\infty = 1$, whereas for configuration 3 (Fig. 21c), the magnitude of both parameters generally increased with Mach number ($M_\infty = 0.9$ through 1.3). The effectiveness of the vanes in decreasing the Magnus components on configurations 0 and 2 is clearly shown, with the eight canted vanes being the most effective. The vanes apparently reduced the body Magnus force by changing the flow pattern on the boattail. In addition, the axial force on the canted vanes produced a negative yawing moment at angle of attack (Ref. 1). However, for configuration 3 (Fig. 21c), the vanes had very little effect on the Magnus force and increased the Magnus moment. Apparently the vanes'

location on the forward portion of the long boattail reduced the local side force near the vanes but influenced the flow over the aft portion of the boattail such that there was a larger local side force there to give the larger yawing moment. Results from the present tests compare well with the vanes-off data obtained in the previous investigation. A comparison of the three models with the eight canted vanes is presented in Fig. 22. The results show that the smallest Magnus force and moment were obtained with configuration 0 and that $C_{n_{p\alpha}}$ was negative at $M_\infty = 0.9$.

Platou (Ref. 2) has shown that body Magnus characteristics are dependent on flow conditions in the boundary layer, and Pate and Schueler (Ref. 3) have shown that transition location is dominated by the aerodynamic noise present in wind tunnels and is a function of tunnel size, with the smaller tunnel having a shorter distance to transition from the model nose for a given unit Reynolds number and Mach number. Since the location of transition is a possible factor affecting Magnus characteristics on spinning models, the estimated location of transition on the model leeward side (from shadowgraph photographs) is presented in Fig. 23 for configuration 0 at $M_\infty = 1.76$ and 2.5 in Tunnel A. These data, although not complete, may be of benefit in the future in comparing the present data with those from other test facilities. A typical shadowgraph photograph showing the flow patterns at $M_\infty = 1.76$ is presented in Fig. 24.

SECTION V
CONCLUDING REMARKS

An investigation was conducted to determine the static-stability and Magnus characteristics of three Naval Weapons Laboratory ballistic shell configurations. The tests were conducted at Mach numbers 0.7 through 2.5 for an angle-of-attack range from -2 to 8 deg. Results were obtained at spin parameter ($pd/2V_\infty$) values up to 0.4 radians. The test results are summarized as follows:

1. For configurations 0 and 2, C_{N_α} increased and C_{m_α} decreased with increasing Mach number for $M_\infty > 0.9$. For configuration 3, both parameters generally increased with increasing Mach number.
2. The vanes increased C_{N_α} and decreased C_{m_α}.

3. Both C_Y and C_n were nonlinear with $pd/2V_\infty$ at the higher angles of attack ($\alpha \gtrsim 4$ deg) and $pd/2V_\infty$ values ($pd/2V_\infty \gtrsim 0.2$).
4. Generally, C_Y was negative and C_n was positive for positive values of $pd/2V_\infty$ and α.
5. The magnitudes of both C_{Y_p} and C_{n_p} increased with angle of attack and were linear up to about 2 deg.
6. For configurations 0 and 2, both C_{Y_p} and C_{n_p} were a maximum near $M_\infty = 1$, whereas for configuration 3 the magnitude of both parameters generally increased with Mach number ($M_\infty = 0.9$ to 1.3).
7. The vanes reduced the Magnus force and moment on configurations 0 and 2, but increased the Magnus moment on configuration 3.
8. The canted vanes were more effective in reducing the Magnus forces than were the straight vanes.

REFERENCES

1. Benton, Edward R. "Supersonic Magnus Effect on a Finned Missile." AIAA Journal, Vol. 2, No. 1, January 1964, pp. 153-155.
2. Platou, A. S. "The Magnus Force on a Short Body at Supersonic Speeds." BRL Report No. 1062 (AD212064), January 1959.
3. Pate, S. R. and Schueler, C. J. "Effects of Radiated Aerodynamic Noise on Model Boundary-Layer Transition in Supersonic and Hypersonic Wind Tunnels." AEDC-TR-67-236 (AD666644), March 1968. Also AIAA Journal, Vol. 7, No. 3, March 1969, pp. 450-457.

APPENDIX
ILLUSTRATIONS

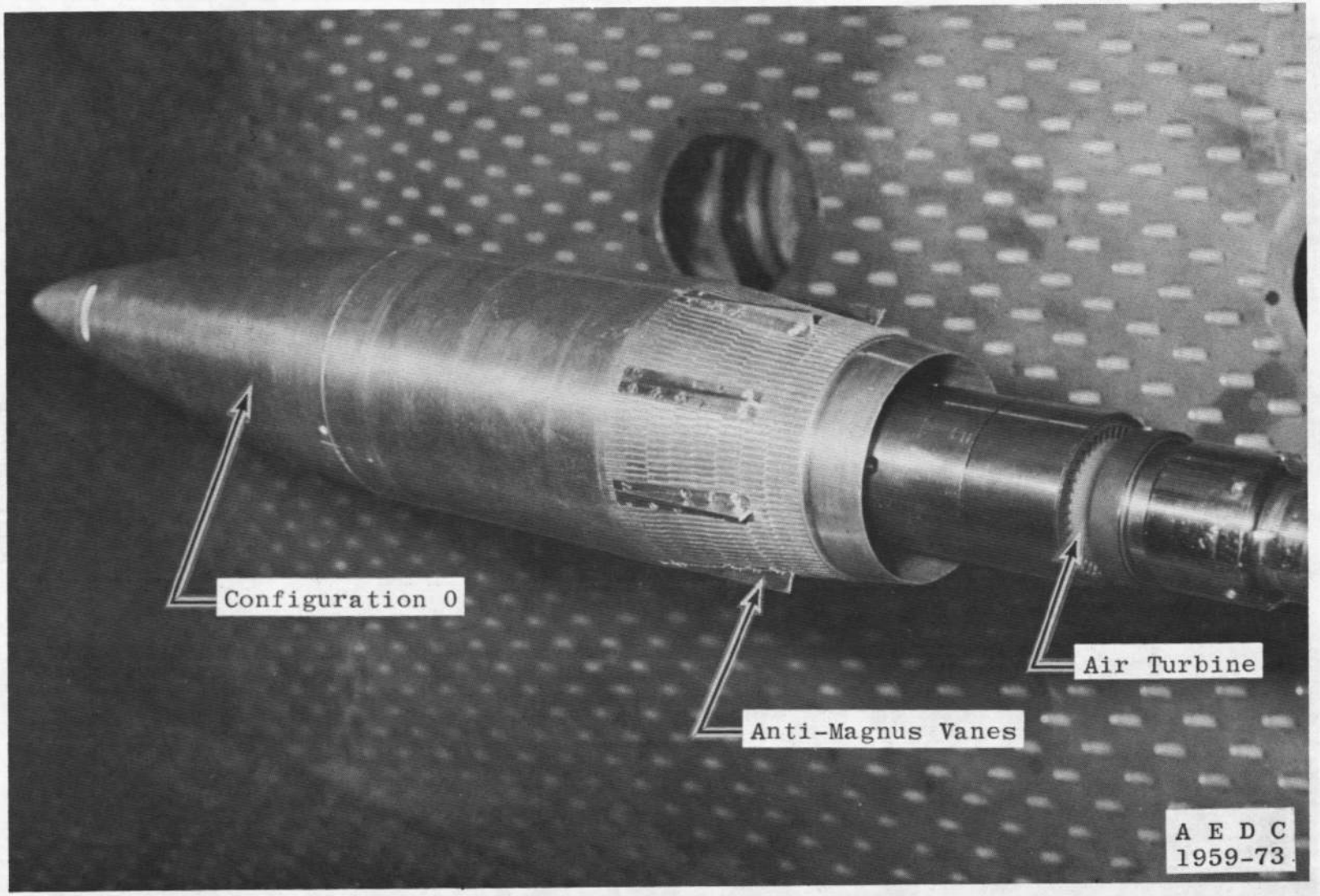

a. Tunnel 4T Installation

Fig. 1 Model Photographs

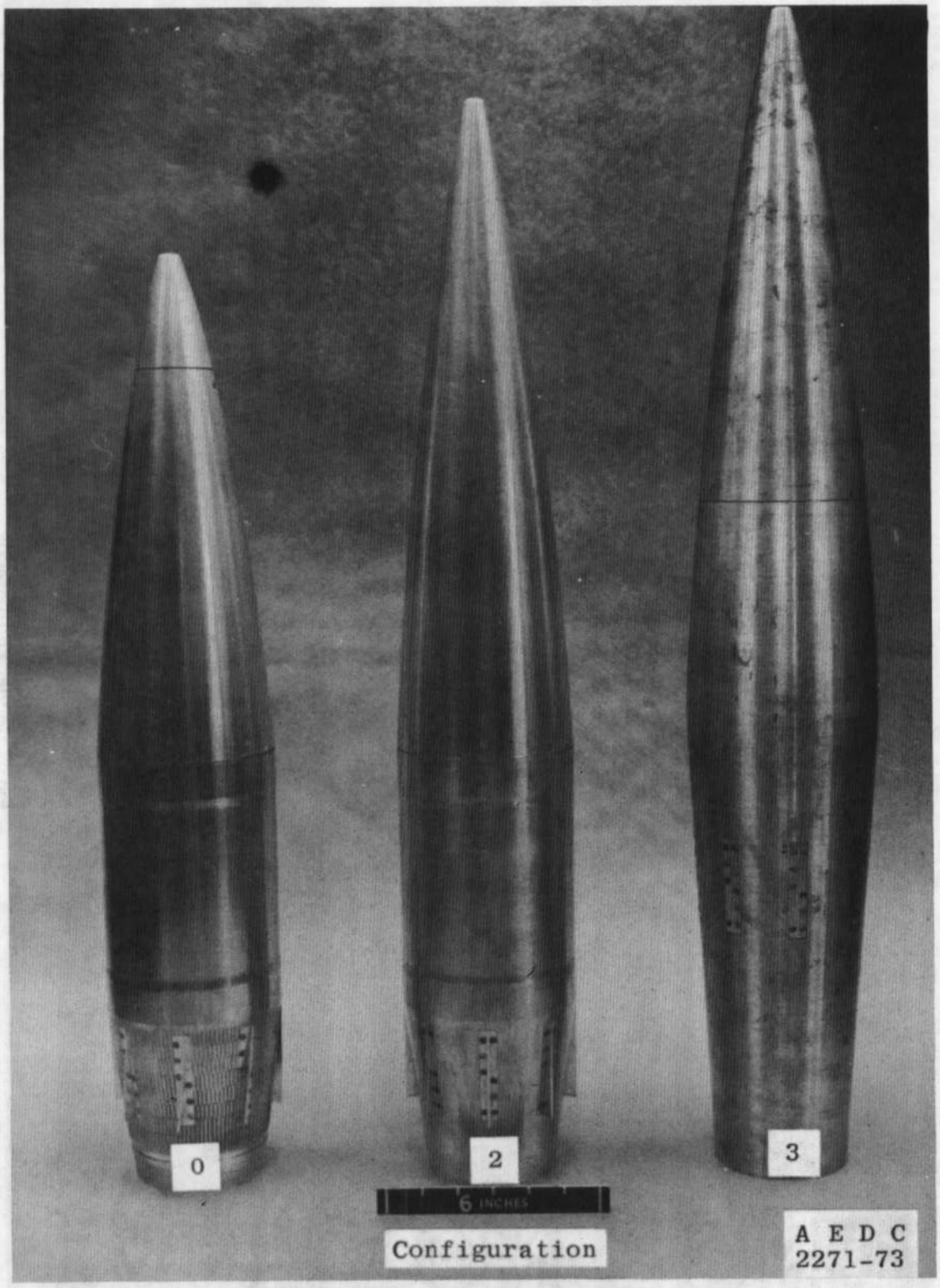

b. Complete Configurations
Fig. 1 Continued

c. Knurl Pattern
Fig. 1 Concluded

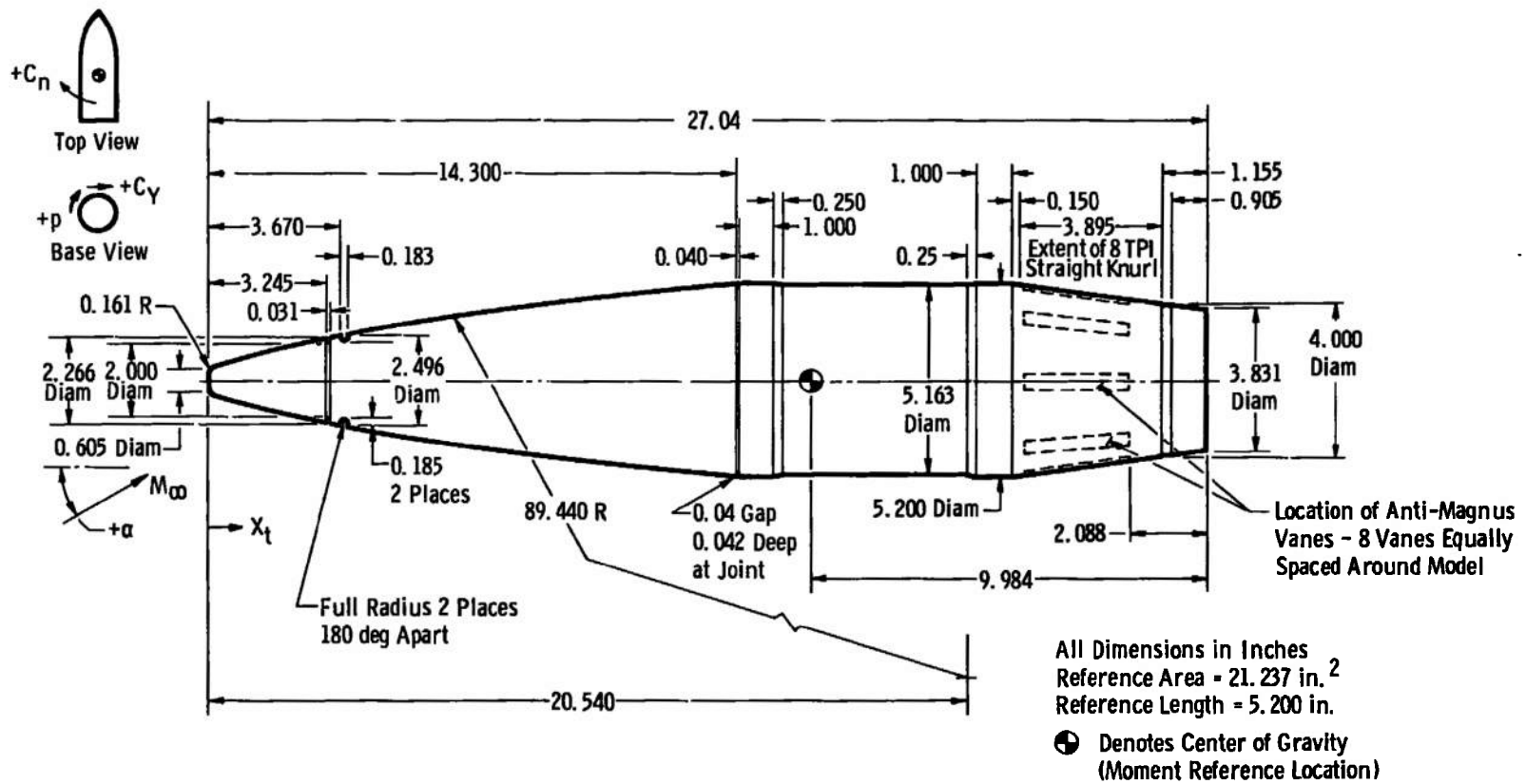

a. Configuration 0

Fig. 2 Model Details

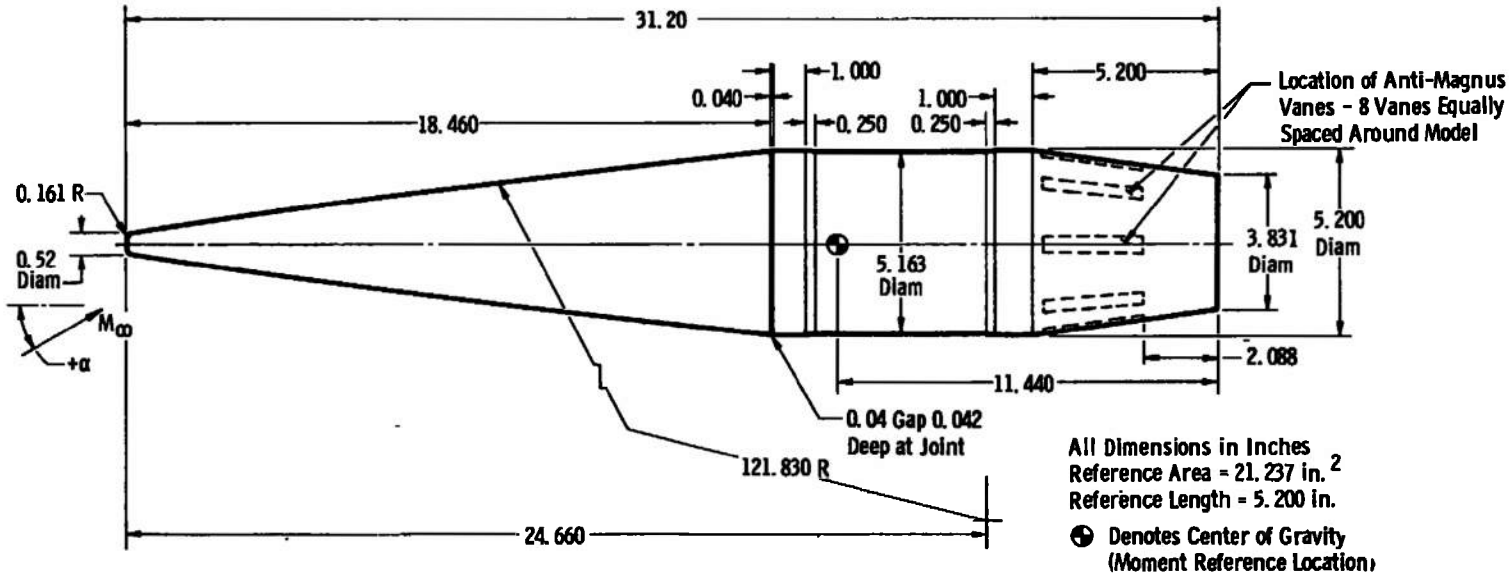

b. Configuration 2
Fig. 2 Continued

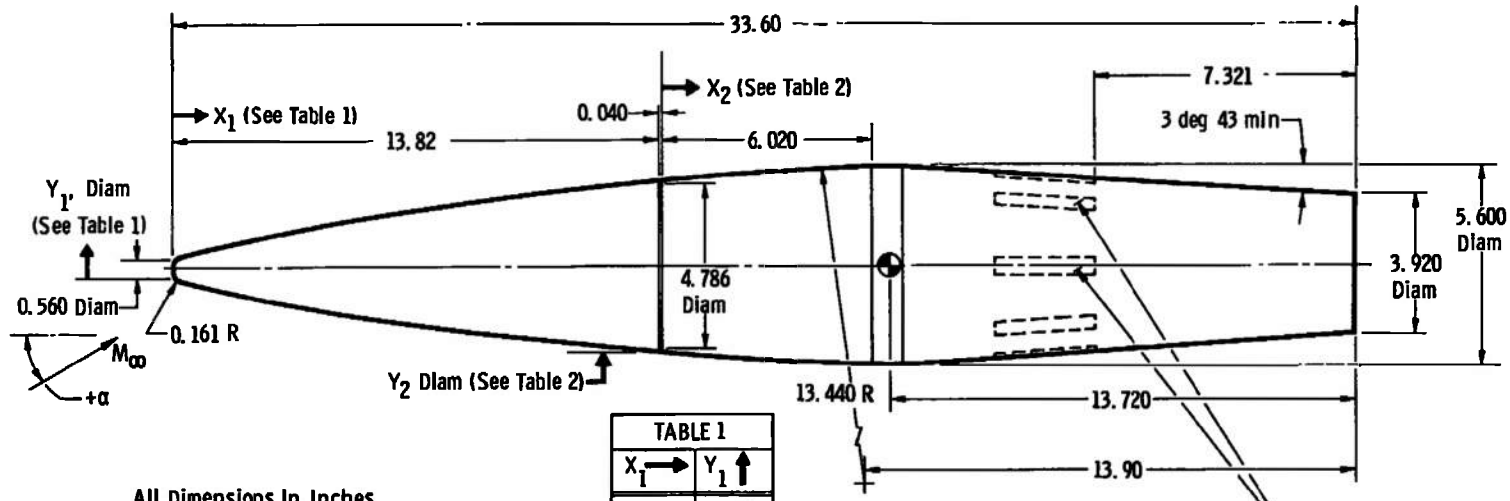

All Dimensions In Inches
Reference Area = 24.630 in.^{2}
Reference Length = 5.600 in.

Denotes Center of Gravity
(Moment Reference Location)

TABLE 1

X_1 →	Y_1 ↑
0	0.560
1.000	1.098
2.000	1.546
3.000	1.946
4.000	2.312
5.000	2.650
6.000	2.966
7.000	3.264
8.000	3.542
9.000	3.804
10.000	4.050
11.000	4.281
12.000	4.500
13.000	4.702
13.820	4.856

TABLE 2

X_2 →	Y_2 ↑
0	4.860
0.140	4.890
1.140	5.060
2.140	5.216
3.140	5.352
4.140	5.468
5.140	5.556
6.020	5.600

c. Configuration 3
Fig. 2 Continued

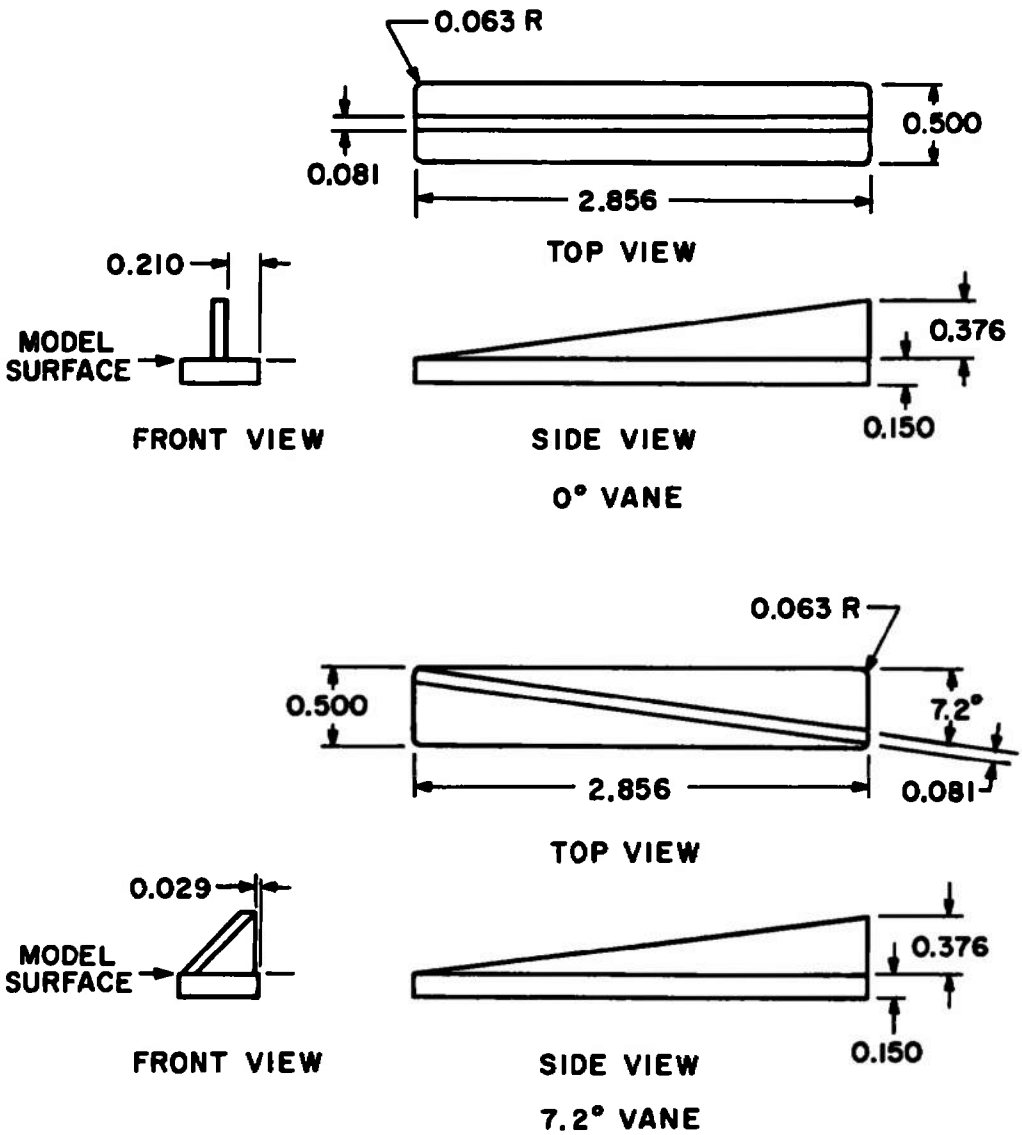

ALL DIMENSIONS IN INCHES

d. Anti-Magnus Vanes
Fig. 2 Concluded

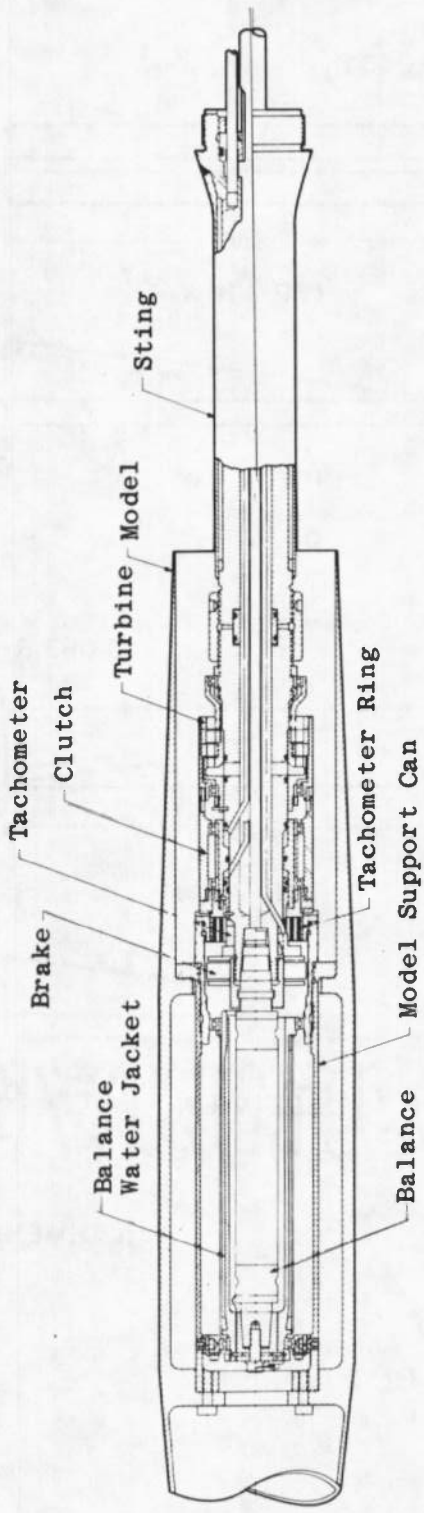

Fig. 3 Magnus-Force Test Mechanism

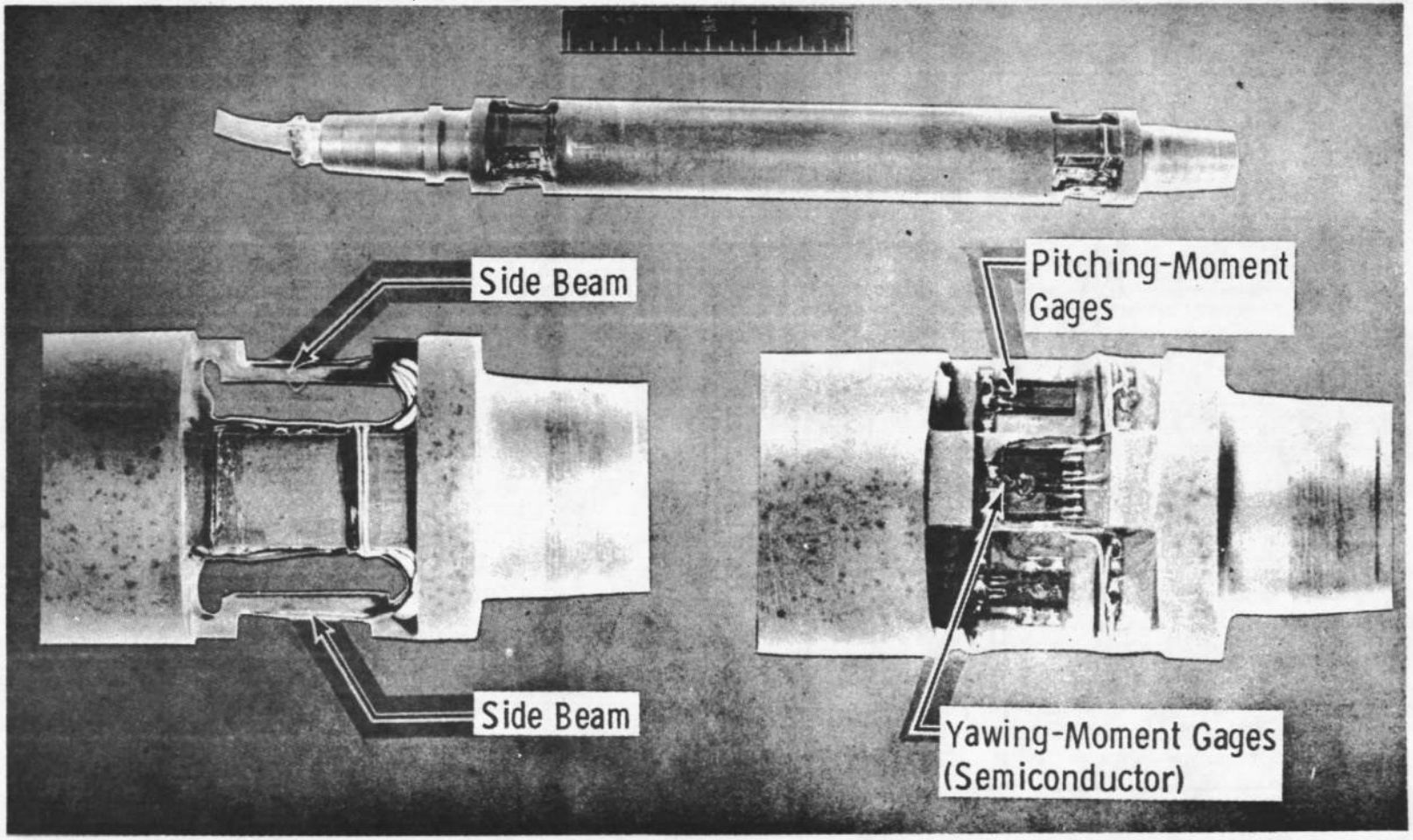

Fig. 4 Balance Details

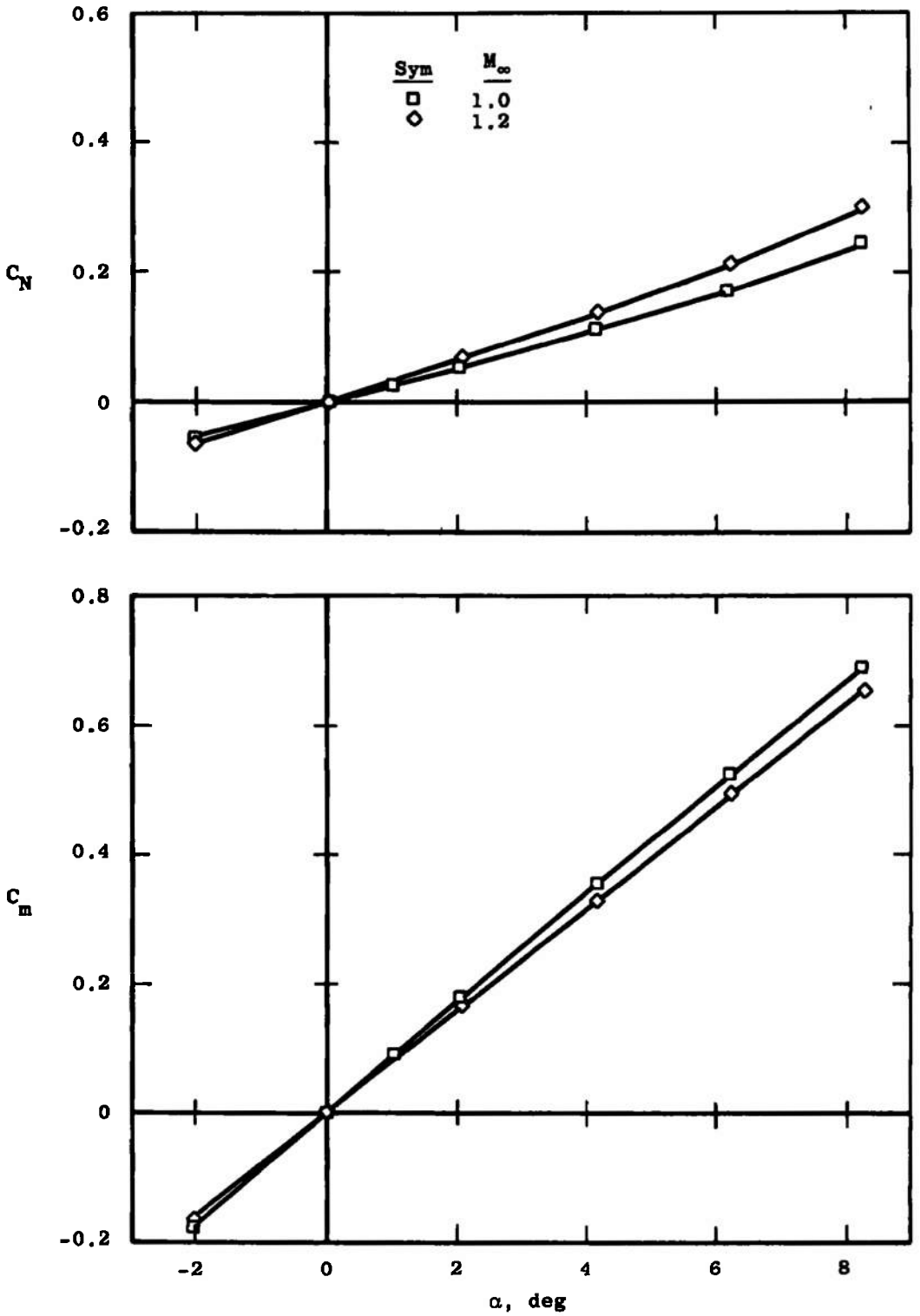

a. Without Vanes

Fig. 5 Variation of C_N and C_m with Angle of Attack, Configuration 0

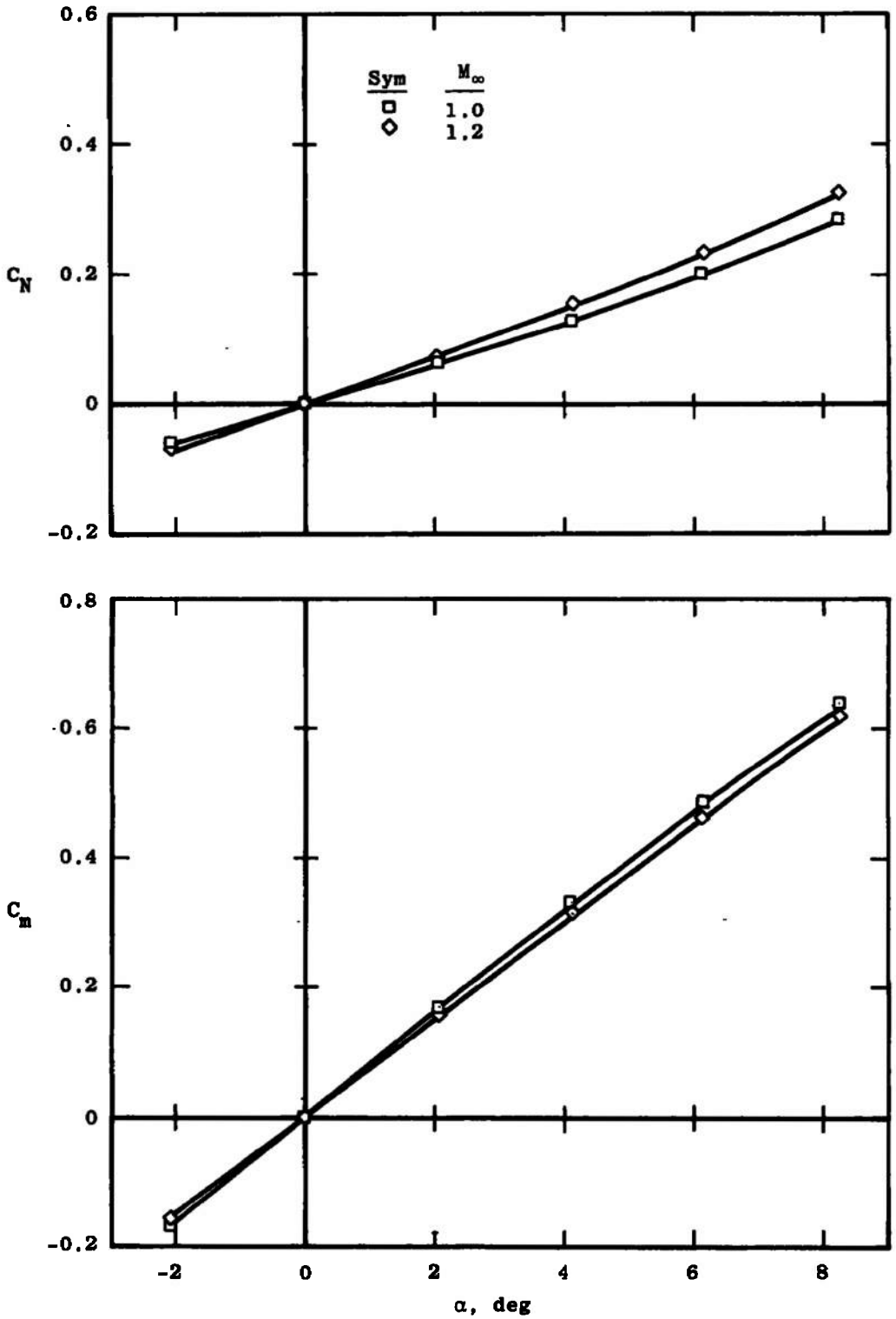

b. With Four Canted Vanes
Fig. 5 Continued

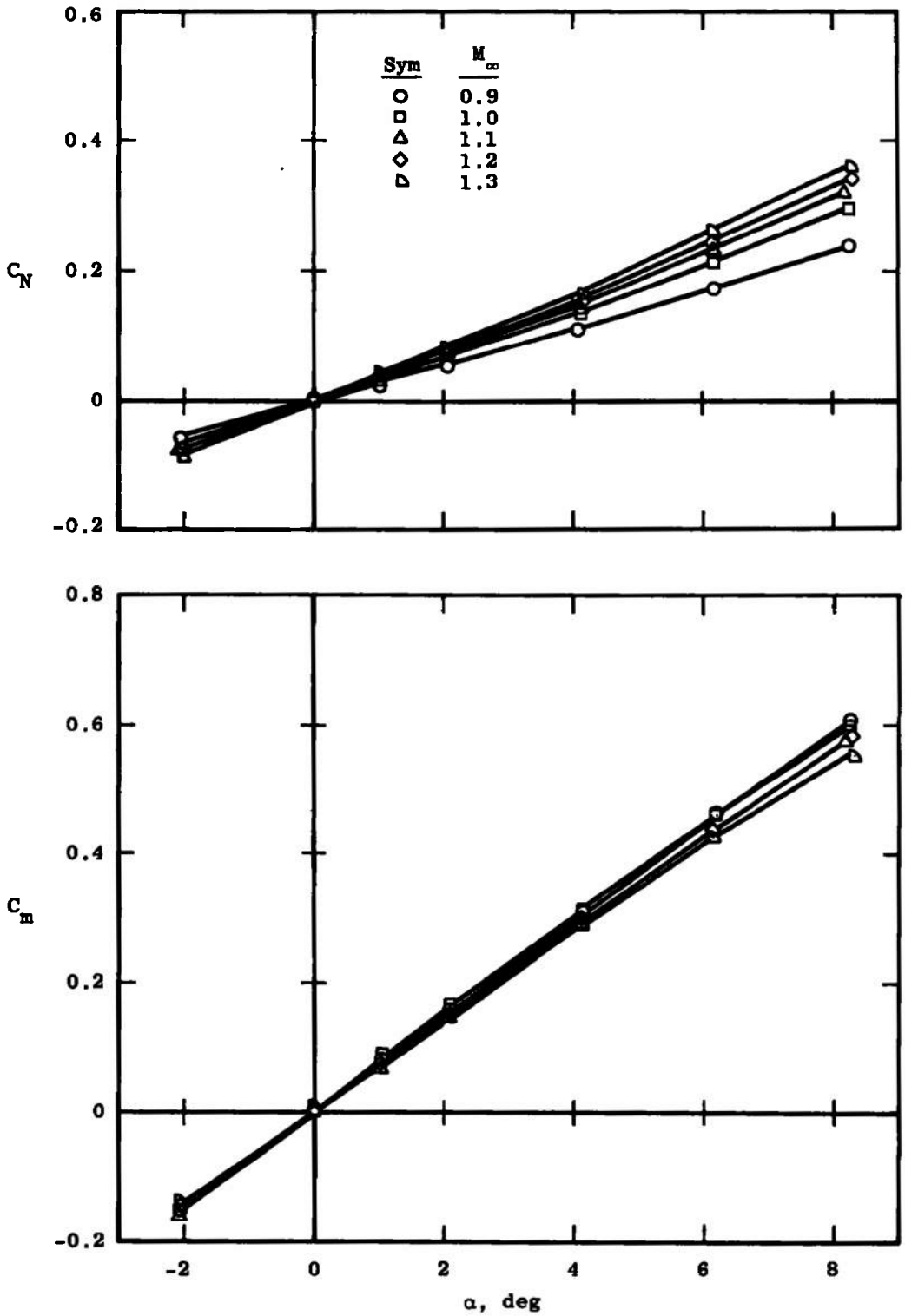

c. With Eight Straight Vanes
Fig. 5 Continued

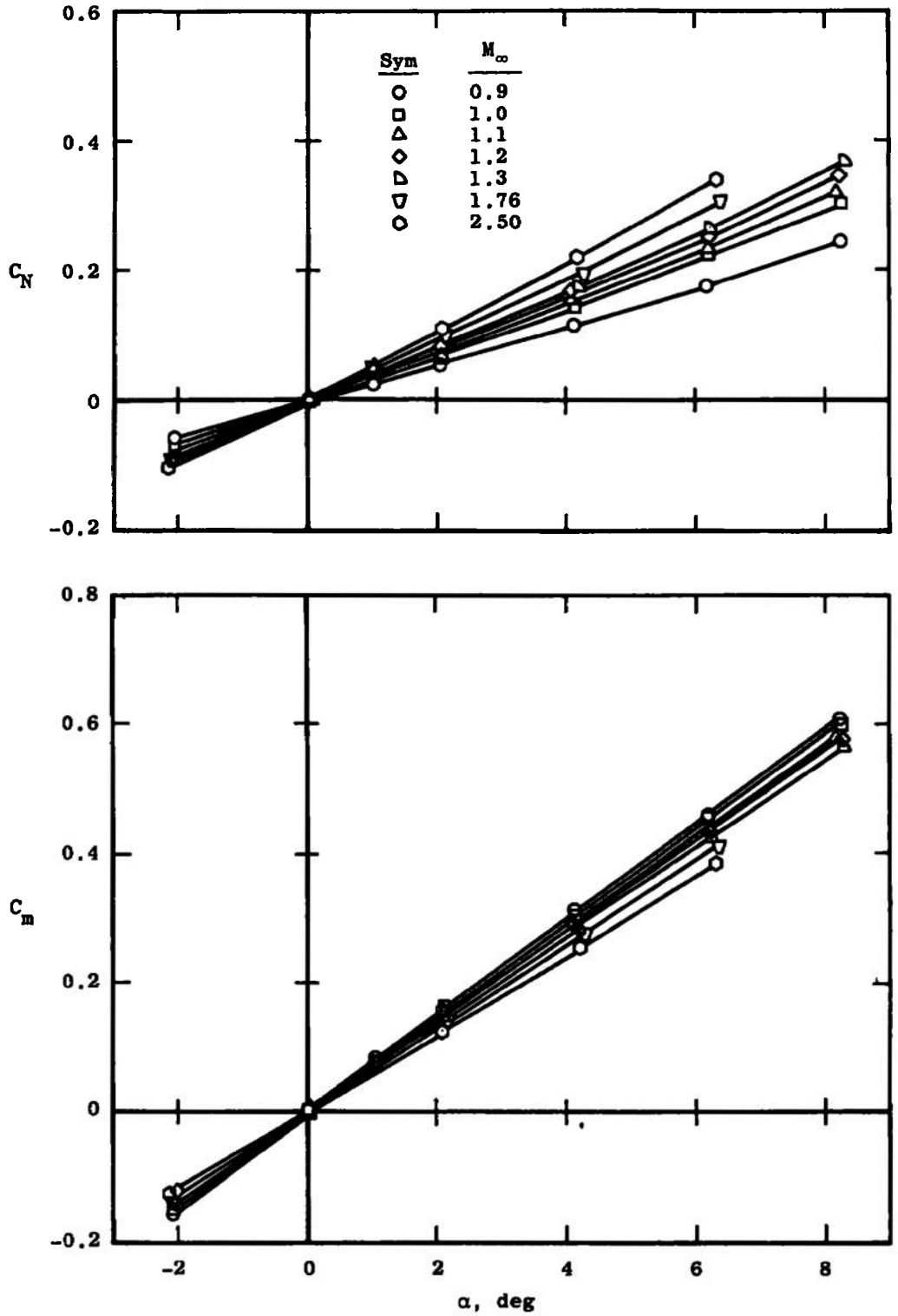

d. With Eight Canted Vanes
Fig. 5 Concluded

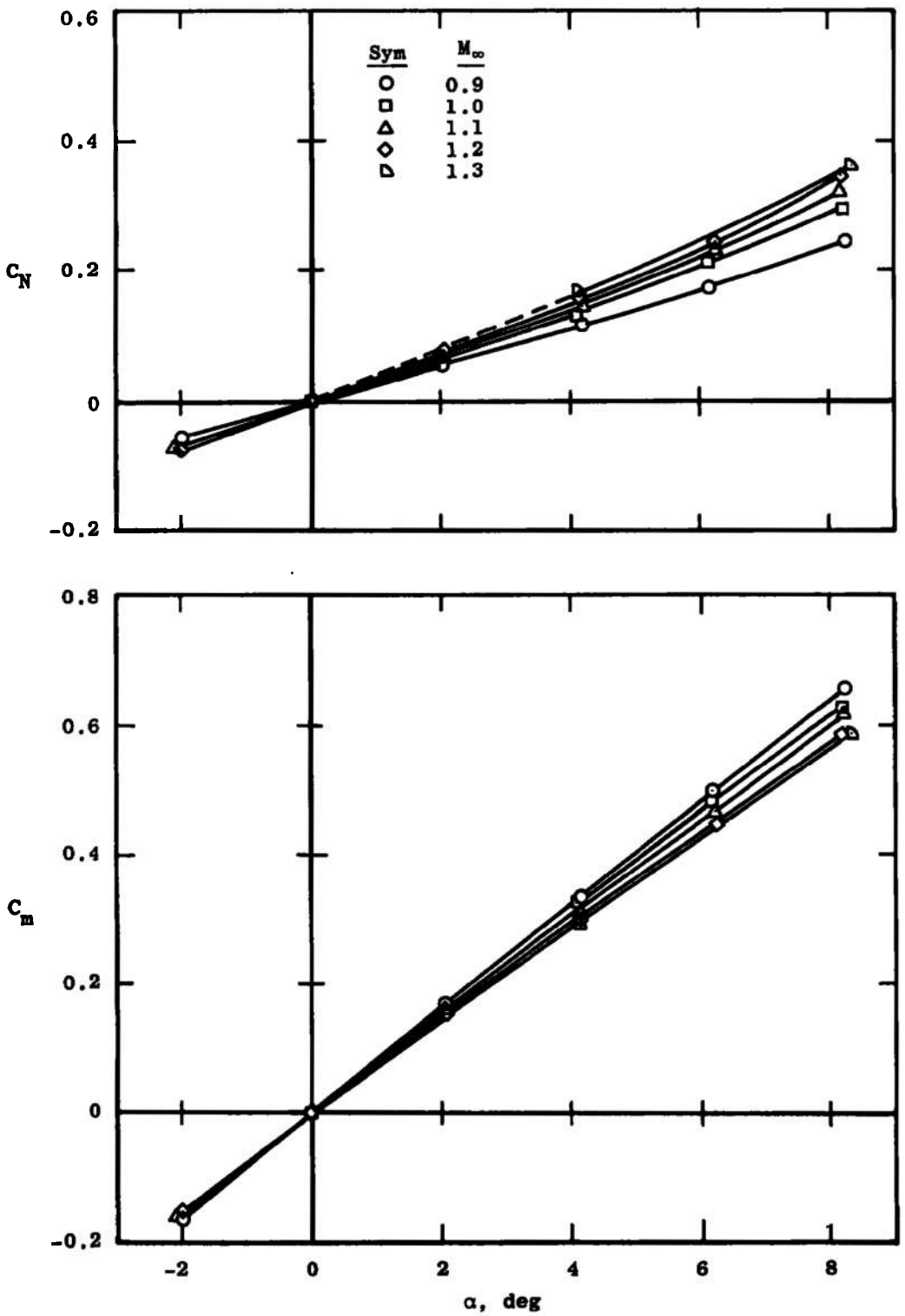

a. With Eight Straight Vanes

Fig. 6 Variation of C_N and C_m with Angle of Attack, Configuration 2

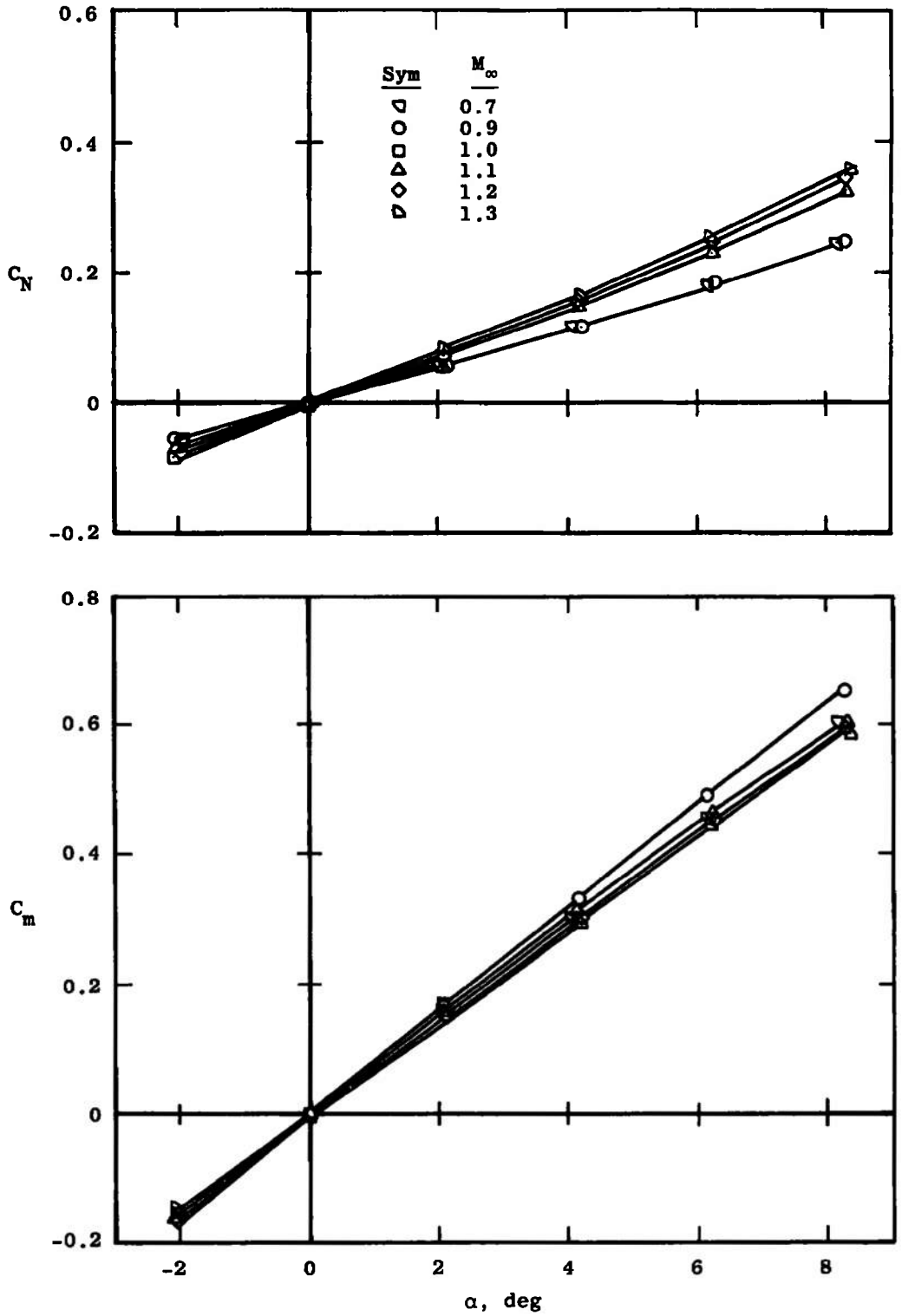

b. With Eight Canted Vanes
Fig. 6 Concluded

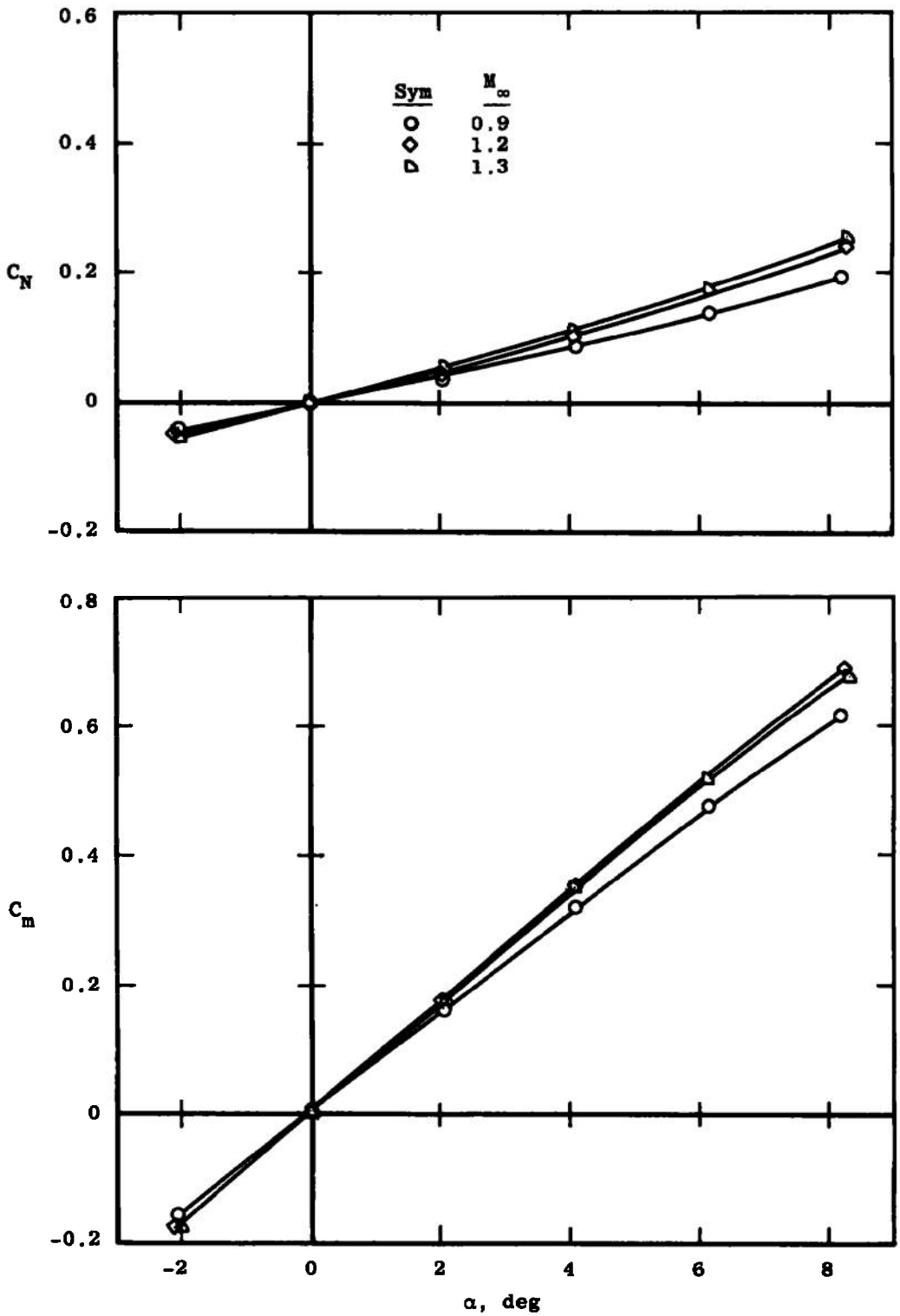

a. Without Vanes

Fig. 7 Variation of C_N and C_m with Angle of Attack, Configuration 3

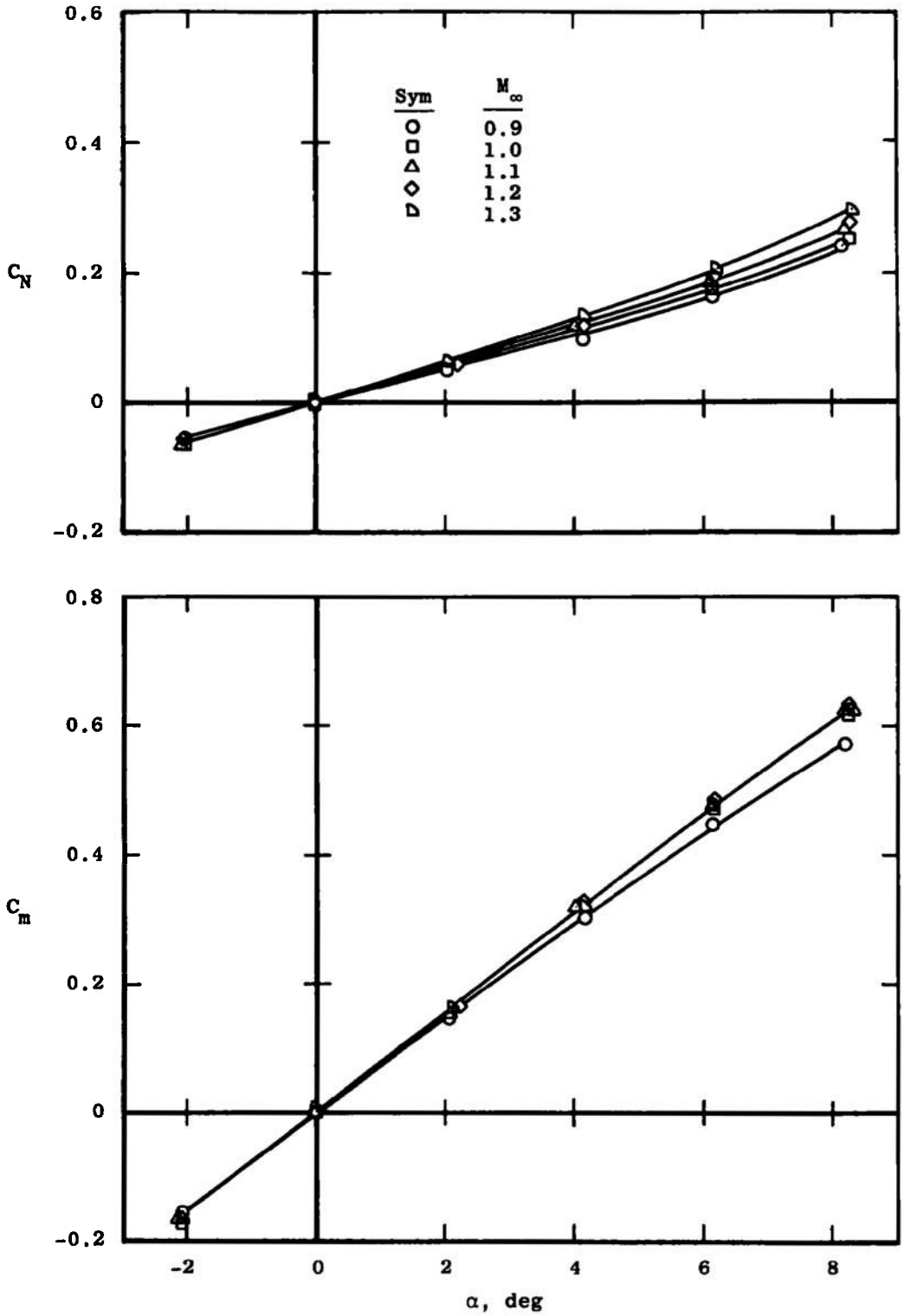

b. With Eight Canted Vanes
Fig. 7 Concluded

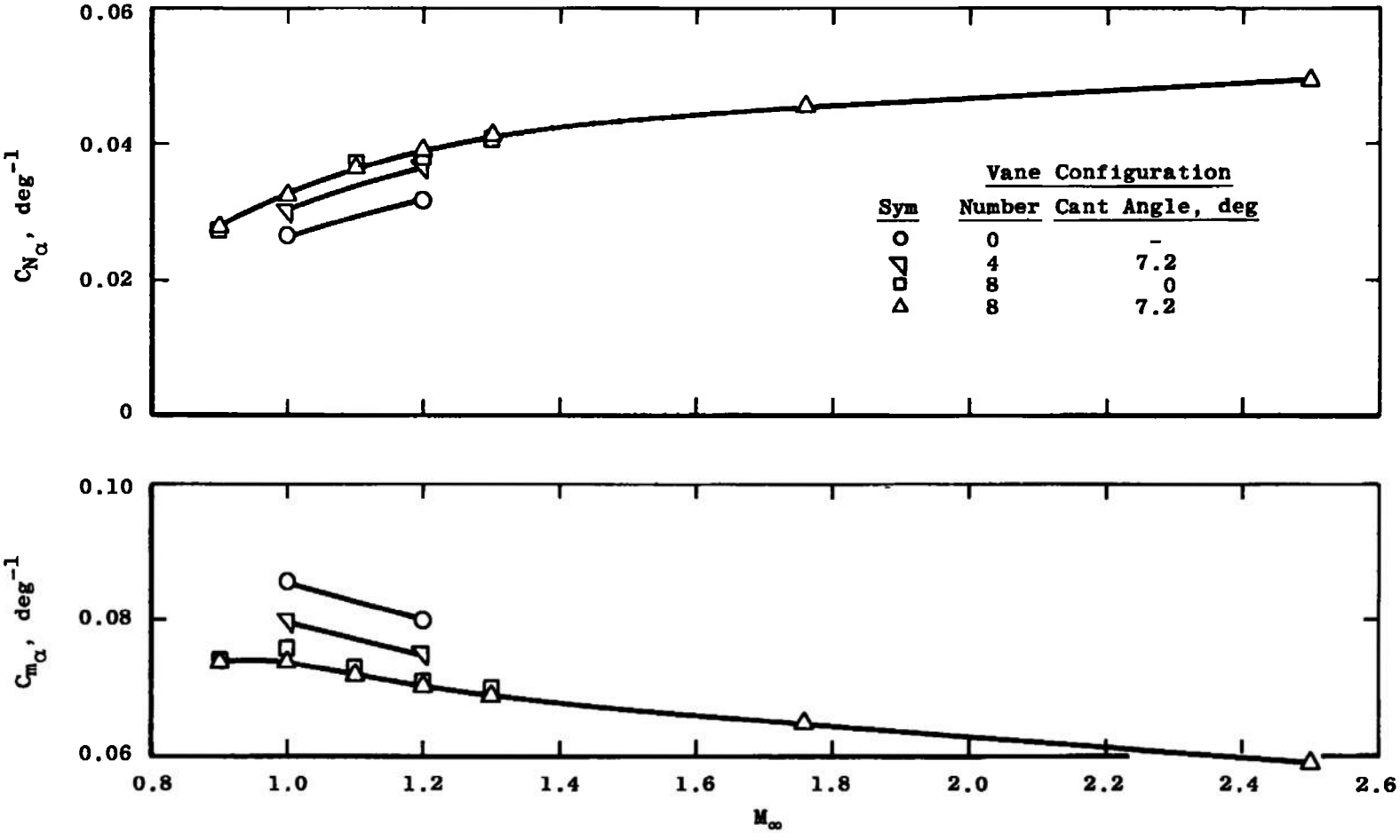

a. Configuration 0

Fig. 8 Variation of C_{N_α} and C_{m_α} with Mach Number

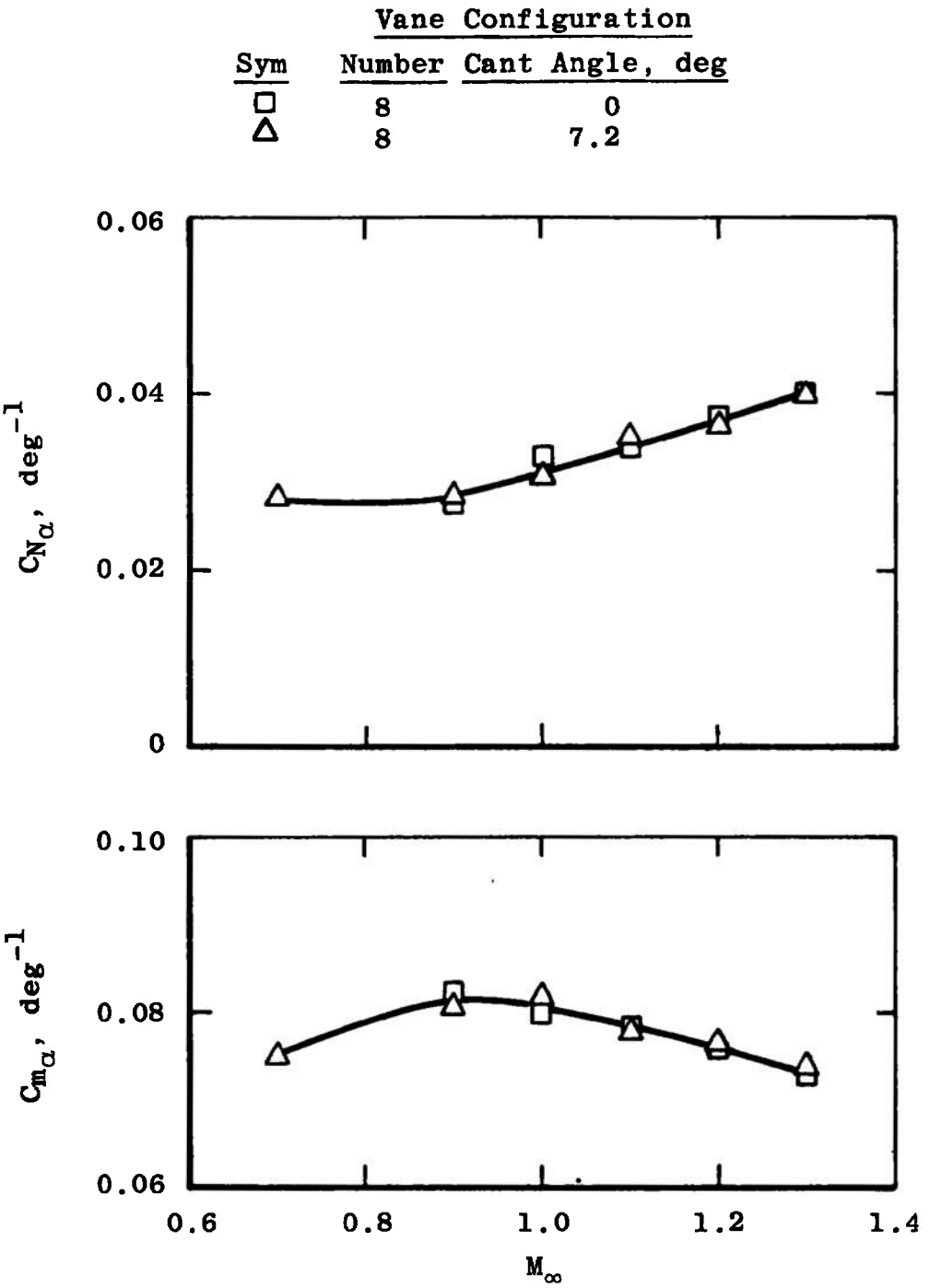

b. Configuration 2
Fig. 8 Continued

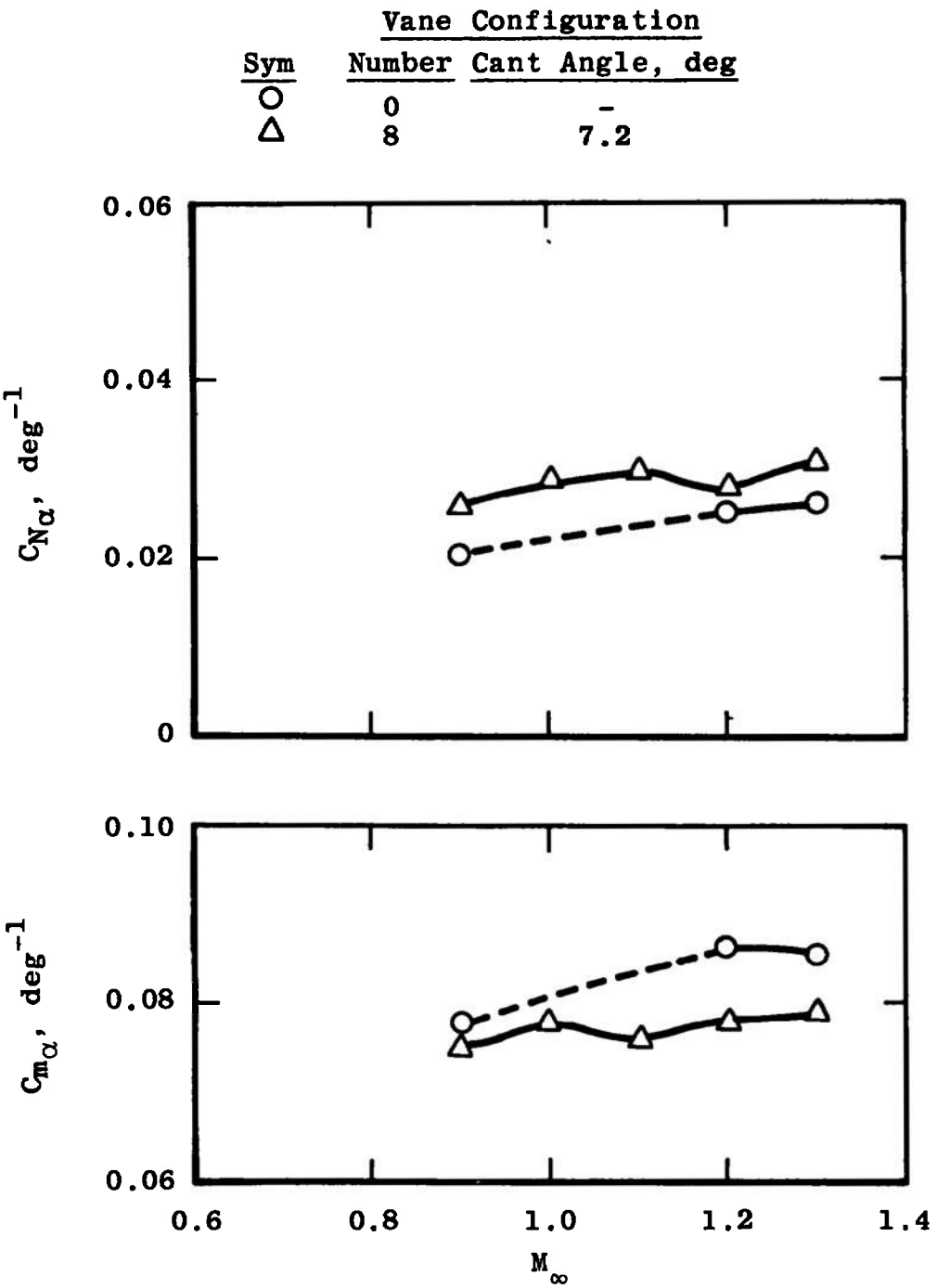

c. Configuration 3
Fig. 8 Concluded

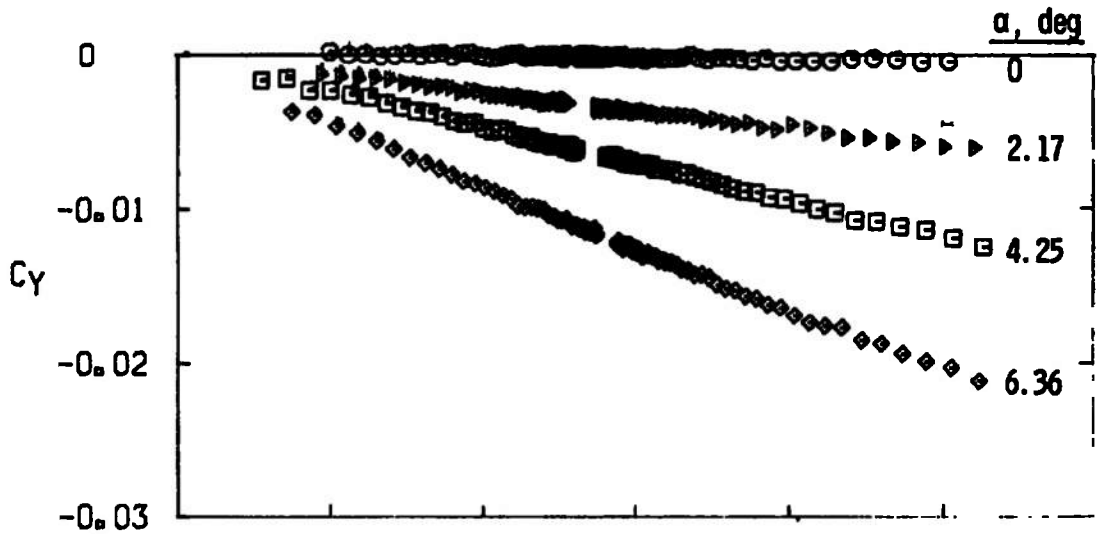

Note: These data are also presented in Fig. 13f.

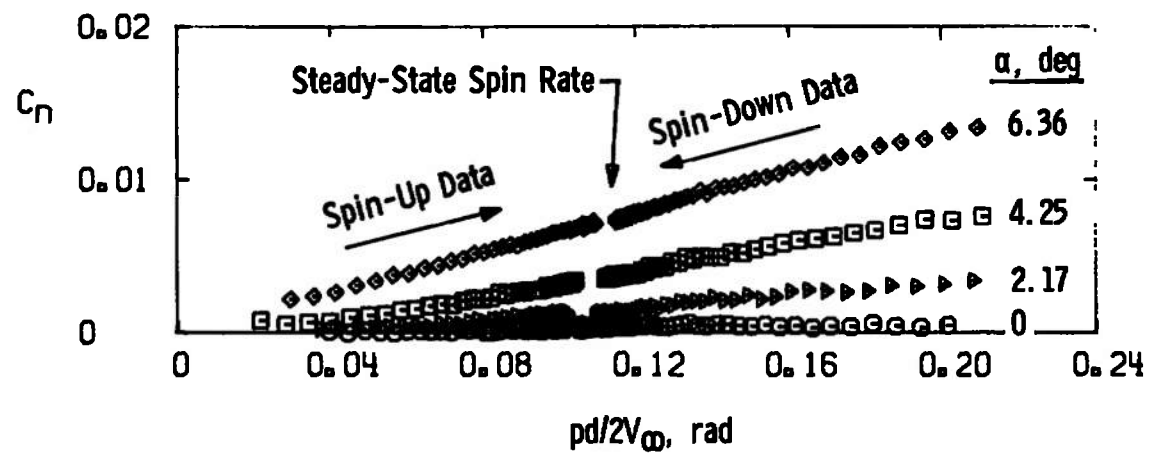

Fig. 9 Typical Variation of C_Y and C_n with $pd/2V_\infty$, M_∞ = 1.76

Sym	α, deg
↑	-2.07
○	0.00
×	1.03
△	2.06
□	4.13
◇	6.19
▷	8.26

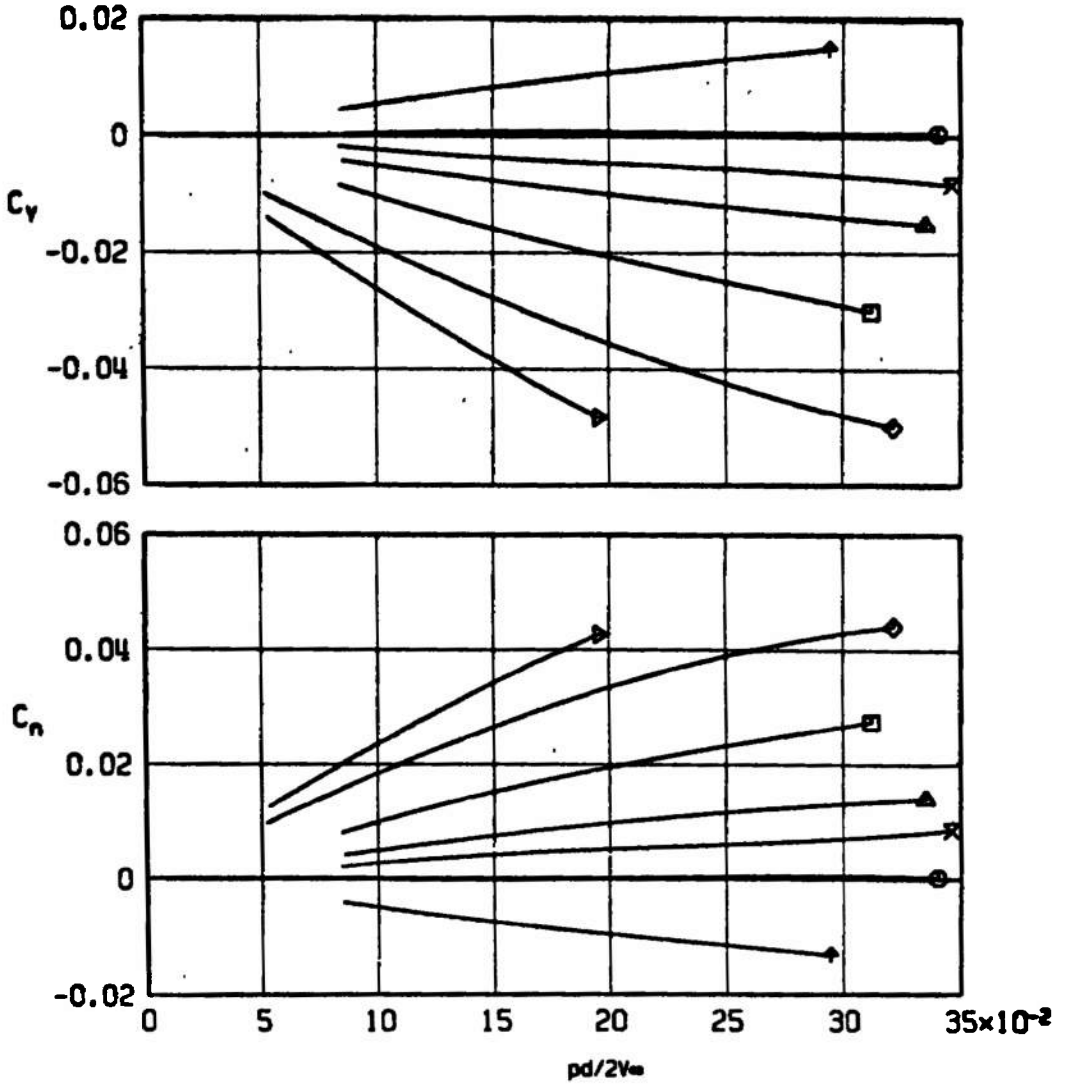

a. $M_\infty = 1.0$

Fig. 10 Variation of C_Y and C_n with $pd/2V_\infty$ for Configuration 0 without Vanes

Sym	α, deg
↑	-2.07
○	0.00
△	2.07
□	4.14
◇	6.21
▷	8.28

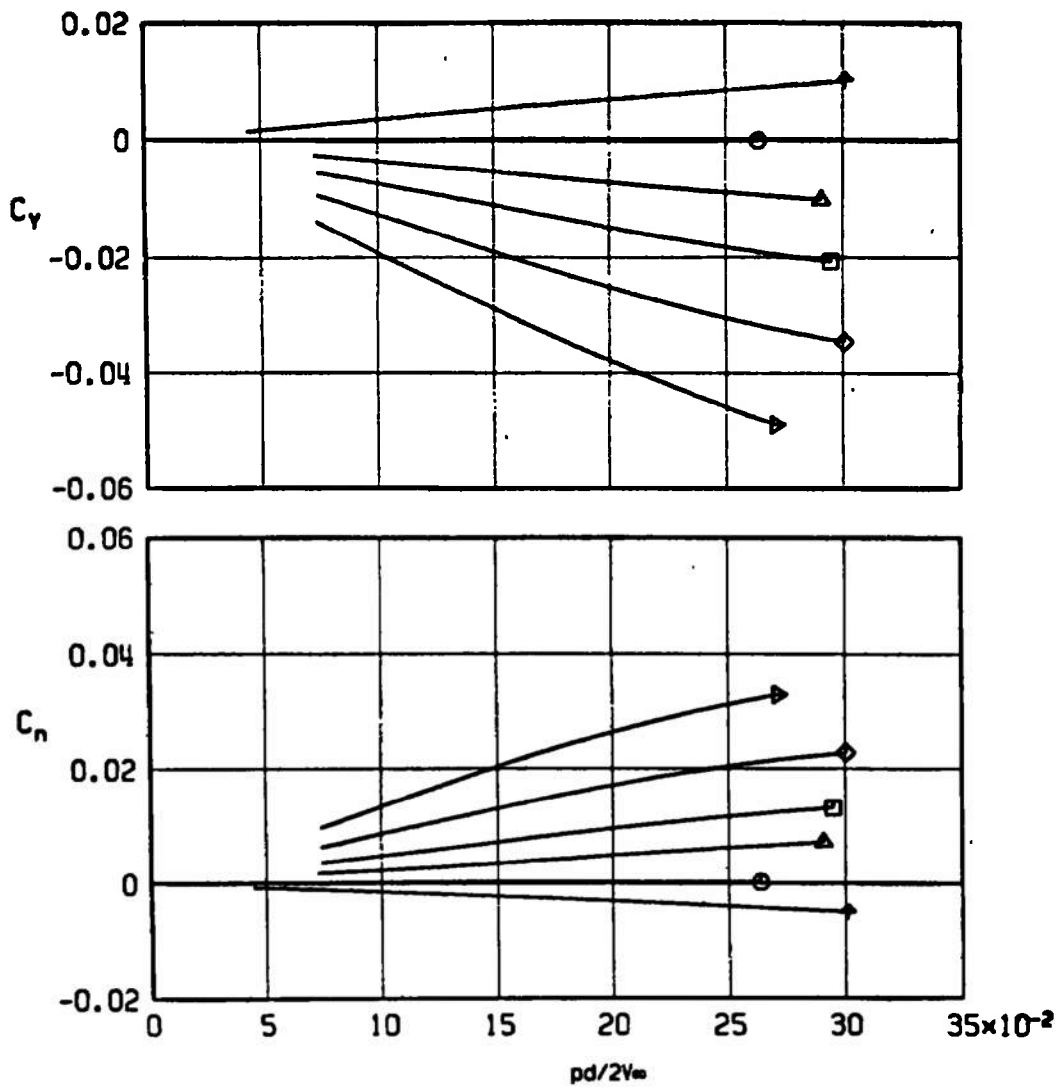

b. $M_\infty = 1.2$

Fig. 10 Concluded

Sym	α, deg
✦	-2.06
⊙	0.00
△	2.04
⊡	4.10
◇	6.15
▷	8.22

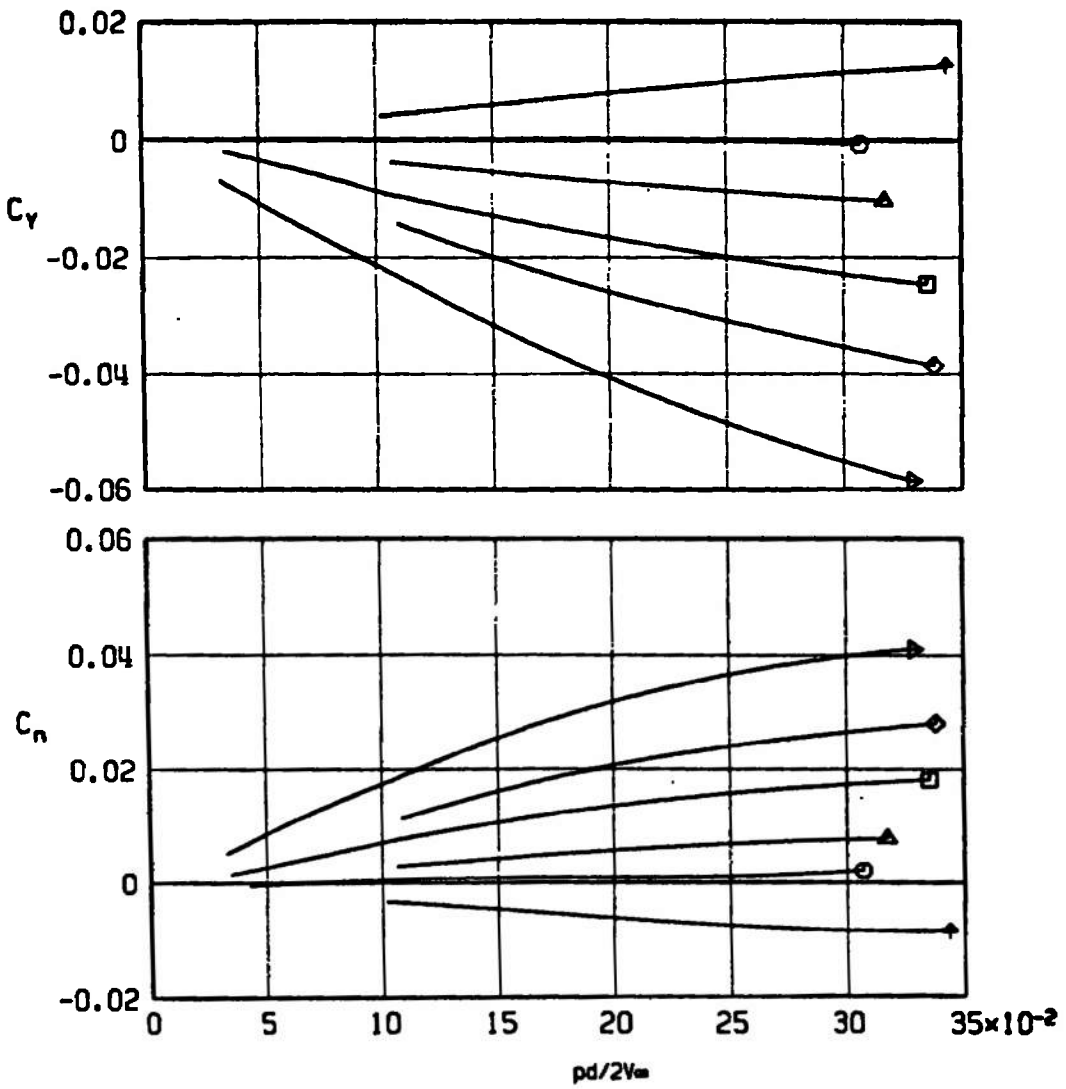

a. $M_\infty = 1.0$

Fig. 11 Variation of C_Y and C_n with $pd/2V_\infty$ for Configuration 0 with Four Canted Vanes

Sym	α, deg
↑	-2.05
○	0.00
△	2.03
□	4.10
◇	6.19
▷	8.25

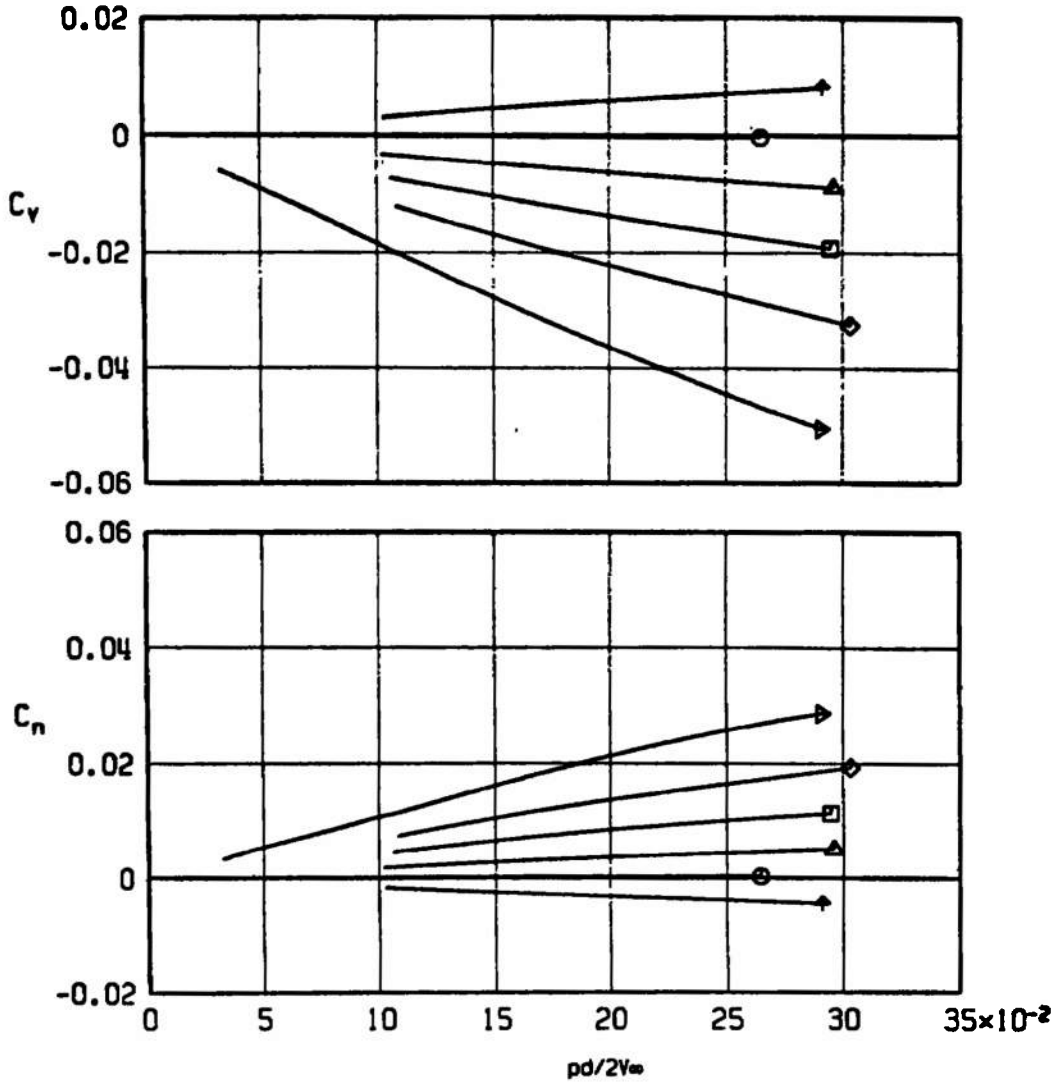

b. $M_\infty = 1.2$

Fig. 11 Concluded

Sym	α, deg
✦	-2.05
⊙	0.00
✕	1.03
△	2.06
⊡	4.11
◇	6.18
▷	8.22

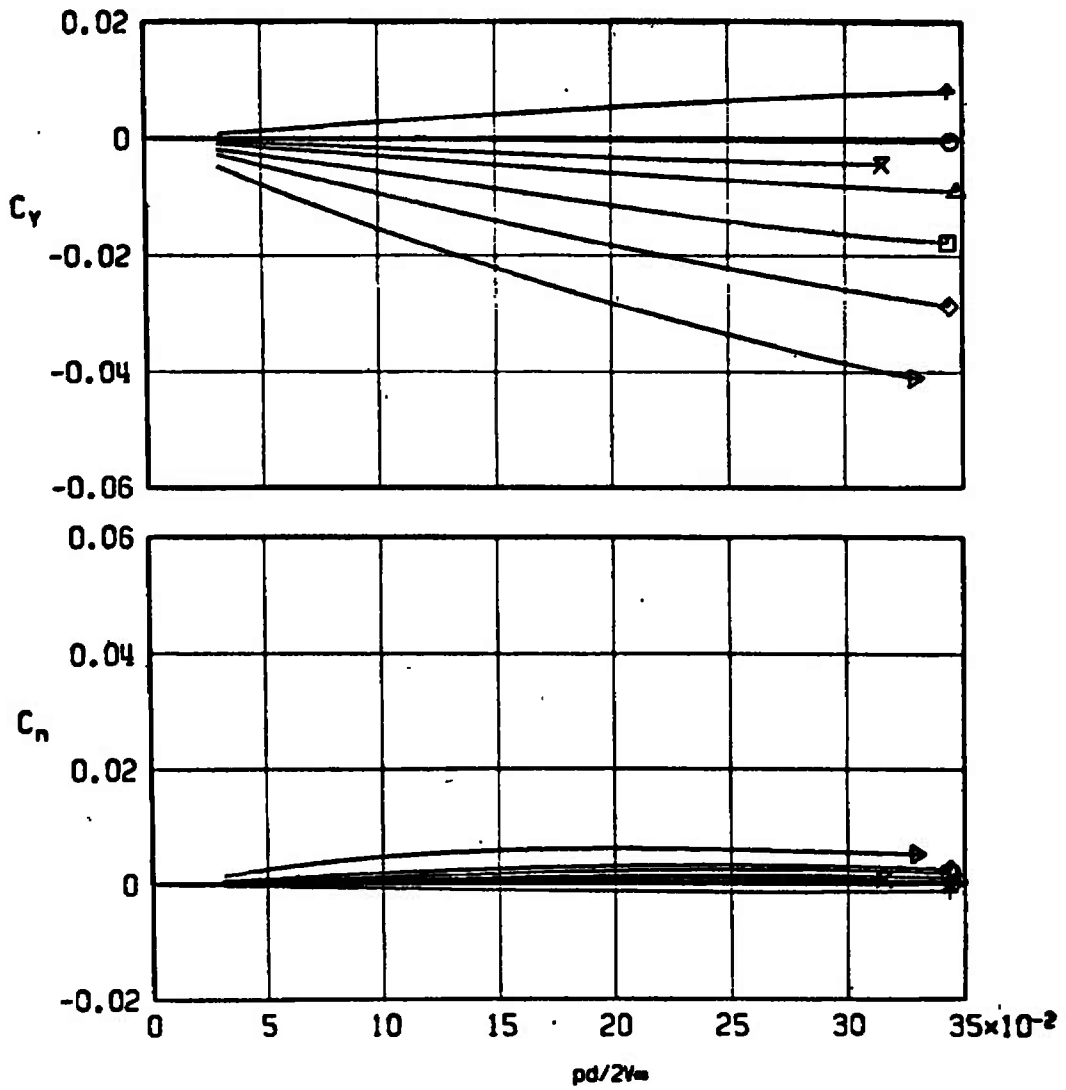

a. $M_\infty = 0.9$

Fig. 12 Variation of C_Y and C_n with $pd/2V_\infty$ for Configuration 0 with Eight Straight Vanes

Sym	α, deg
↑	-2.06
○	0.00
×	1.03
△	2.06
□	4.12
◇	6.18
▷	8.24

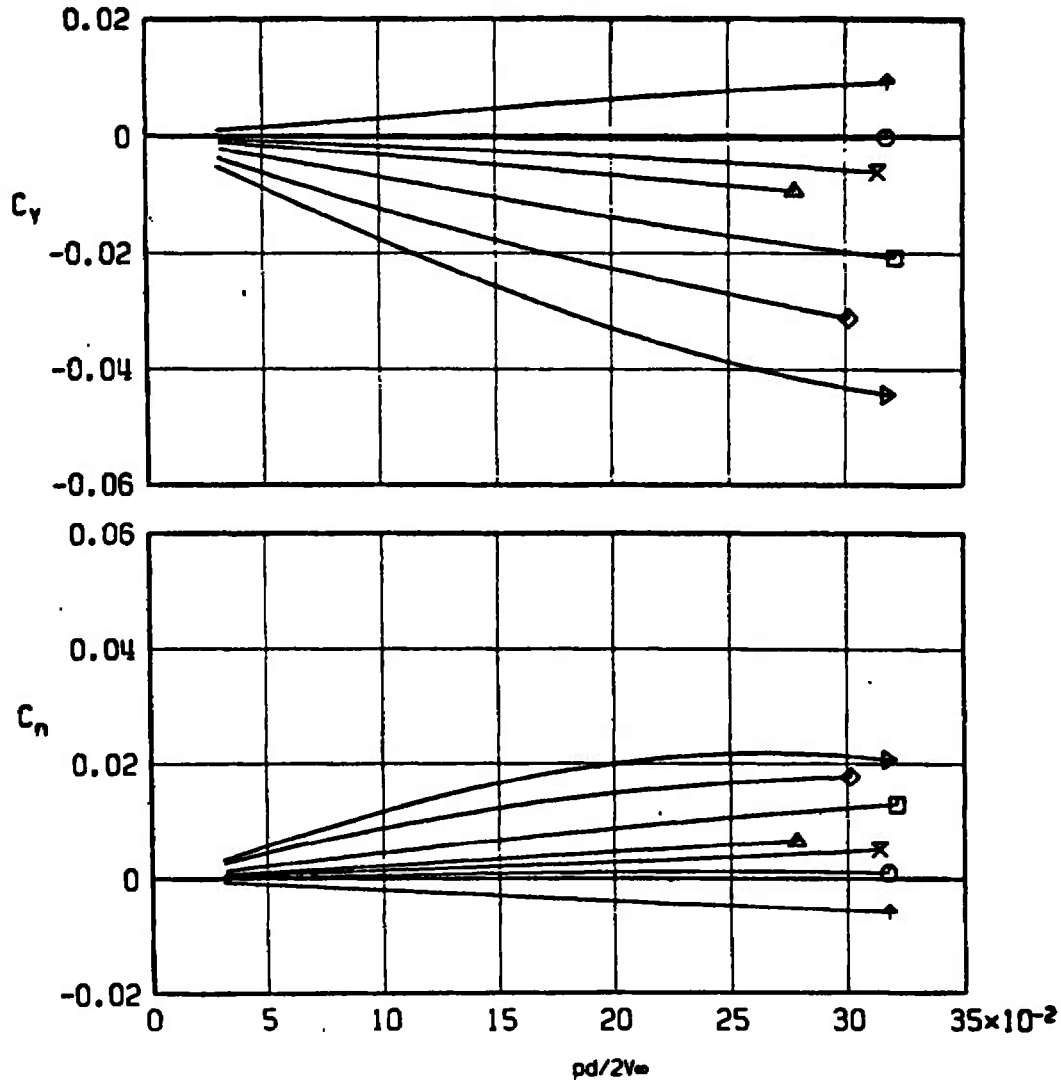

b. M_∞ = 1.0

Fig. 12 Continued

Sym	α, deg
↑	-2.07
○	0.00
×	1.03
△	2.06
□	4.12
◇	6.18
▷	8.25

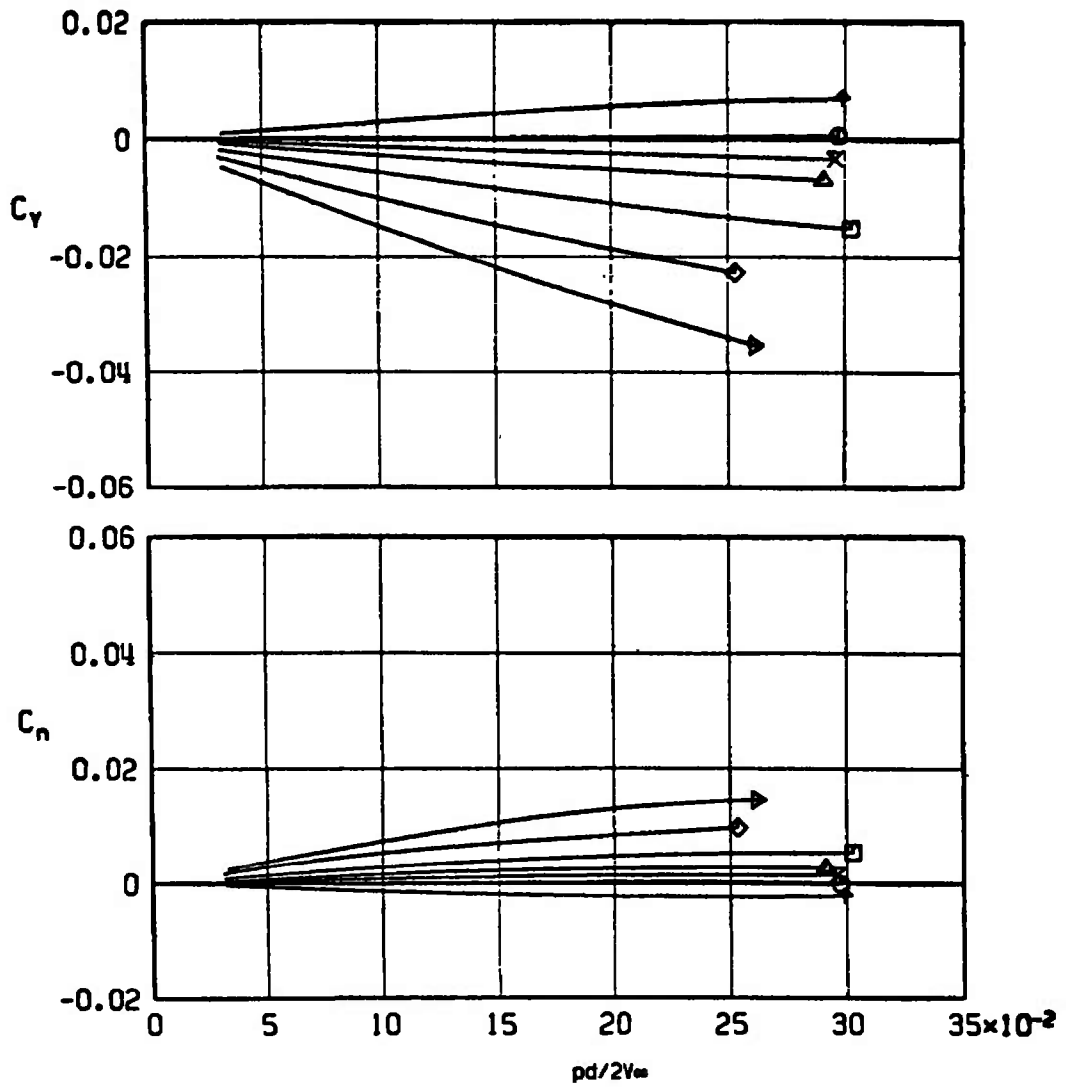

c. $M_\infty = 1.1$

Fig. 12 Continued

Sym	α, deg
↑	-2.06
○	0.00
✕	1.04
△	2.07
□	4.14
◇	6.21
▷	8.28

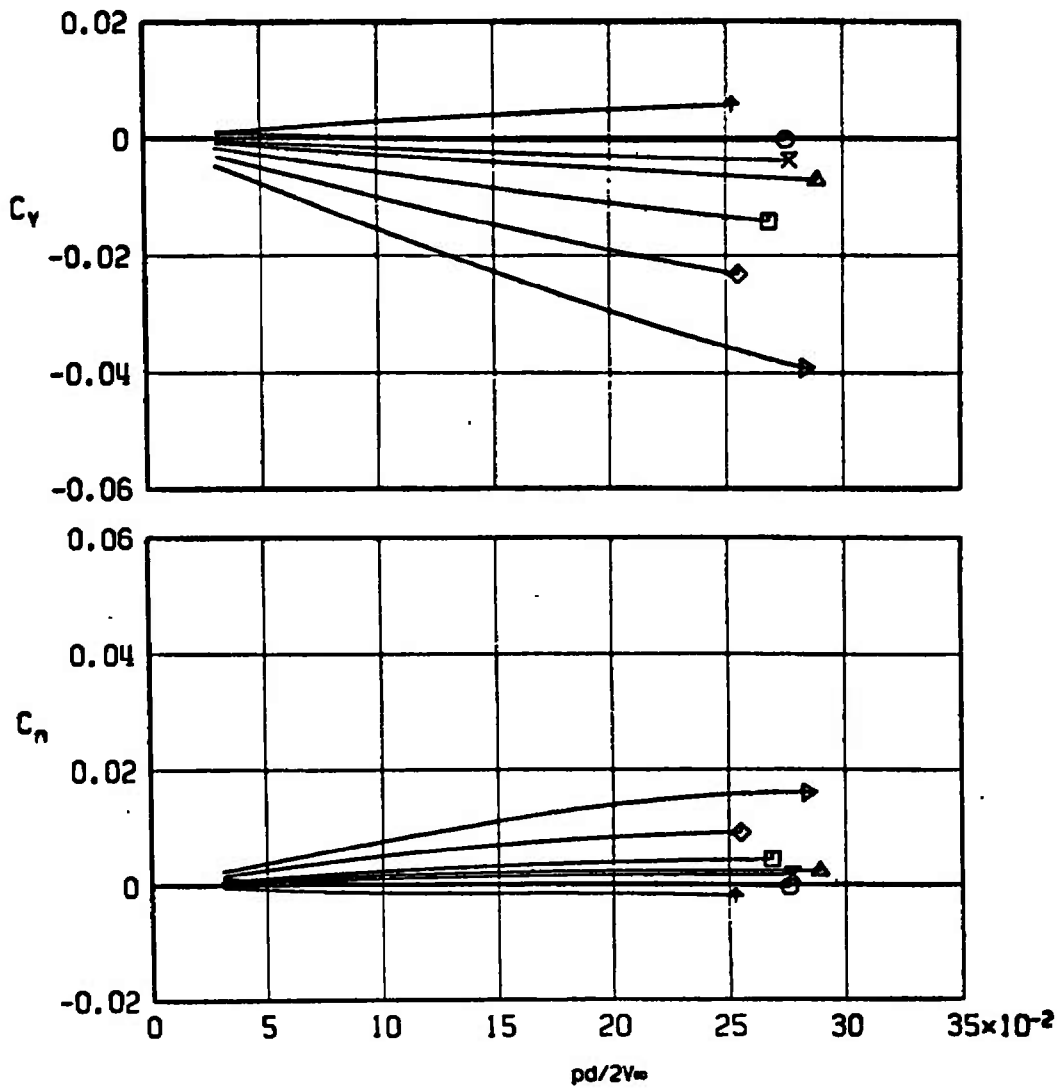

d. $M_\infty = 1.2$

Fig. 12 Continued

Sym	α, deg
↑	-2.06
○	0.00
×	1.04
△	2.07
□	4.14
◇	6.21
▷	8.28

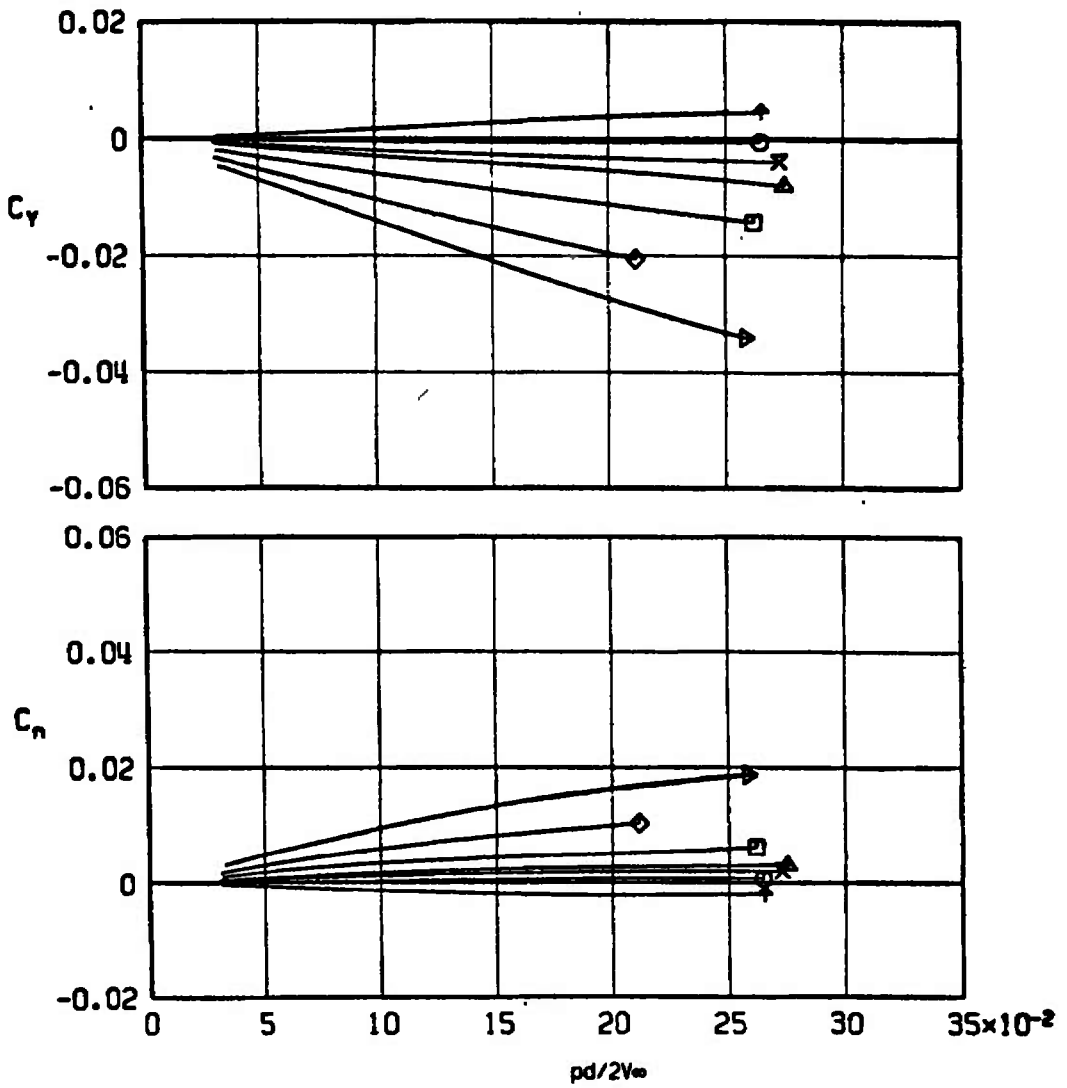

e. $M_\infty = 1.3$

Fig. 12 Concluded

Sym	α, deg
◆	-2.02
○	0.00
✕	1.03
△	2.04
□	4.07
◇	6.14
▷	8.22

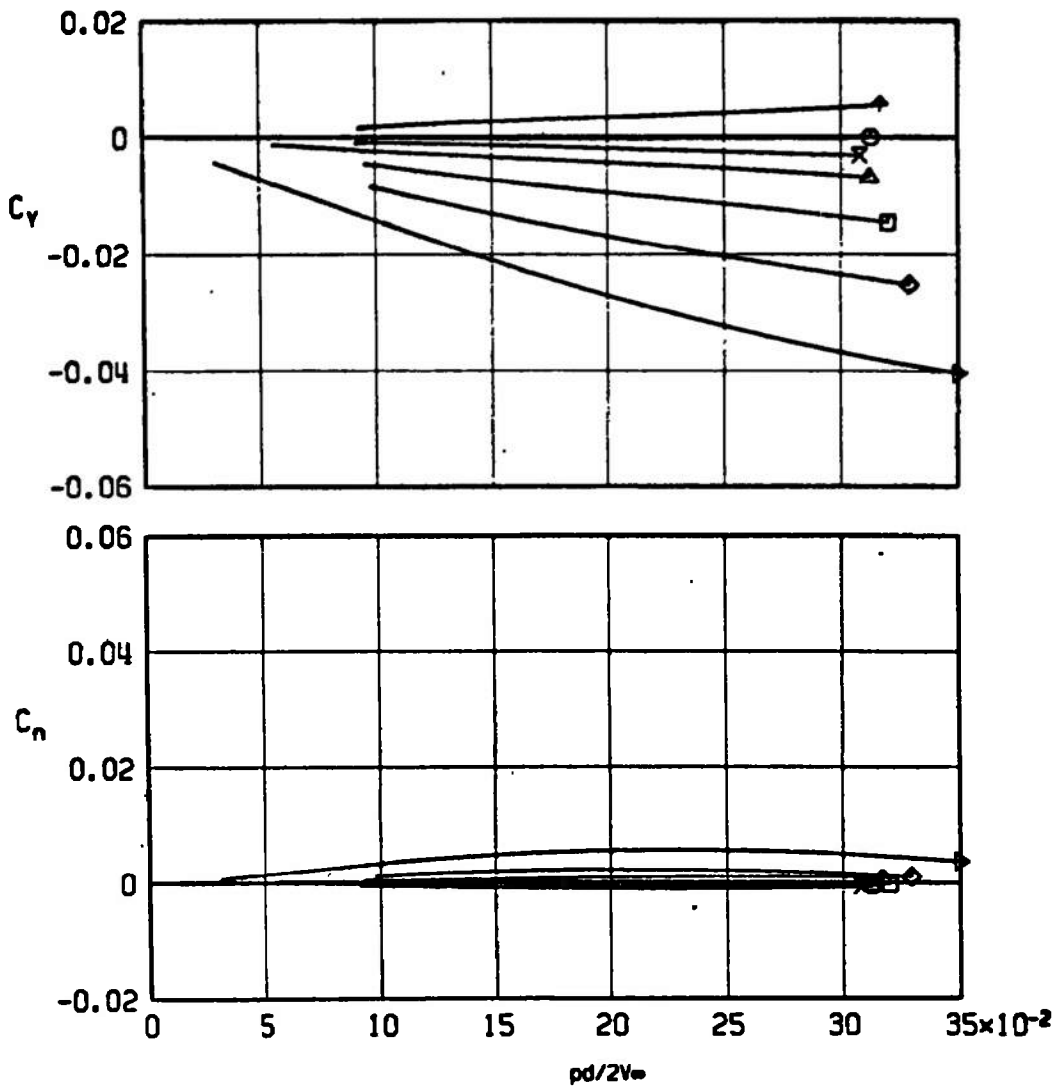

a. $M_\infty = 0.9$

Fig. 13 Variation of C_Y and C_n with $pd/2V_\infty$ for Configuration 0 with Eight Canted Vanes

Sym	α, deg
◆	-2.06
○	0.00
✕	1.03
△	2.05
□	4.08
◇	6.18
▷	8.24

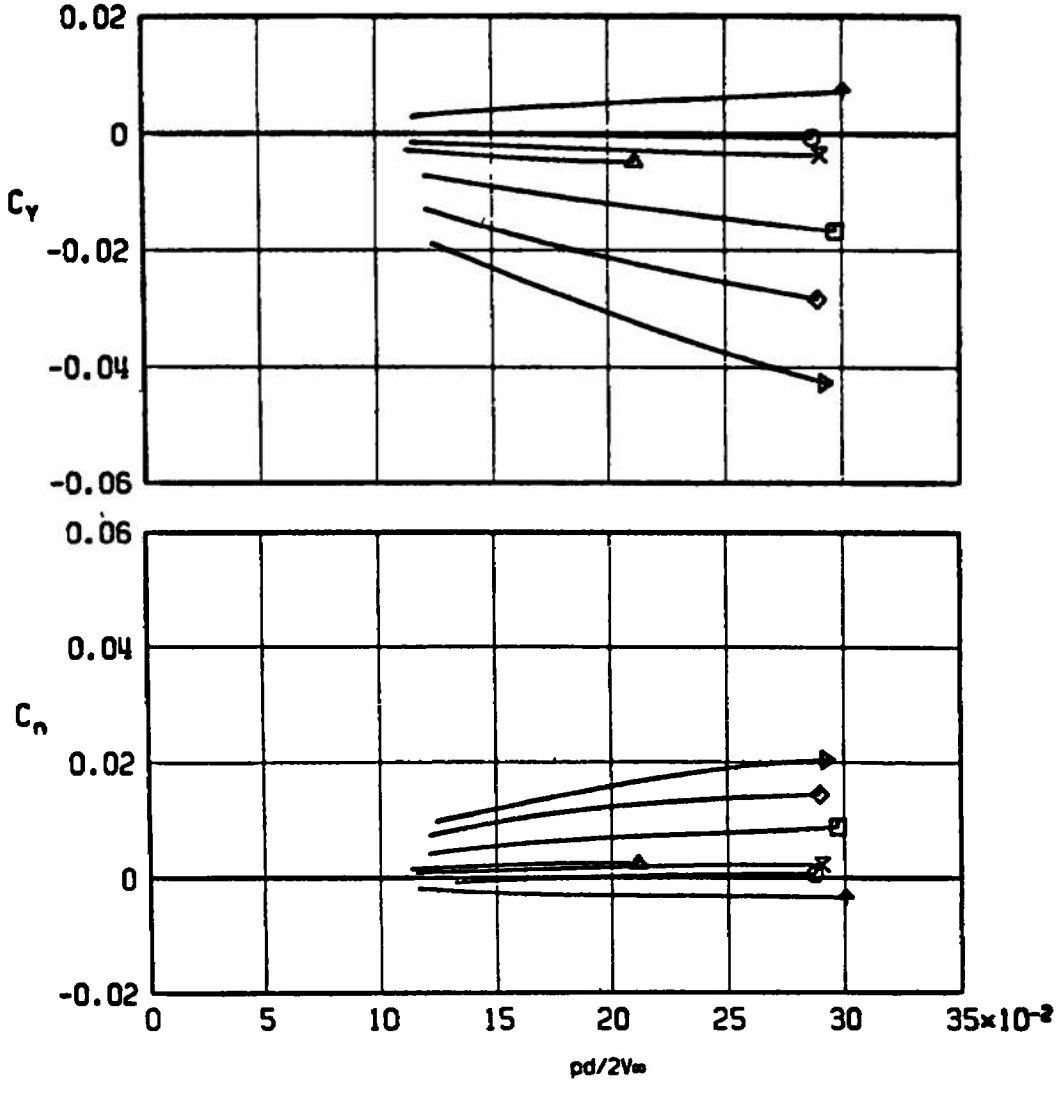

b. $M_\infty = 1.0$
Fig. 13 Continued

Sym	α, deg
✦	-2.06
⊙	0.00
✕	1.03
△	2.06
⊡	4.08
◇	6.19
▷	8.24

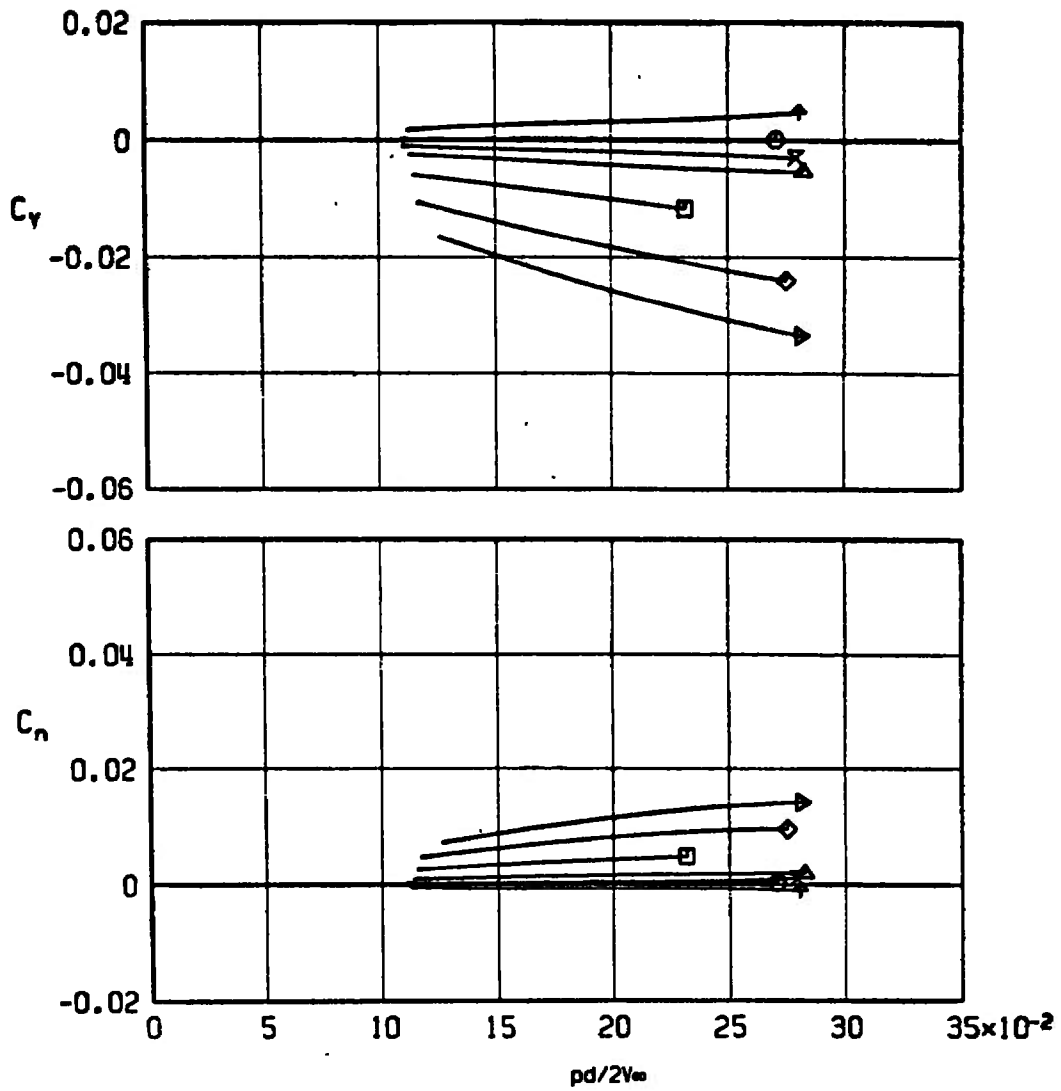

c. $M_\infty = 1.1$

Fig. 13 Continued

Sym	α, deg
↑	-2.05
⊙	0.00
✕	1.04
△	2.08
□	4.09
◇	6.21
▷	8.23

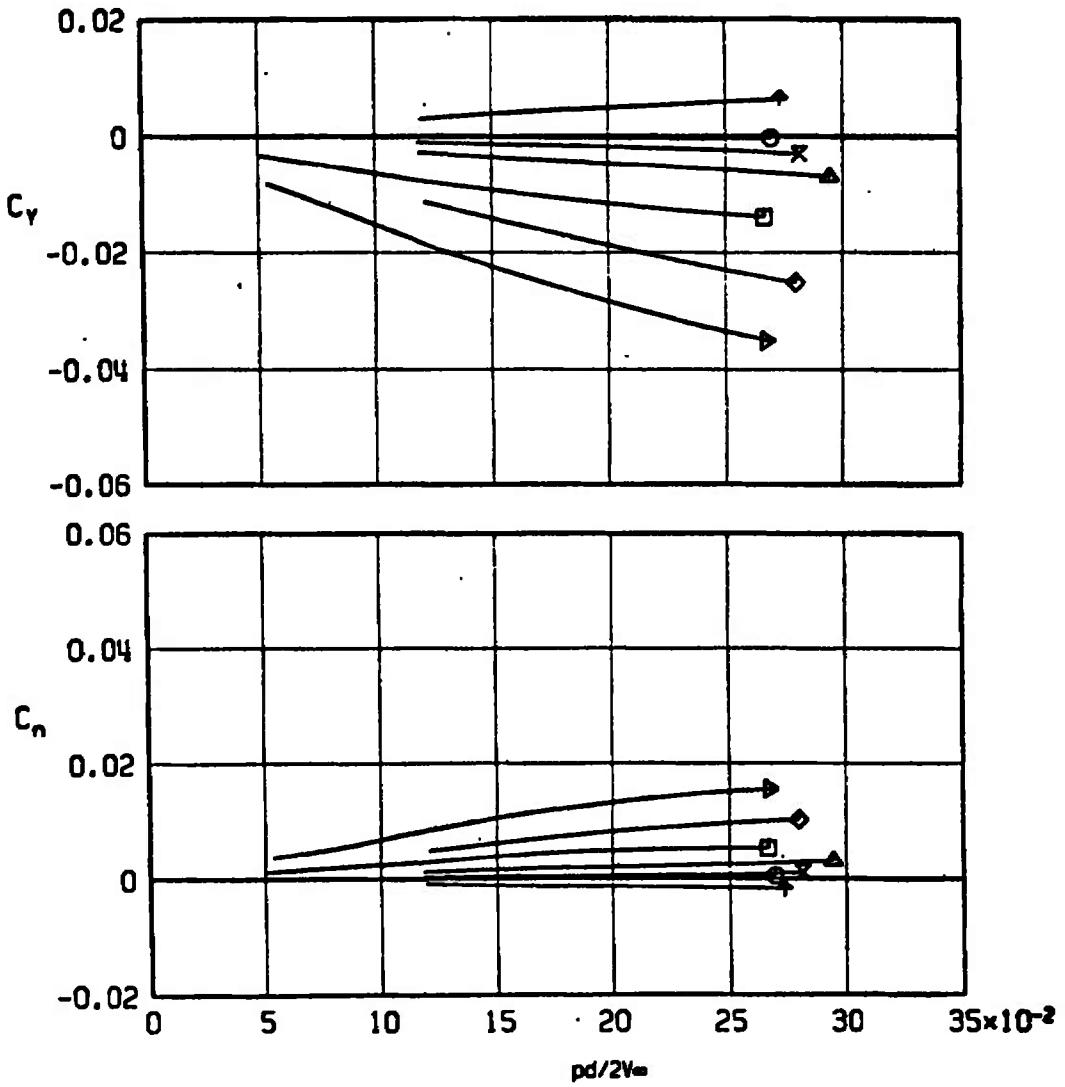

d. $M_\infty = 1.2$

Fig. 13 Continued

Sym	α, deg
↑	-2.06
○	0.00
×	1.03
△	2.08
□	4.08
◇	6.21
▷	8.22

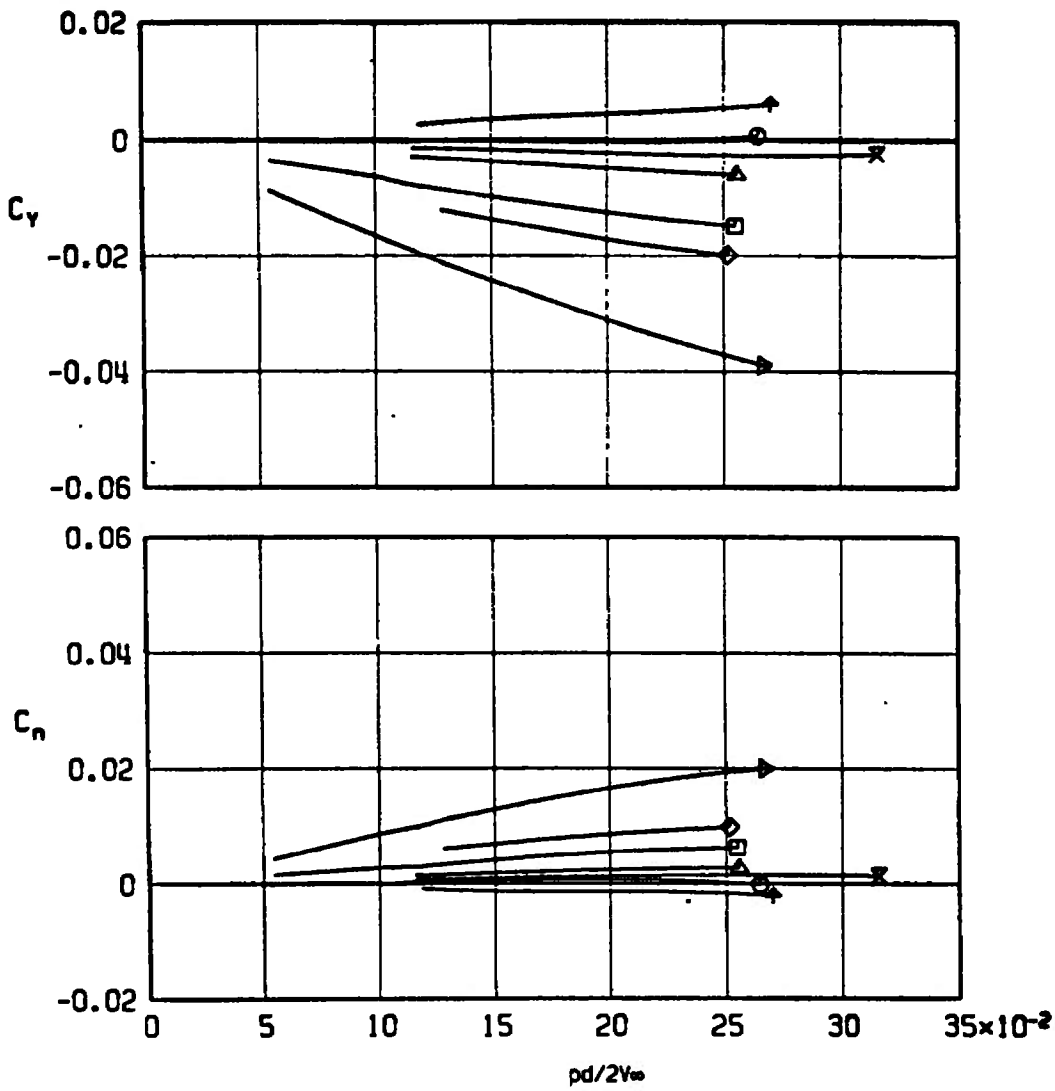

e. $M_\infty = 1.3$

Fig. 13 Continued

Sym	α, deg
◆	-2.12
○	0.00
△	2.17
□	4.25
◇	6.36

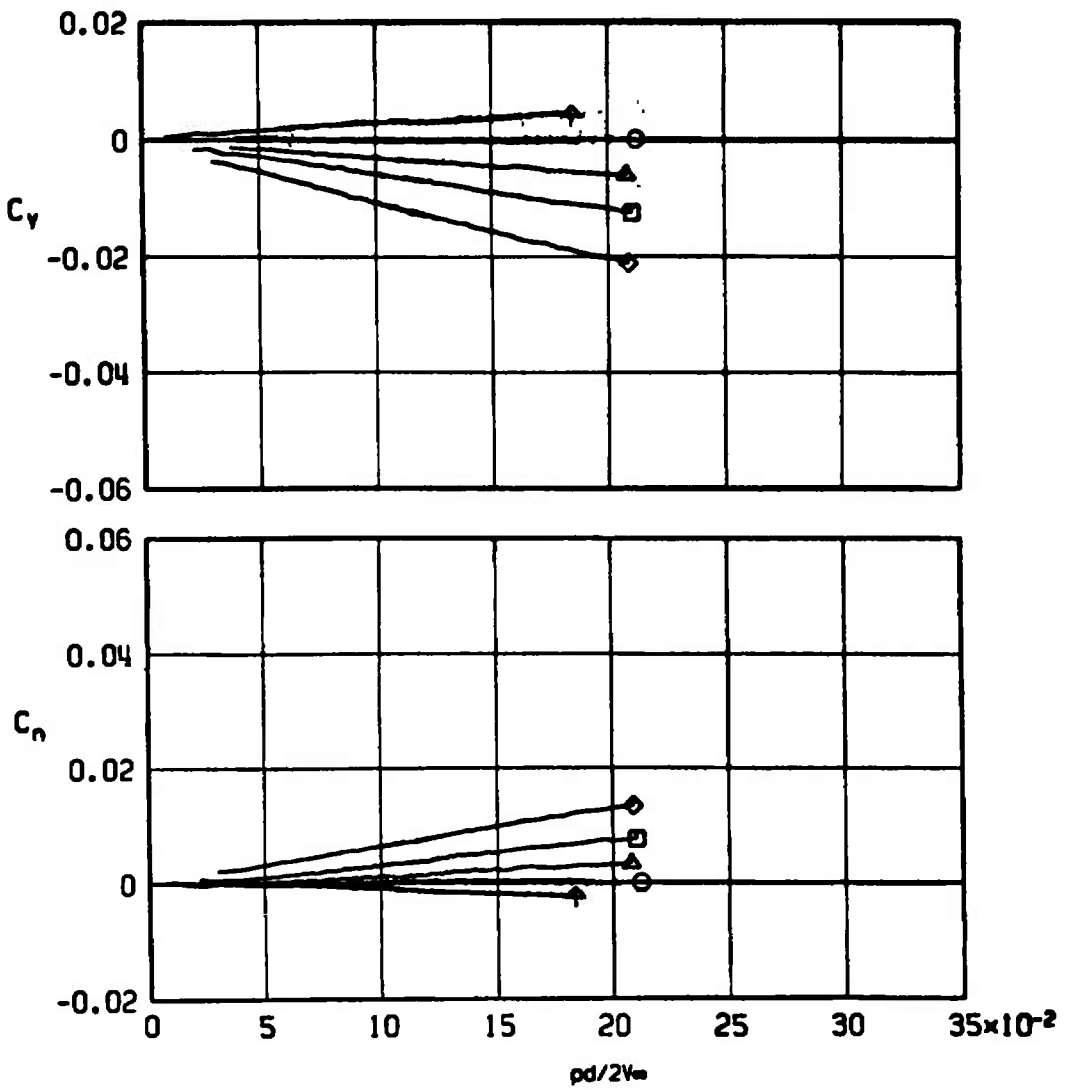

f. $M_\infty = 1.76$
Fig. 13 Continued

Sym	α, deg
♦	-2.15
○	0.00
△	2.07
□	4.19
◇	6.30

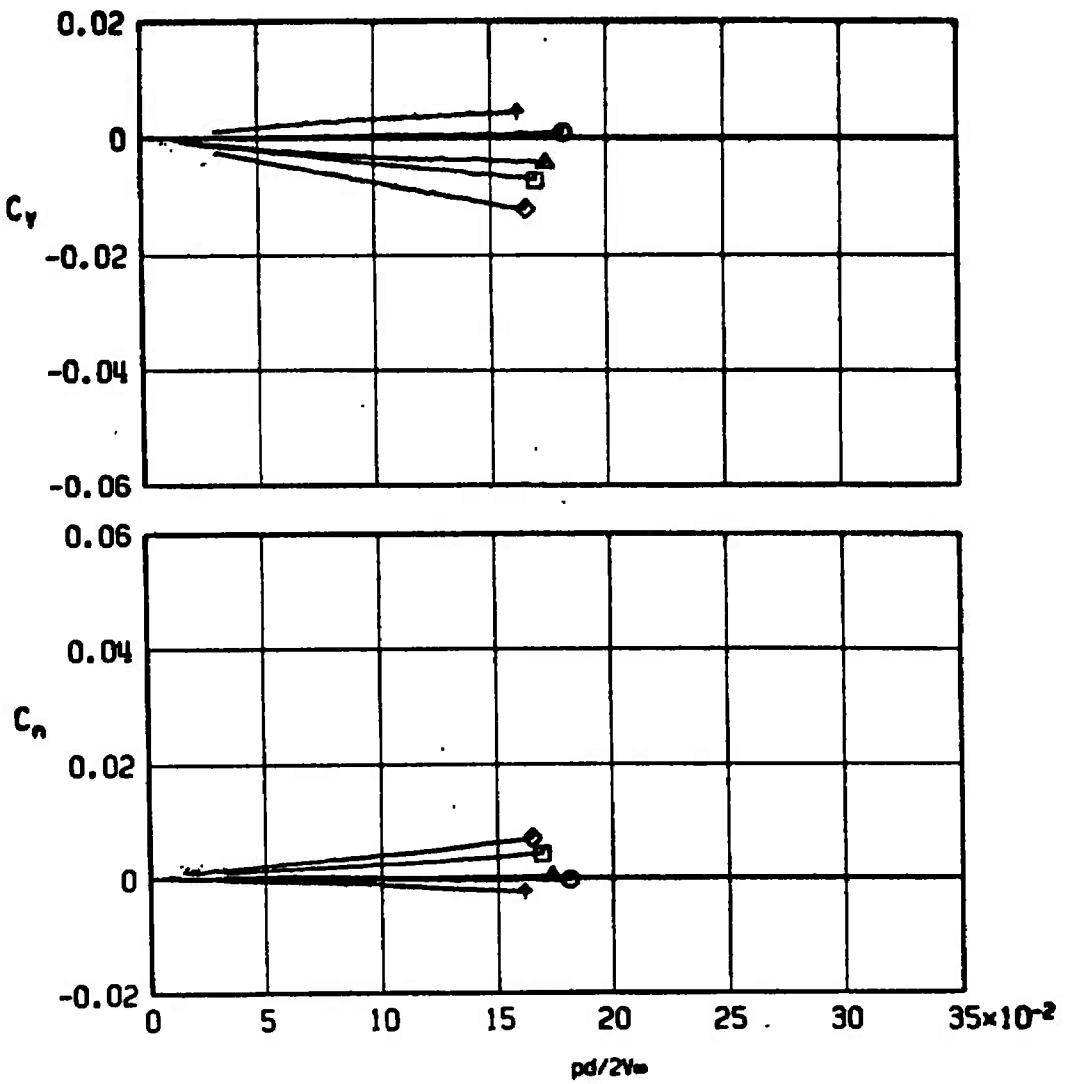

g. $M_\infty = 2.50$

Fig. 13 Concluded

Sym	α, deg
↑	-2.06
○	0.00
△	2.06
□	4.14
◇	6.20
▷	8.26

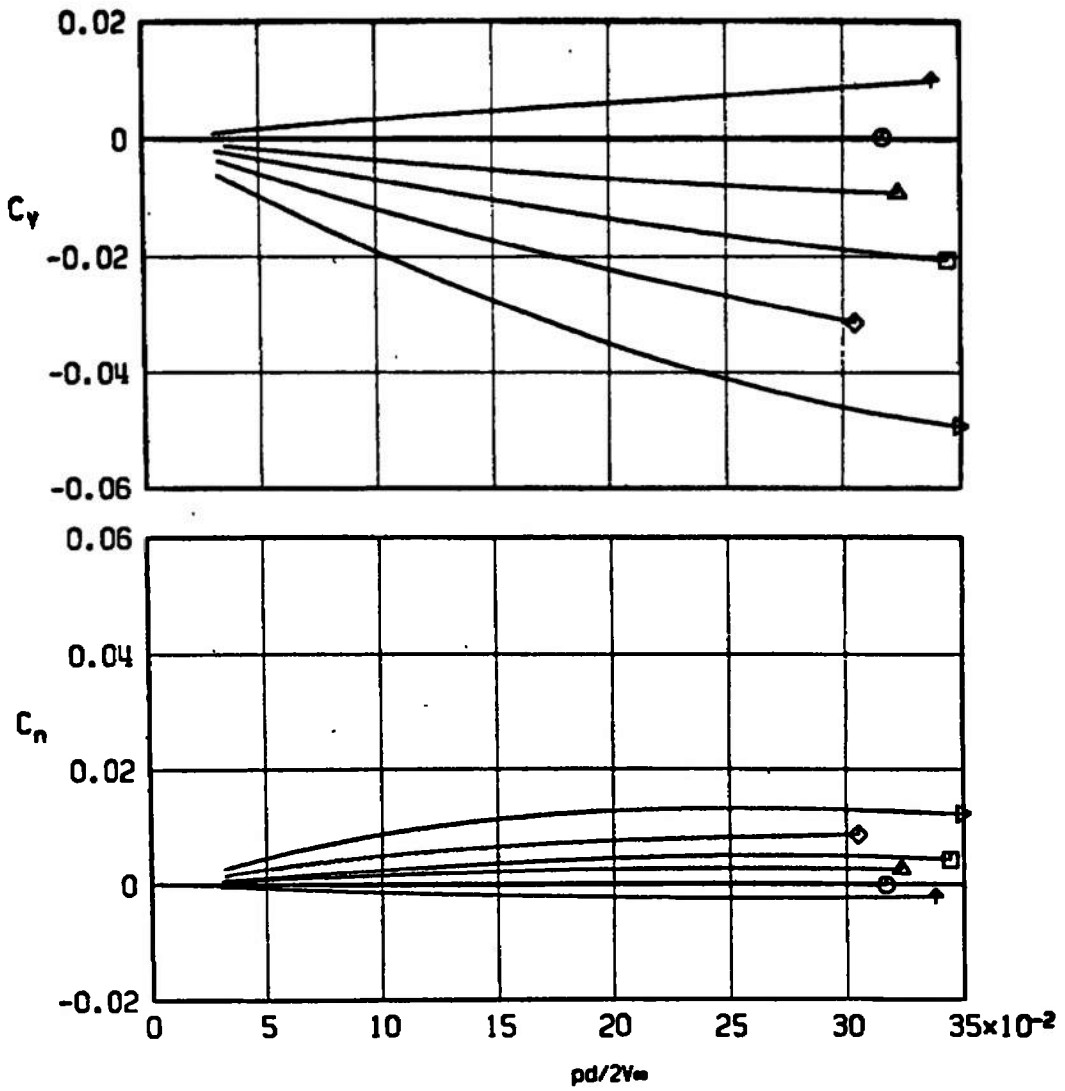

a. $M_\infty = 0.9$

Fig. 14 Variation of C_Y and C_n with $pd/2V_\infty$ for Configuration 2 with Eight Straight Vanes

Sym	α, deg
□	4.14
◇	6.21
▷	8.29

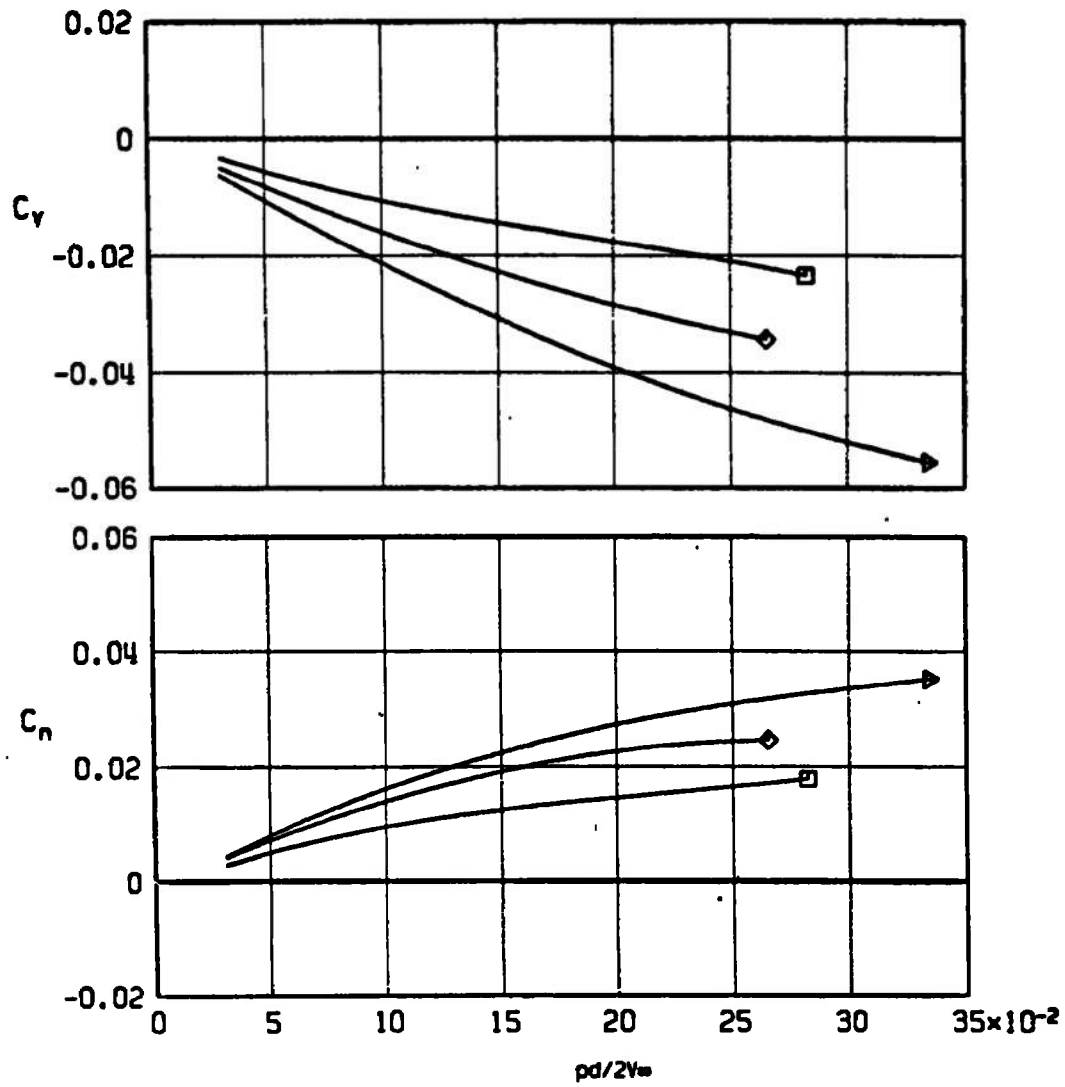

b. $M_\infty = 1.0$
Fig. 14 Continued

Sym	α, deg
↑	-2.09
○	0.00
△	2.08
□	4.15
◇	6.21
▷	8.29

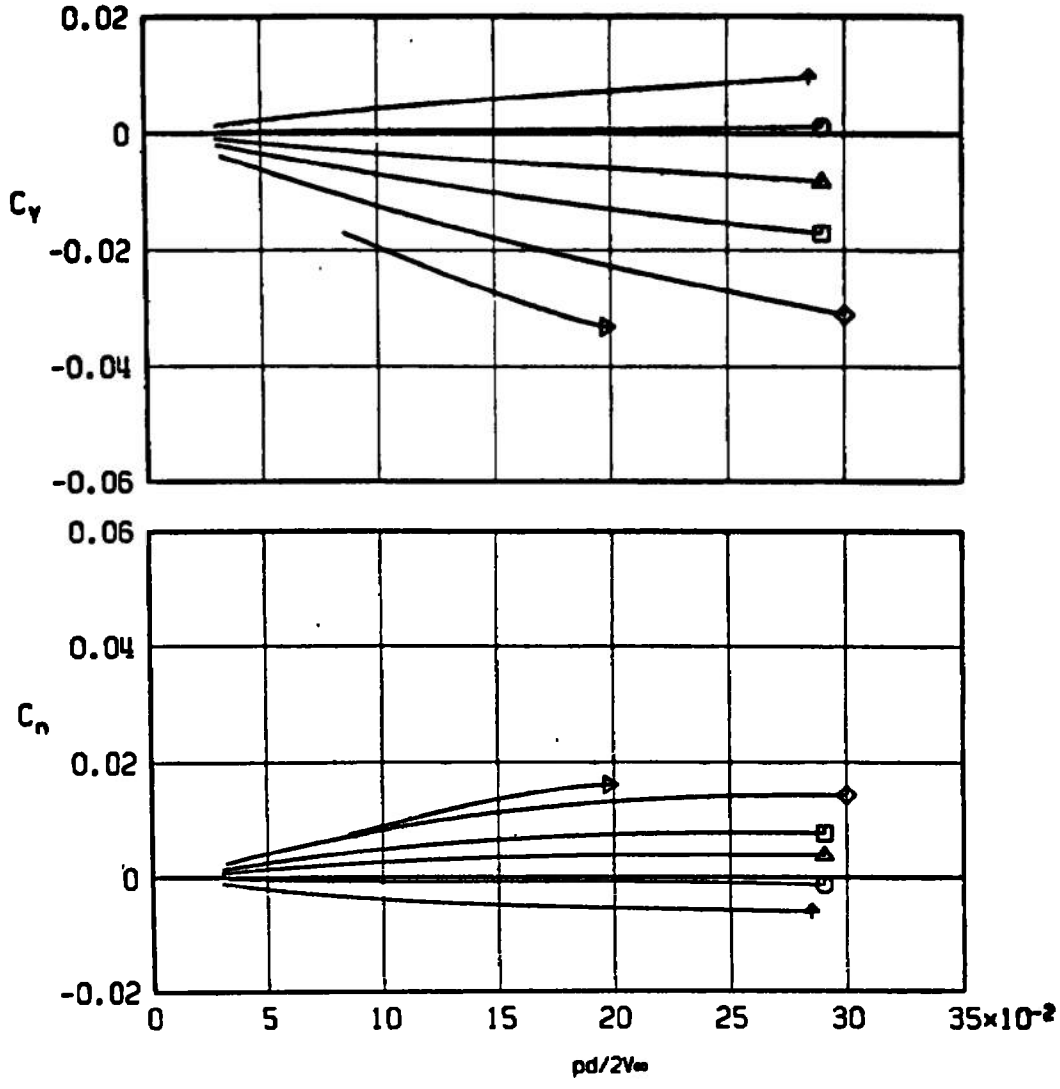

c. $M_\infty = 1.1$
Fig. 14 Continued

Sym	α, deg
↑	-2.07
○	0.00
△	2.08
□	4.15
◇	6.23
▷	8.31

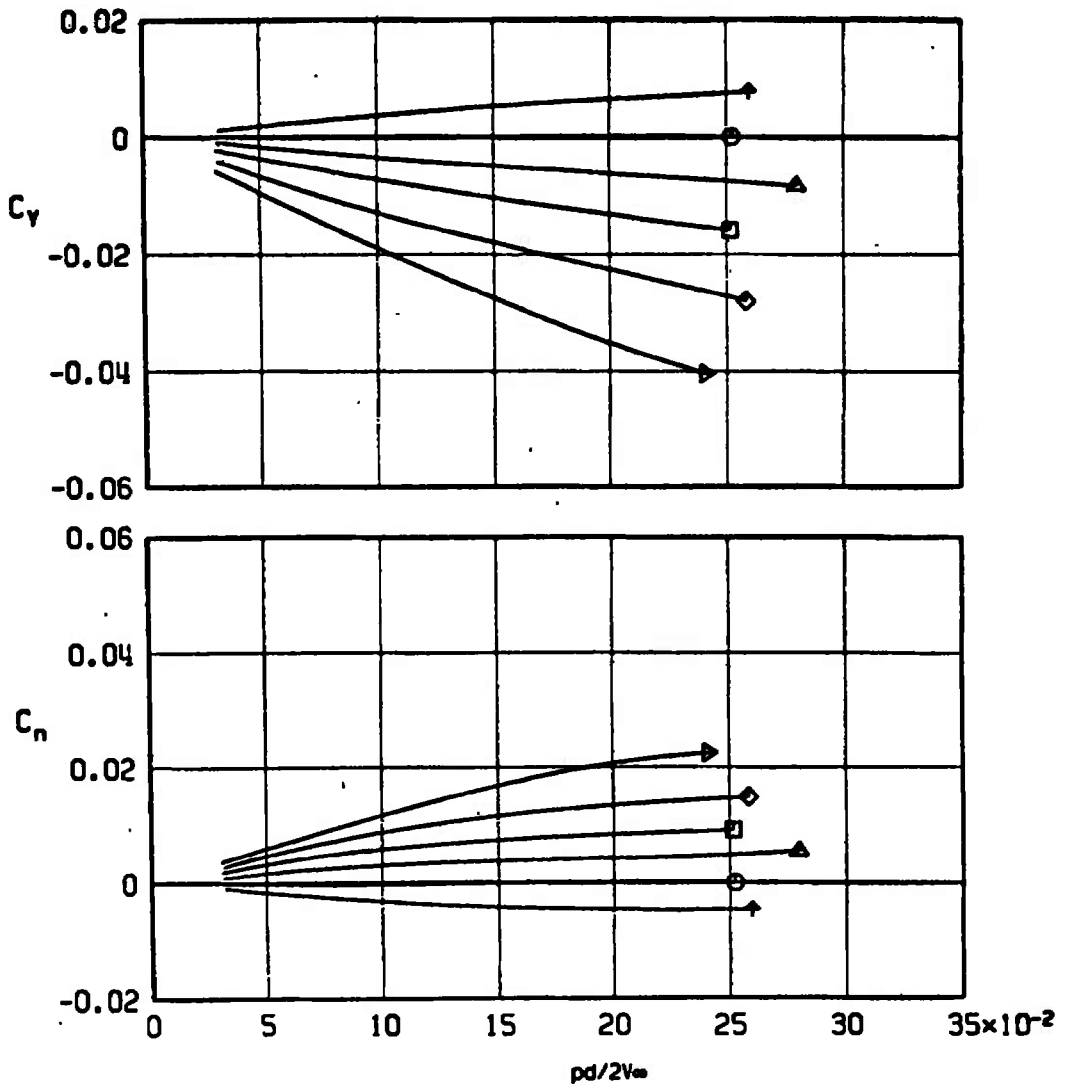

d. $M_\infty = 1.2$

Fig. 14 Continued

Sym	α, deg
□	4.16
▷	8.32

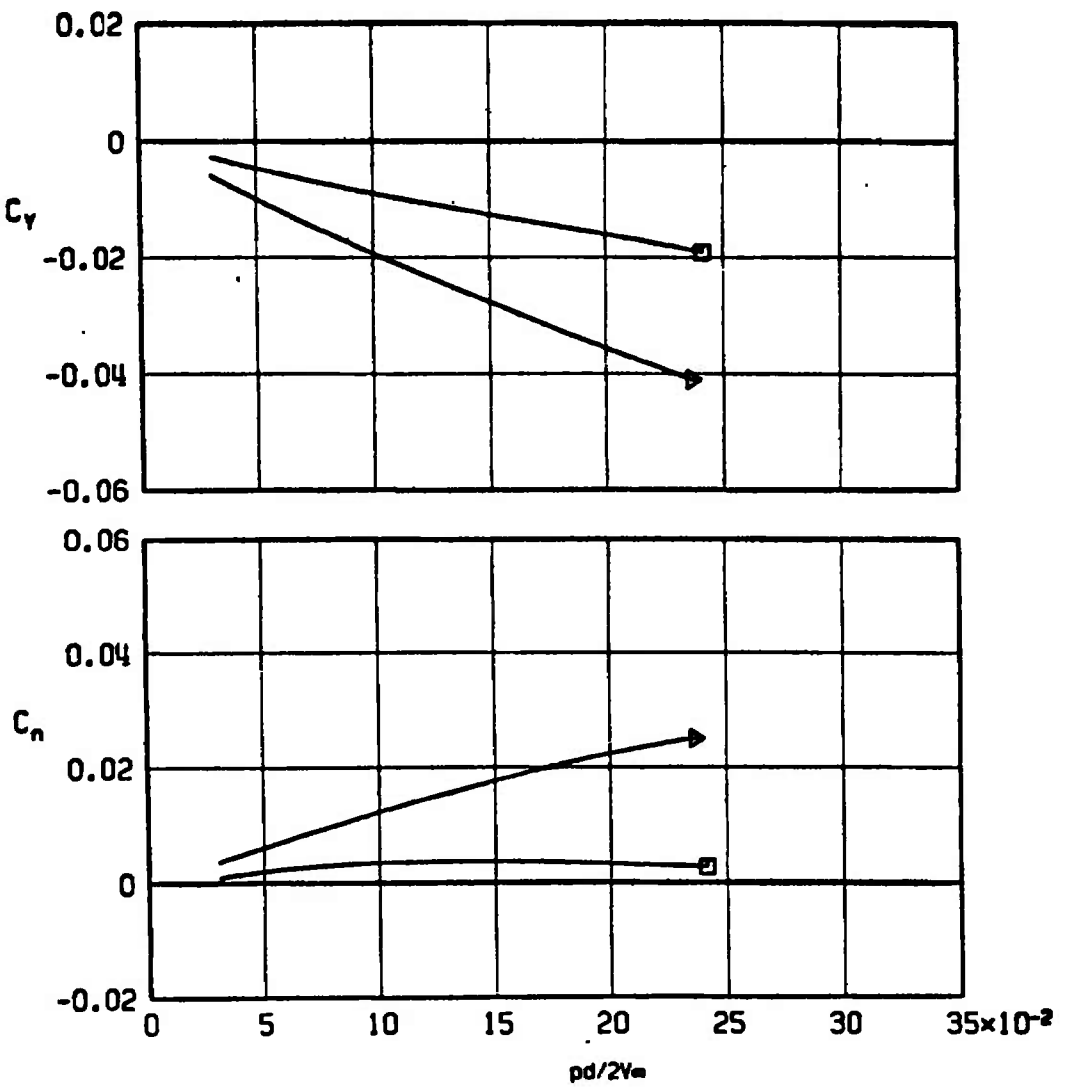

e. M_∞ = 1.3

Fig. 14 Concluded

Sym	α, deg
↑	-2.06
○	0.00
△	2.06
□	4.09
◇	6.18
▷	8.26

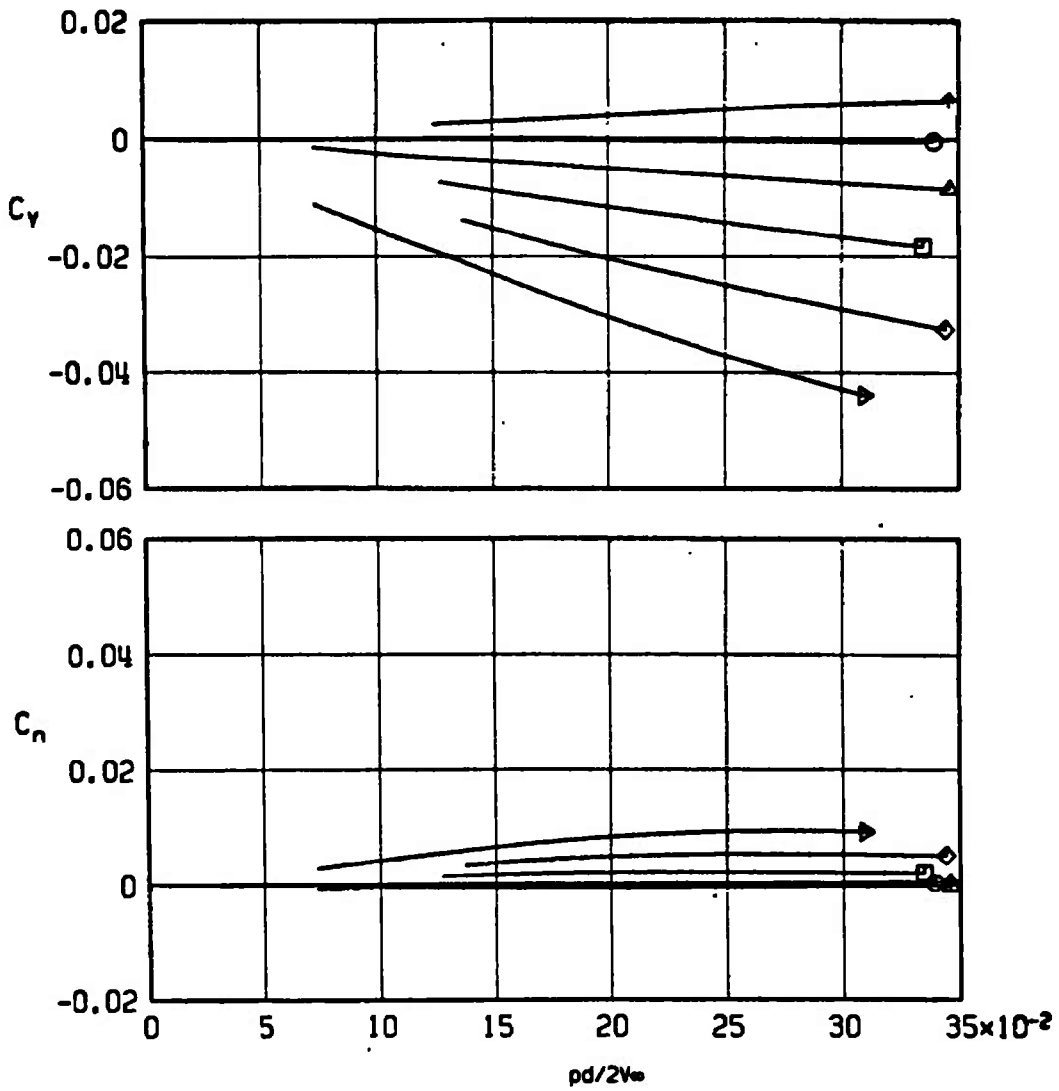

a. $M_\infty = 0.7$

Fig. 15 Variation of C_Y and C_n with $pd/2V_\infty$ for Configuration 2 with Eight Canted Vanes

Sym	α, deg
↑	-2.05
○	0.00
△	2.06
□	4.11
◇	6.16
▷	8.24

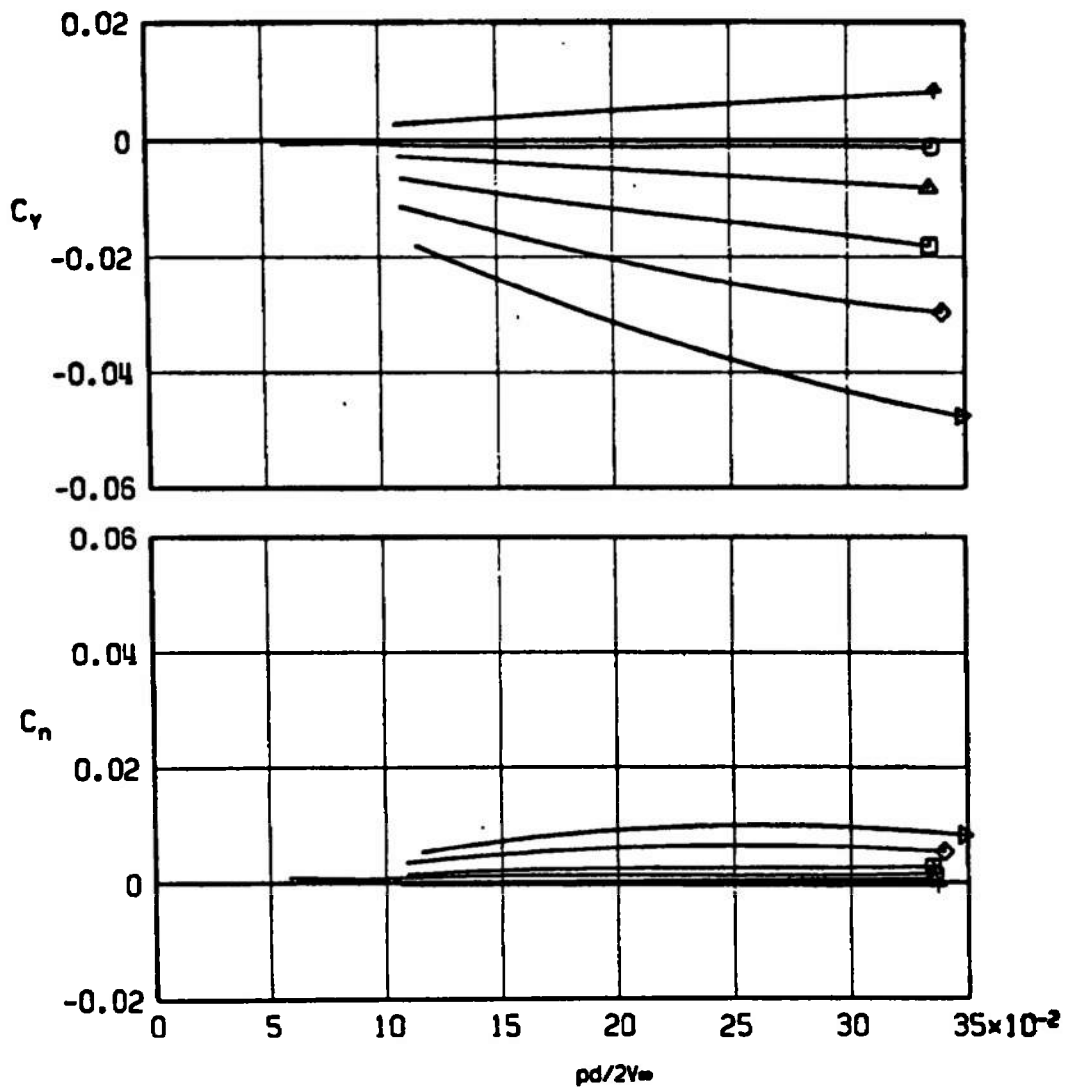

b. $M_\infty = 0.9$
Fig. 15 Continued

Sym	α, deg
↑	-2.05
⊙	0.00
△	2.05

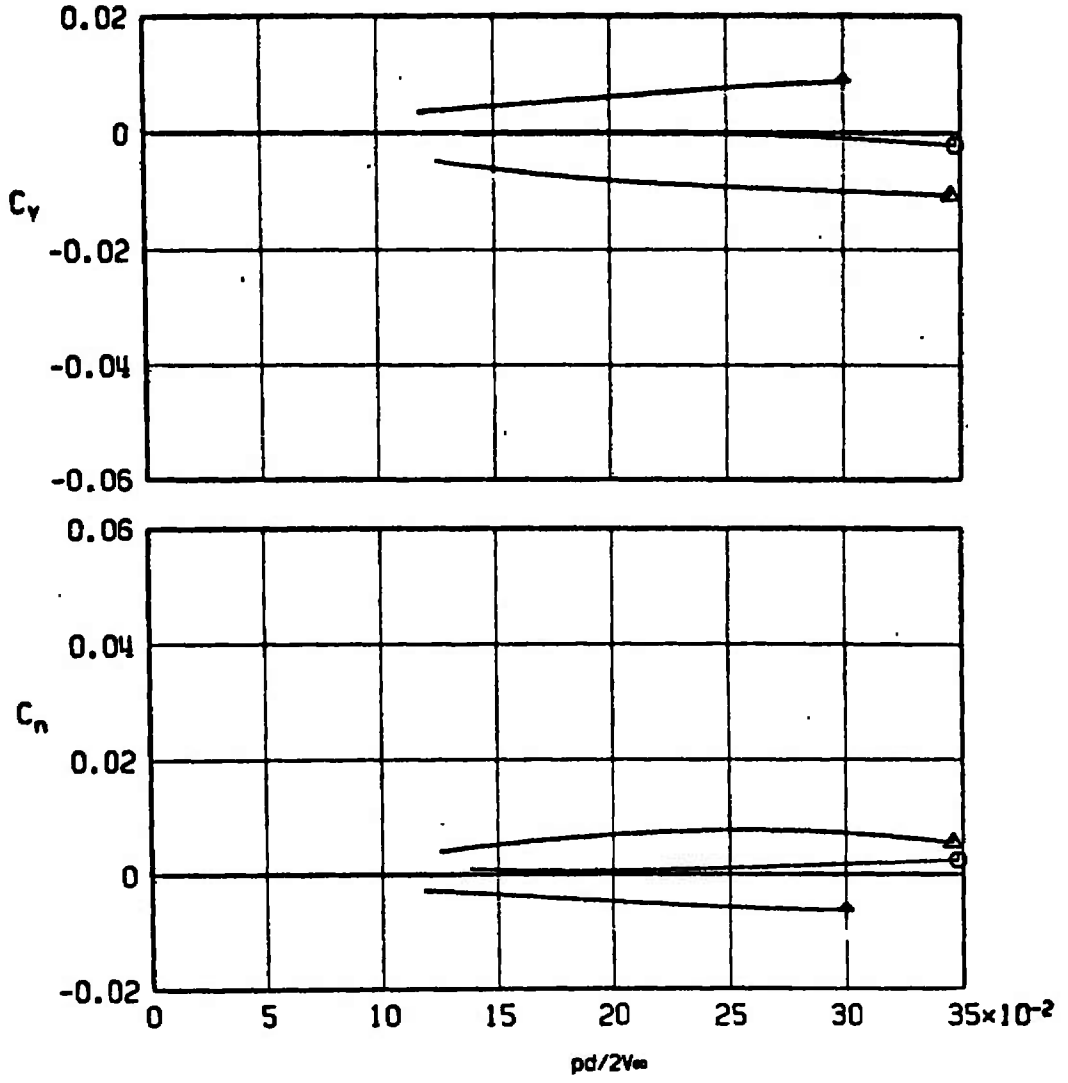

c. $M_\infty = 1.0$
Fig. 15 Continued

Sym	α, deg
↑	-2.05
○	0.00
△	2.06
□	4.12
◇	6.19
▷	8.26

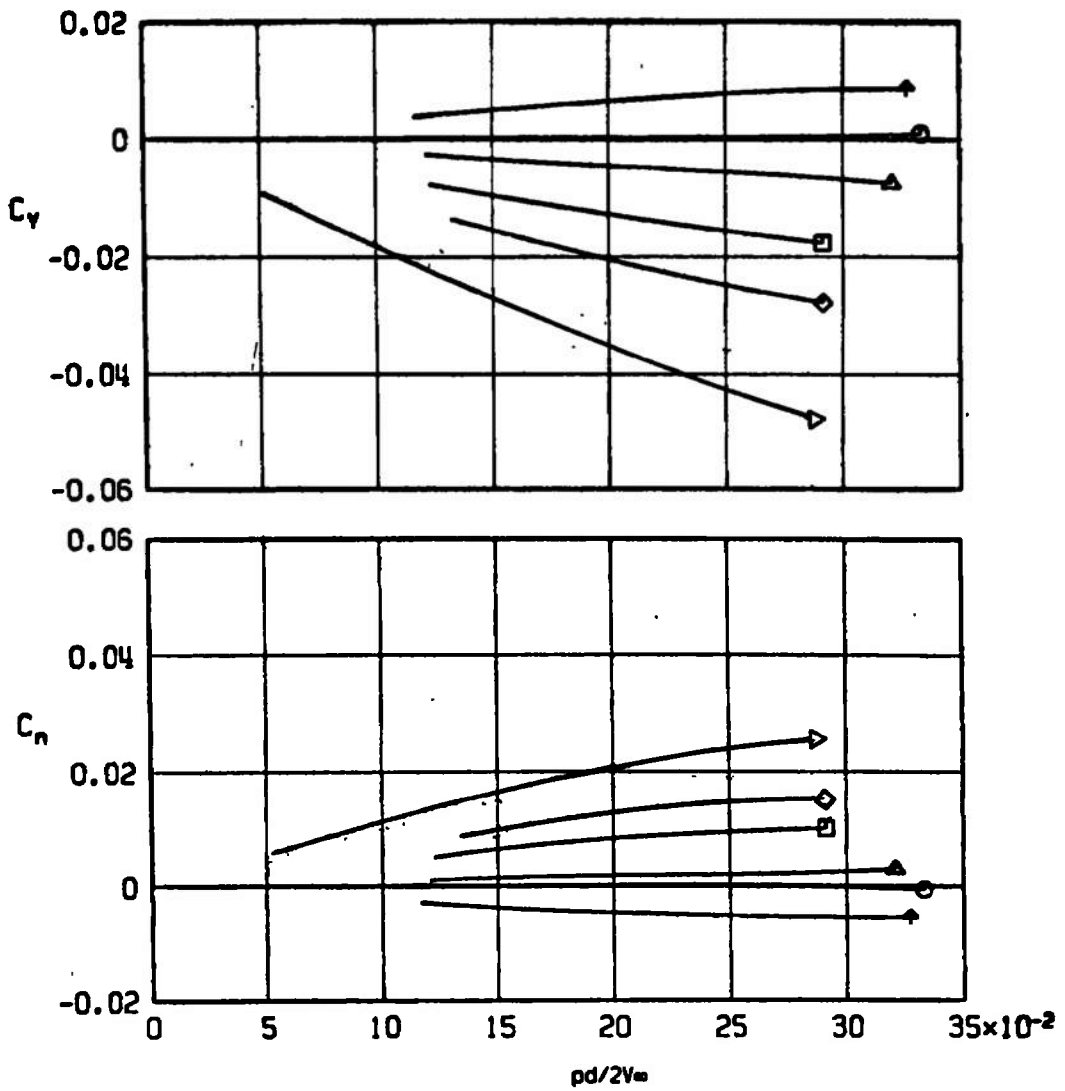

d. $M_\infty = 1.1$
Fig. 15 Continued

Sym	α, deg
↑	-2.05
○	0.00
△	2.04
□	4.12
◇	6.20
▷	8.28

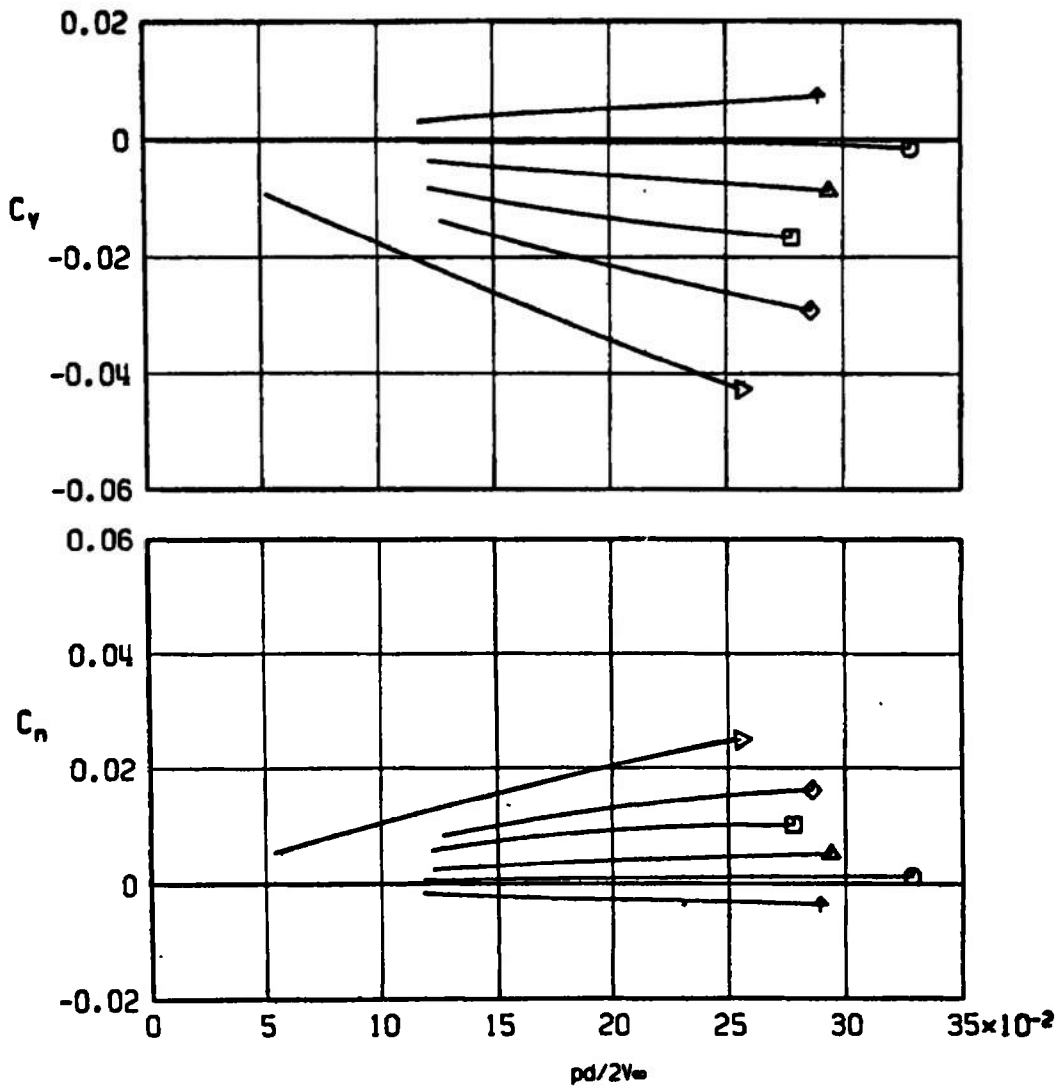

e. $M_\infty = 1.2$

Fig. 15 Continued

Sym	α, deg
◆	-2.06
○	0.00
△	2.06
□	4.13
◇	6.20
▷	8.28

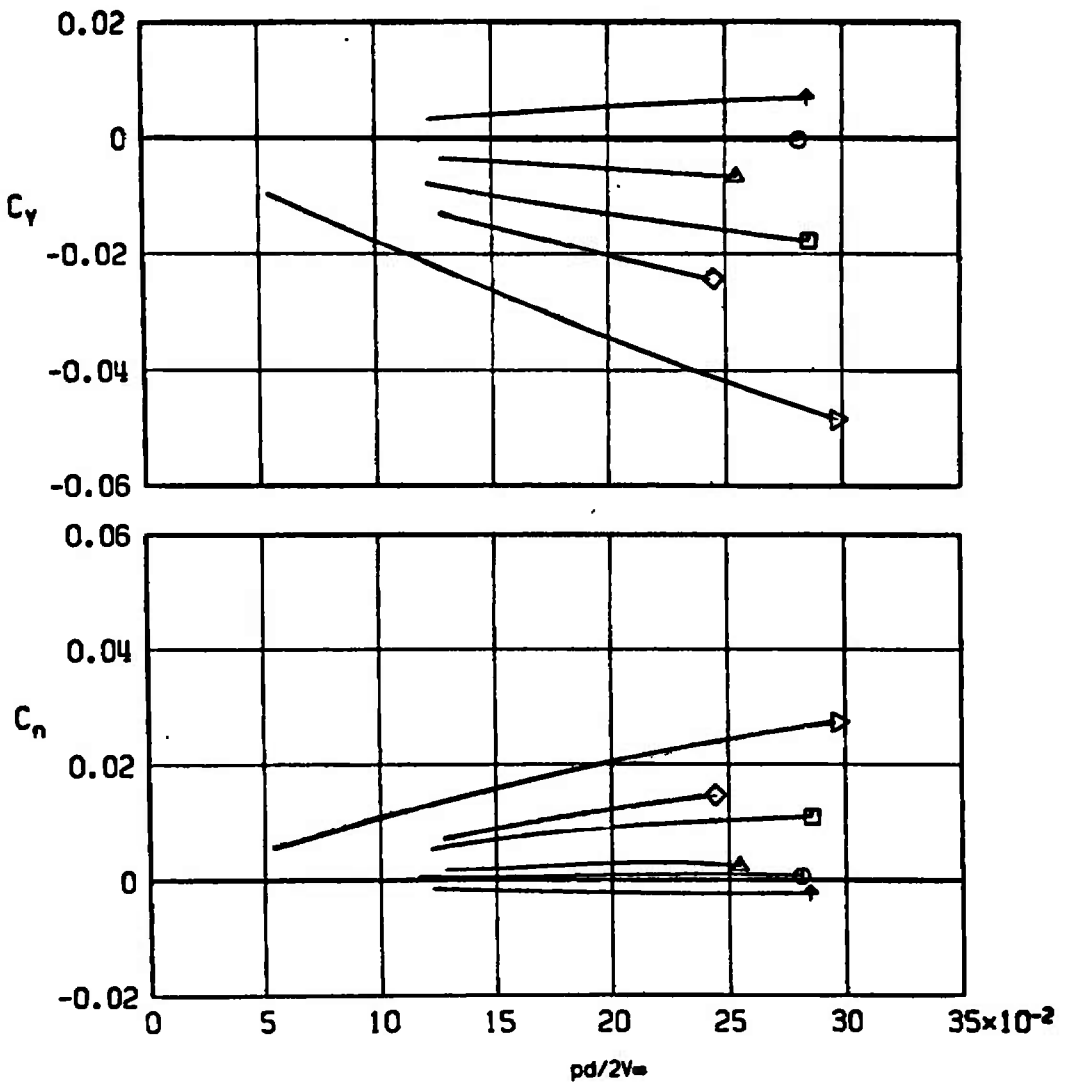

f. $M_\infty = 1.3$

Fig. 15 Concluded

Sym	α, deg
↑	-2.06
○	0.00
△	2.05
□	4.11
◇	6.17
▷	8.22

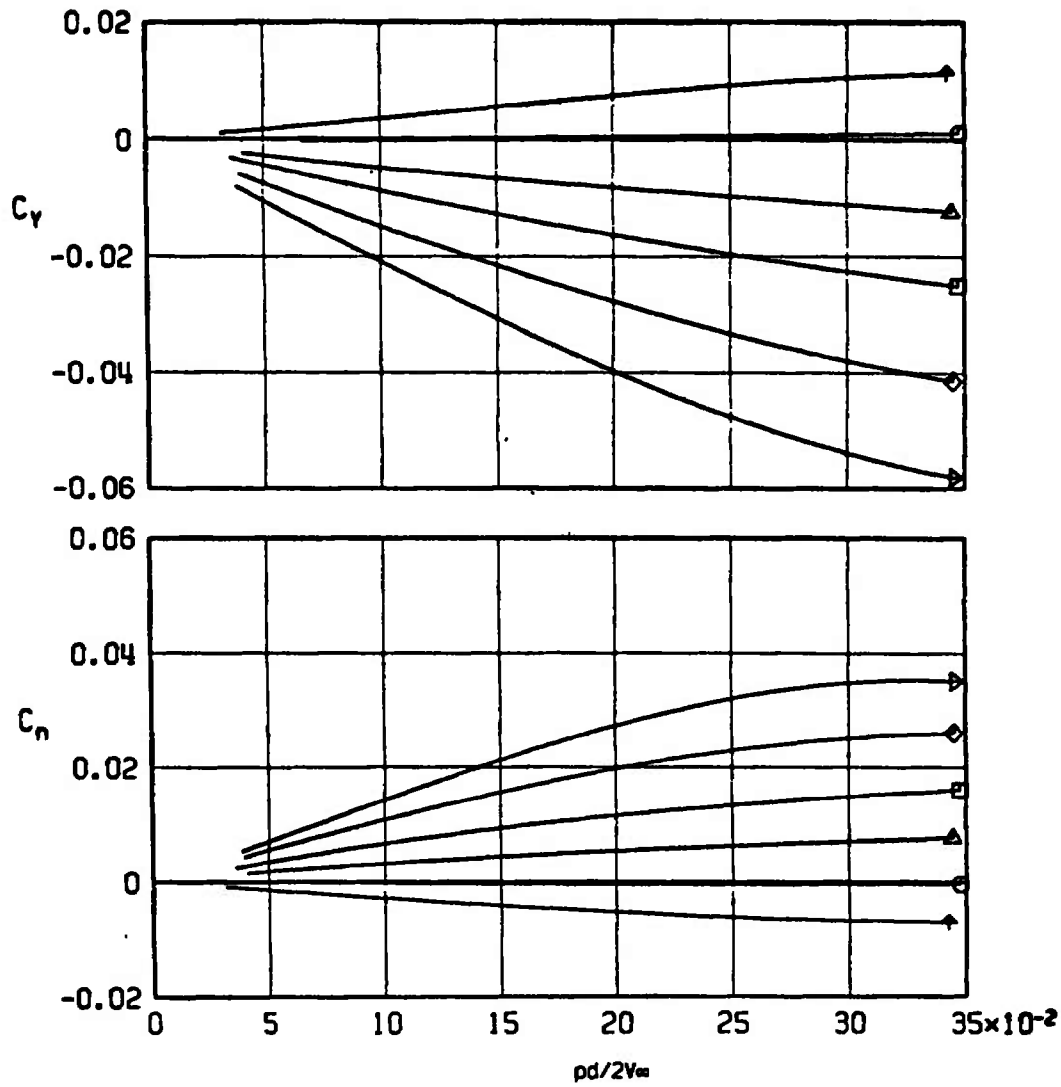

a. $M_\infty = 0.9$

Fig. 16 Variation of C_Y and C_n with $pd/2V_\infty$ for Configuration 3 without Vanes

Sym	α, deg
◆	-2.07
○	0.00
△	2.08
□	4.15
▷	8.28

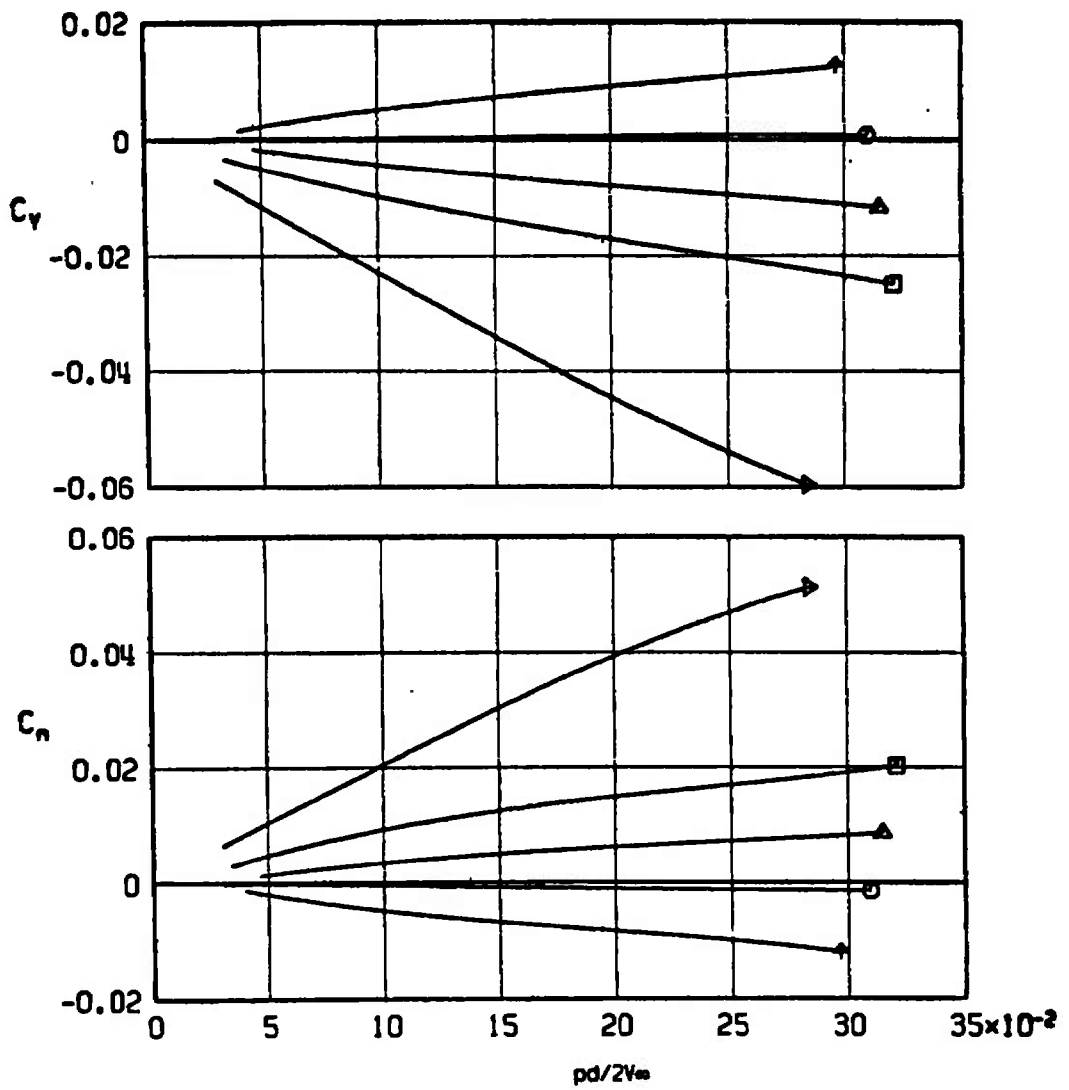

b. $M_\infty = 1.2$
Fig. 16 Continued

Sym	α, deg
▲	-2.07
⊙	0.00
△	2.08
⊡	4.15
◇	6.23
▷	8.30

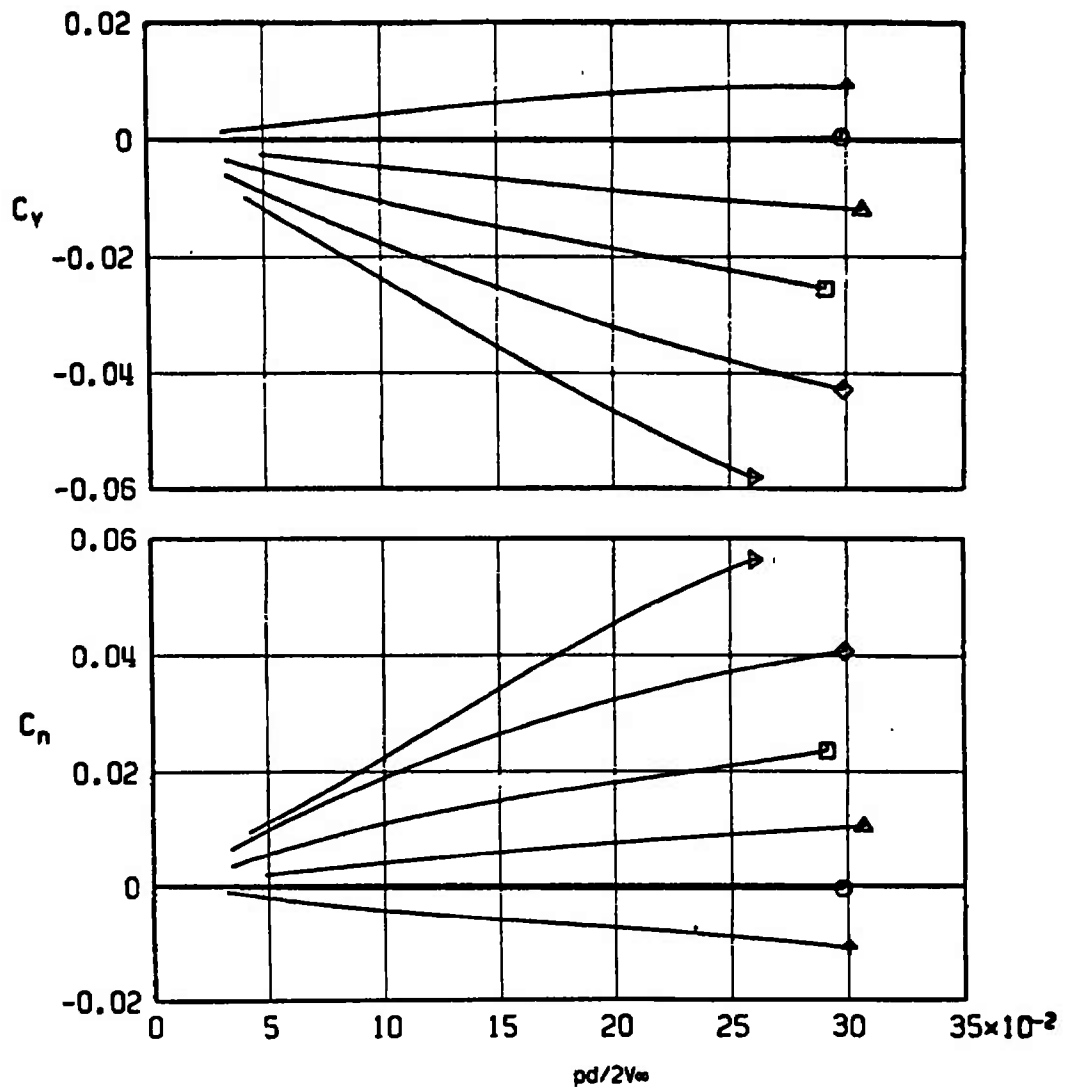

c. $M_\infty = 1.3$

Fig. 16 Concluded

Sym	α, deg
↑	-2.05
○	0.00
△	2.04
□	4.10
◇	6.15
▷	8.20

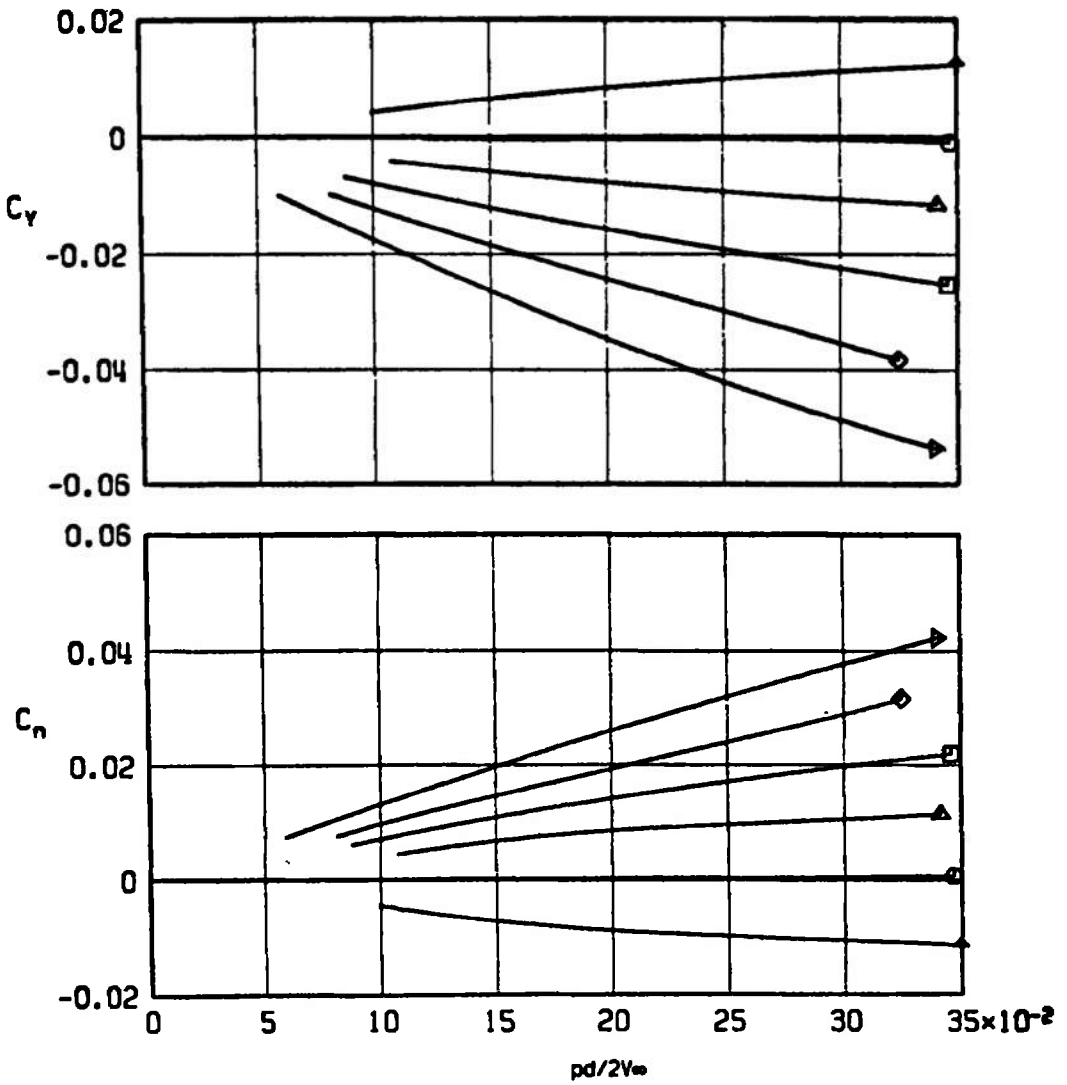

a. $M_\infty = 0.9$

Fig. 17 Variation of C_Y and C_n with $pd/2V_\infty$ for Configuration 3 with Eight Canted Vanes

Sym	α, deg
↑	-2.05
◇	6.14
▷	8.23

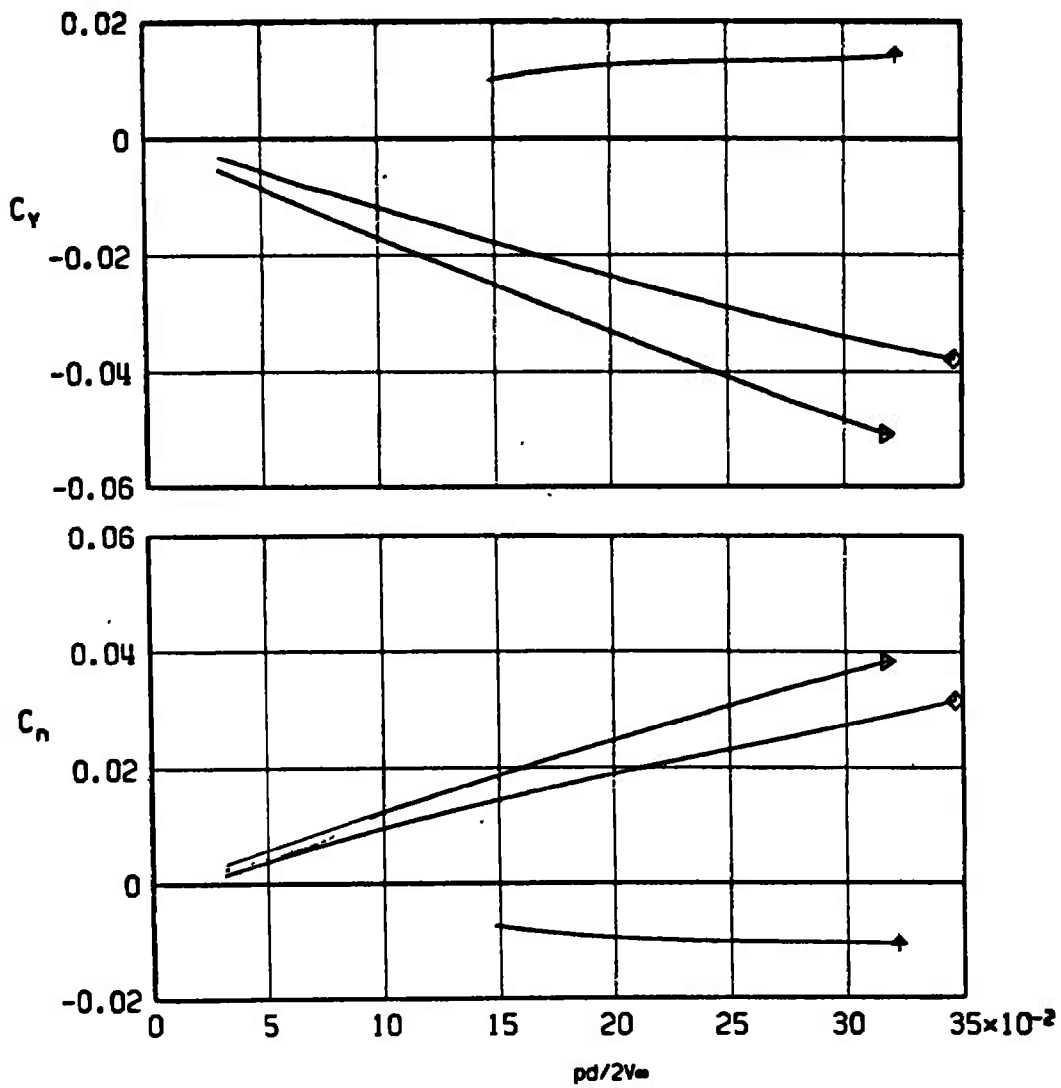

b. $M_\infty = 1.0$
Fig. 17 Continued

Sym	α, deg
◆	-2.05
○	0.00
△	2.04
□	4.09
◇	6.17
▷	8.22

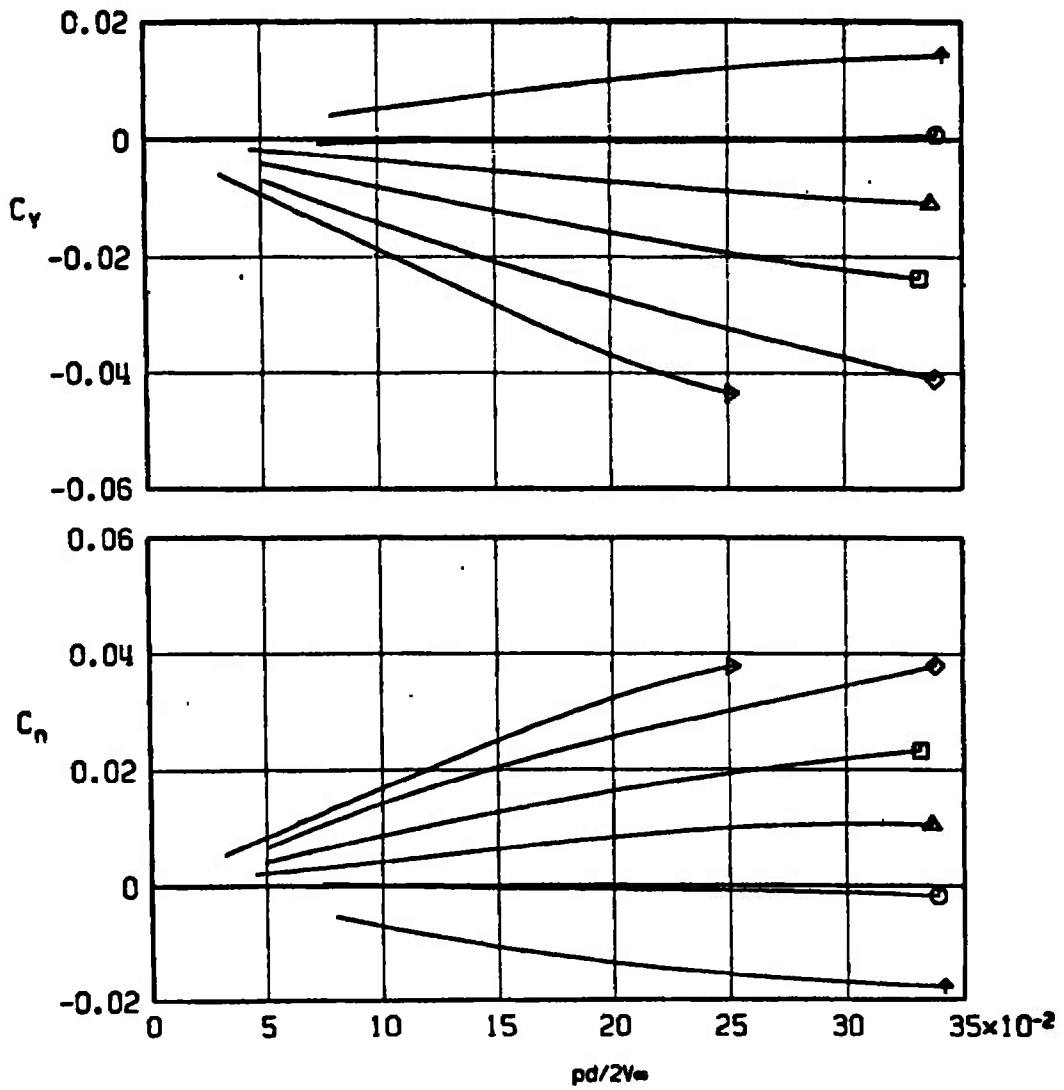

c. $M_\infty = 1.1$
Fig. 17 Continued

Sym	α, deg
↑	-2.04
○	0.00
△	2.06
□	4.14
◇	6.20
▷	8.26

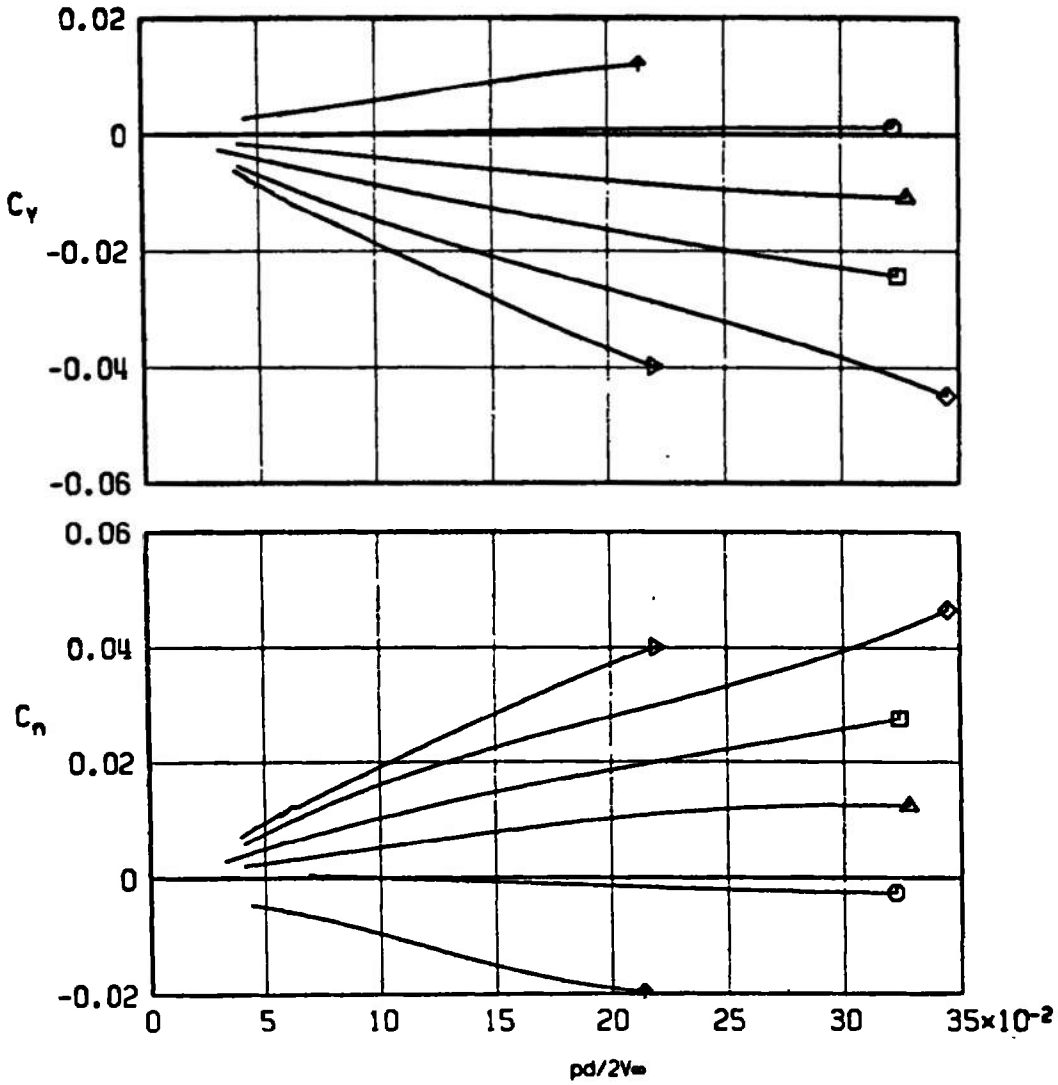

d. $M_\infty = 1.2$

Fig. 17 Continued

Sym	α, deg
↑	-2.04
○	0.00
△	2.09
□	4.14
◇	6.21
▷	8.26

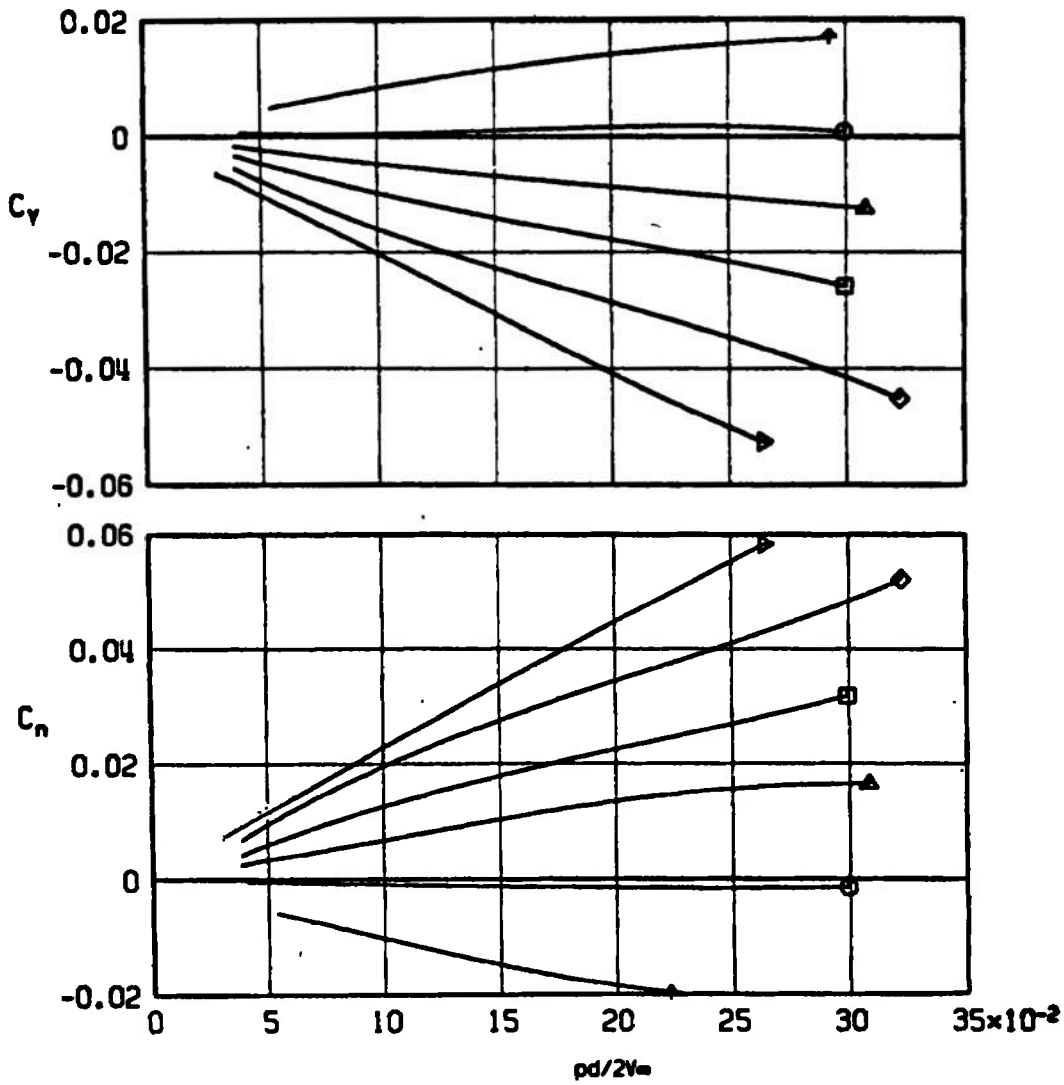

e. $M_\infty = 1.3$

Fig. 17 Concluded

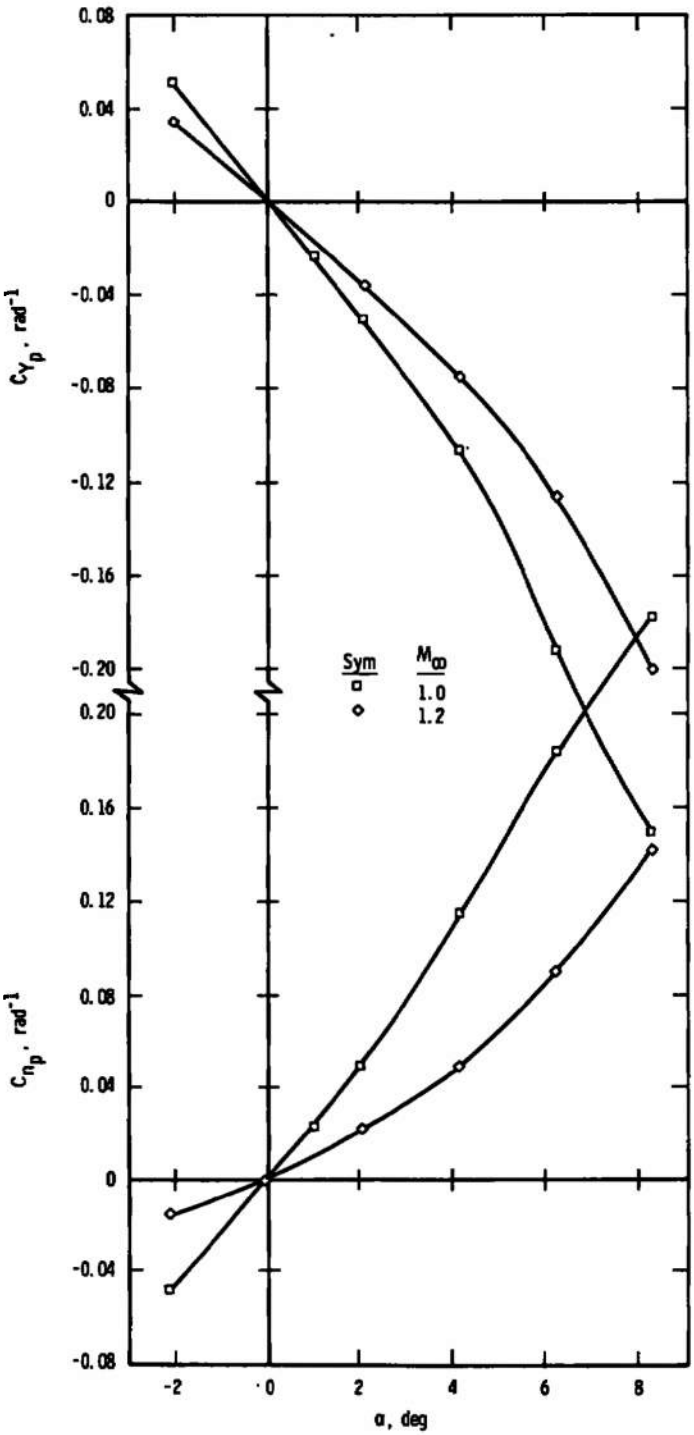

a. Without Vanes

Fig. 18 Variation of C_{Y_p} and C_{n_p} with Angle of Attack for Configuration 0

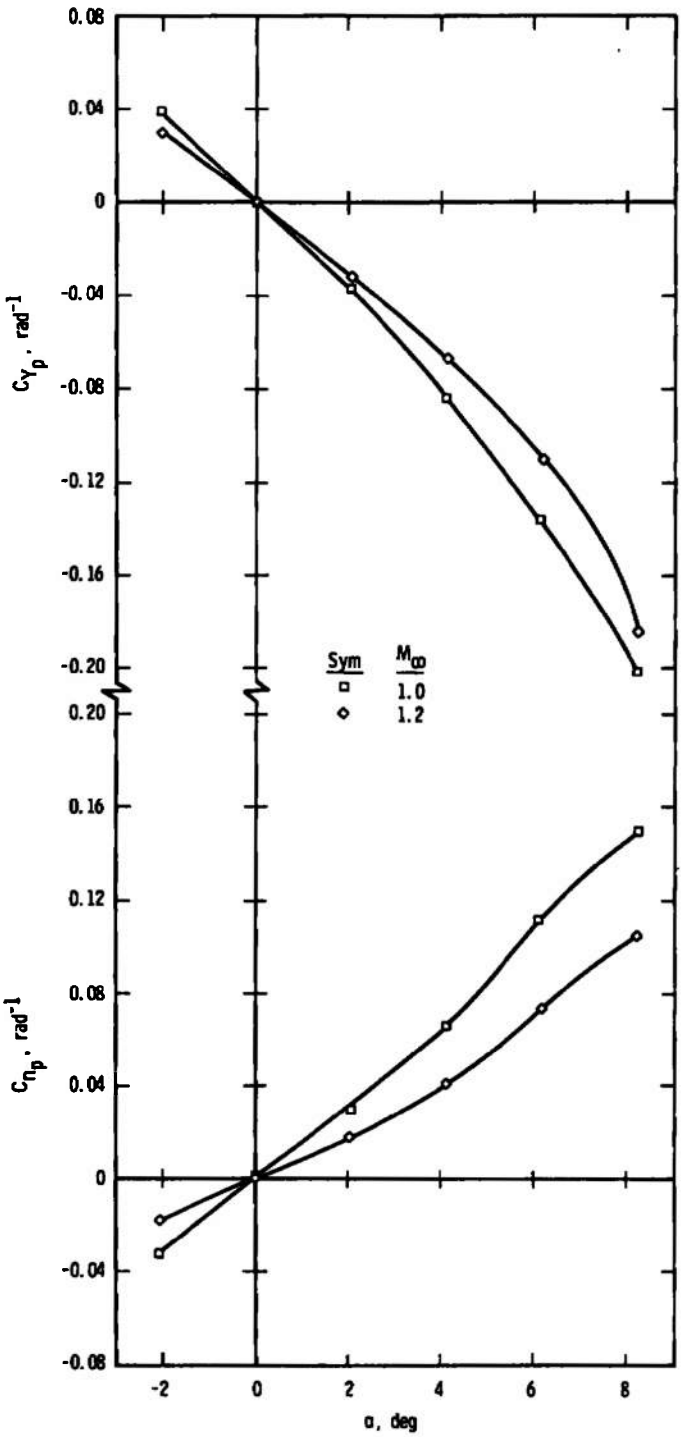

b. With Four Canted Vanes
Fig. 18 Continued

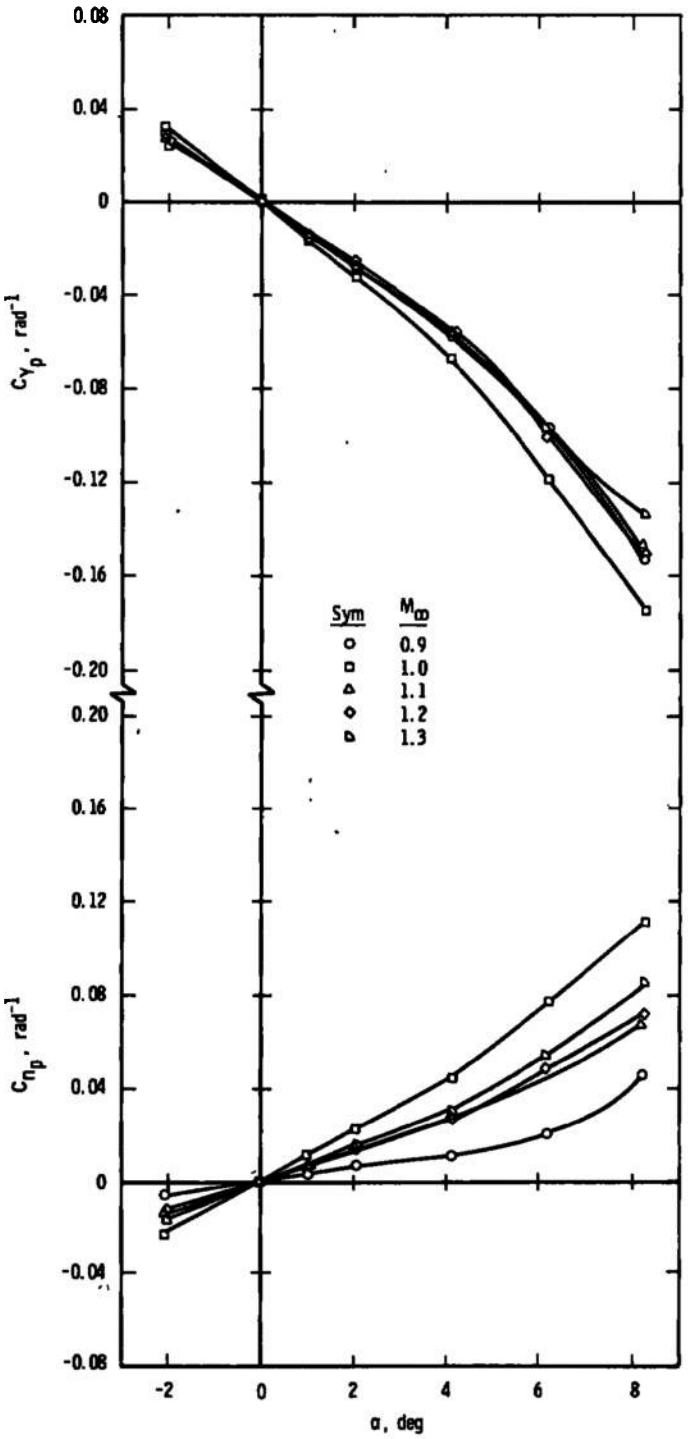

c. With Eight Straight Vanes
Fig. 18 Continued

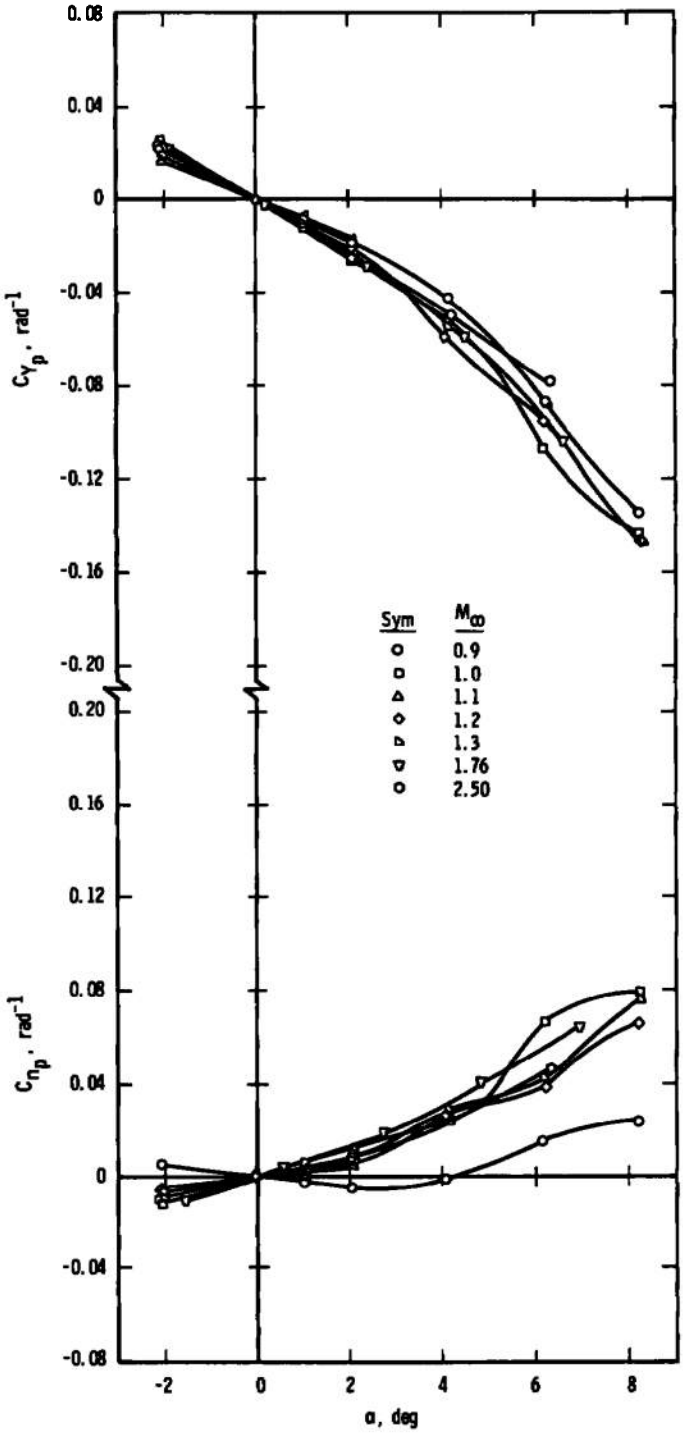

d. With Eight Canted Vanes
Fig. 18 Concluded

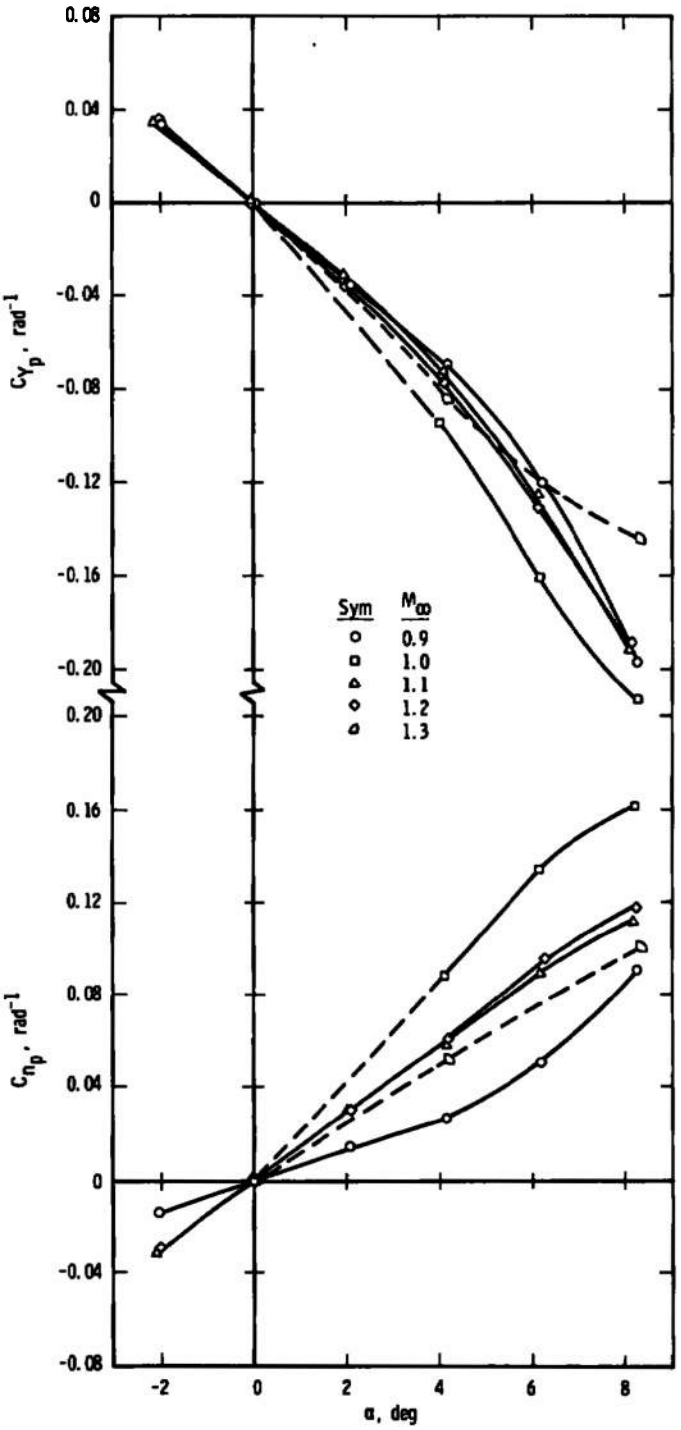

a. With Eight Straight Vanes

Fig. 19 Variation of C_{Y_p} and C_{n_p} with Angle of Attack for Configuration 2

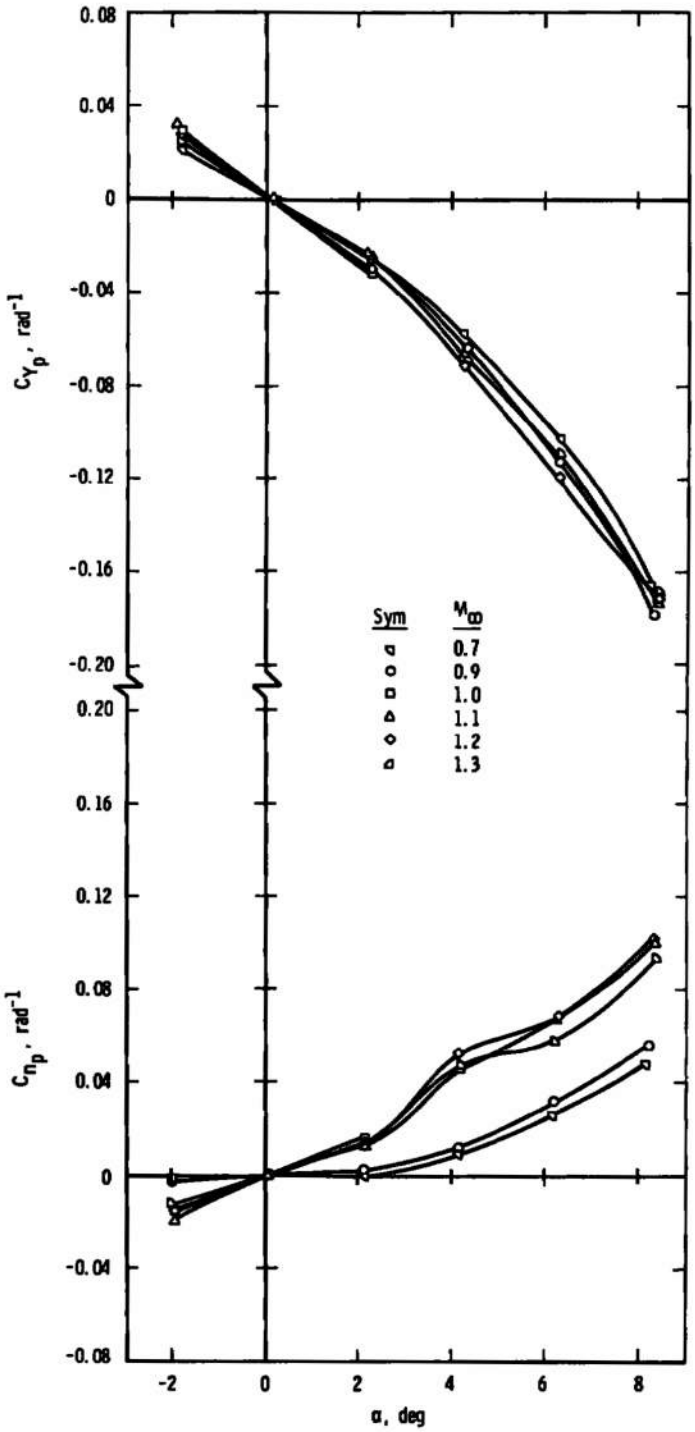

b. With Eight Canted Vanes
Fig. 19 Concluded

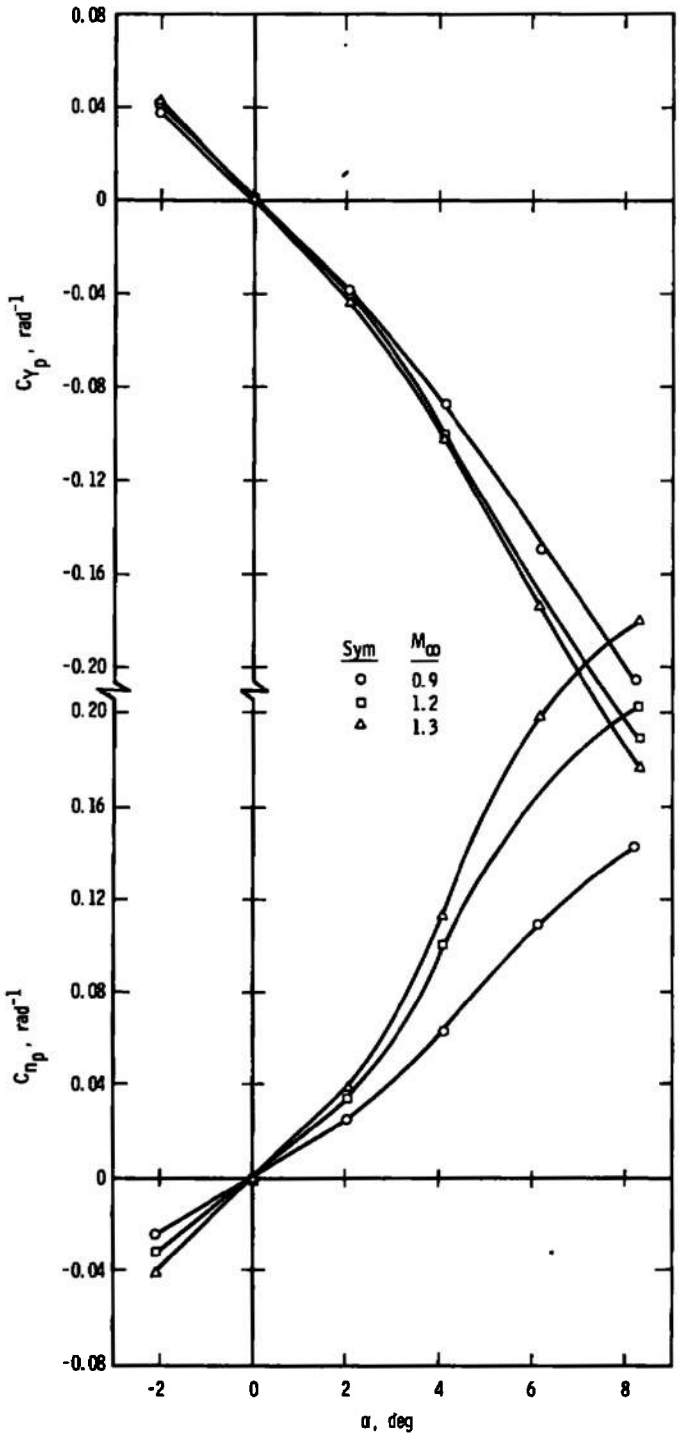

a. Without Vanes

Fig. 20 Variation of C_{Y_p} and C_{n_p} with Angle of Attack for Configuration 3

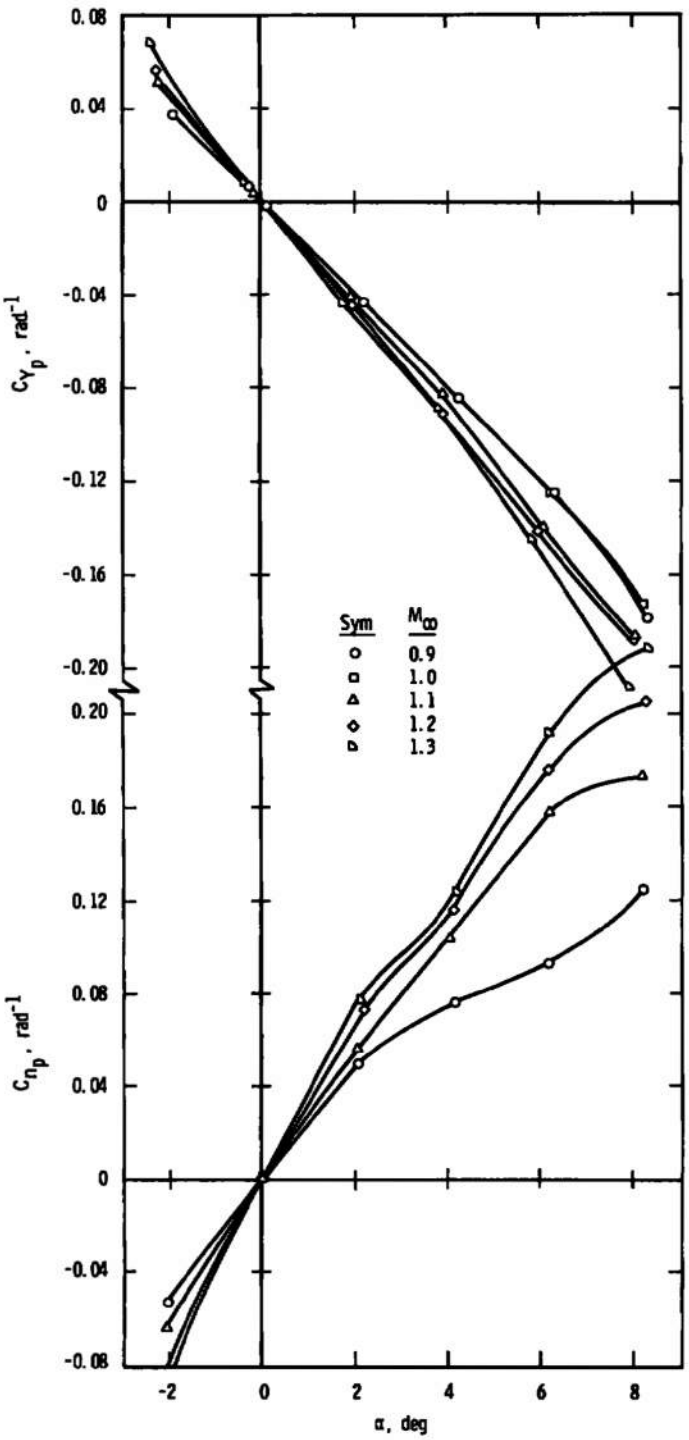

b. With Eight Canted Vanes
Fig. 20 Concluded

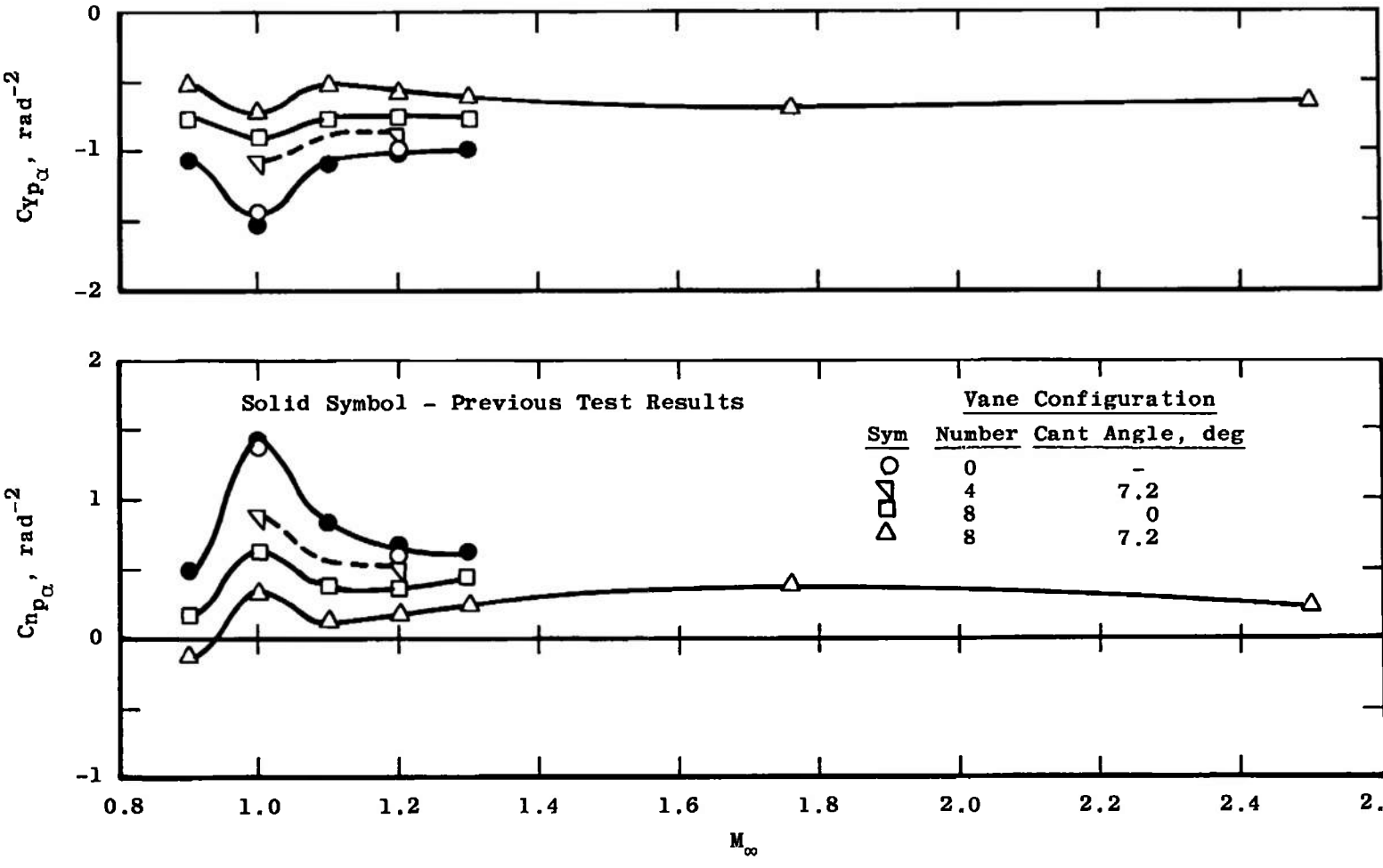

a. Configuration 0

Fig. 21 Variation of $C_{Y_{p_\alpha}}$ and $C_{n_{p_\alpha}}$ with Mach Number

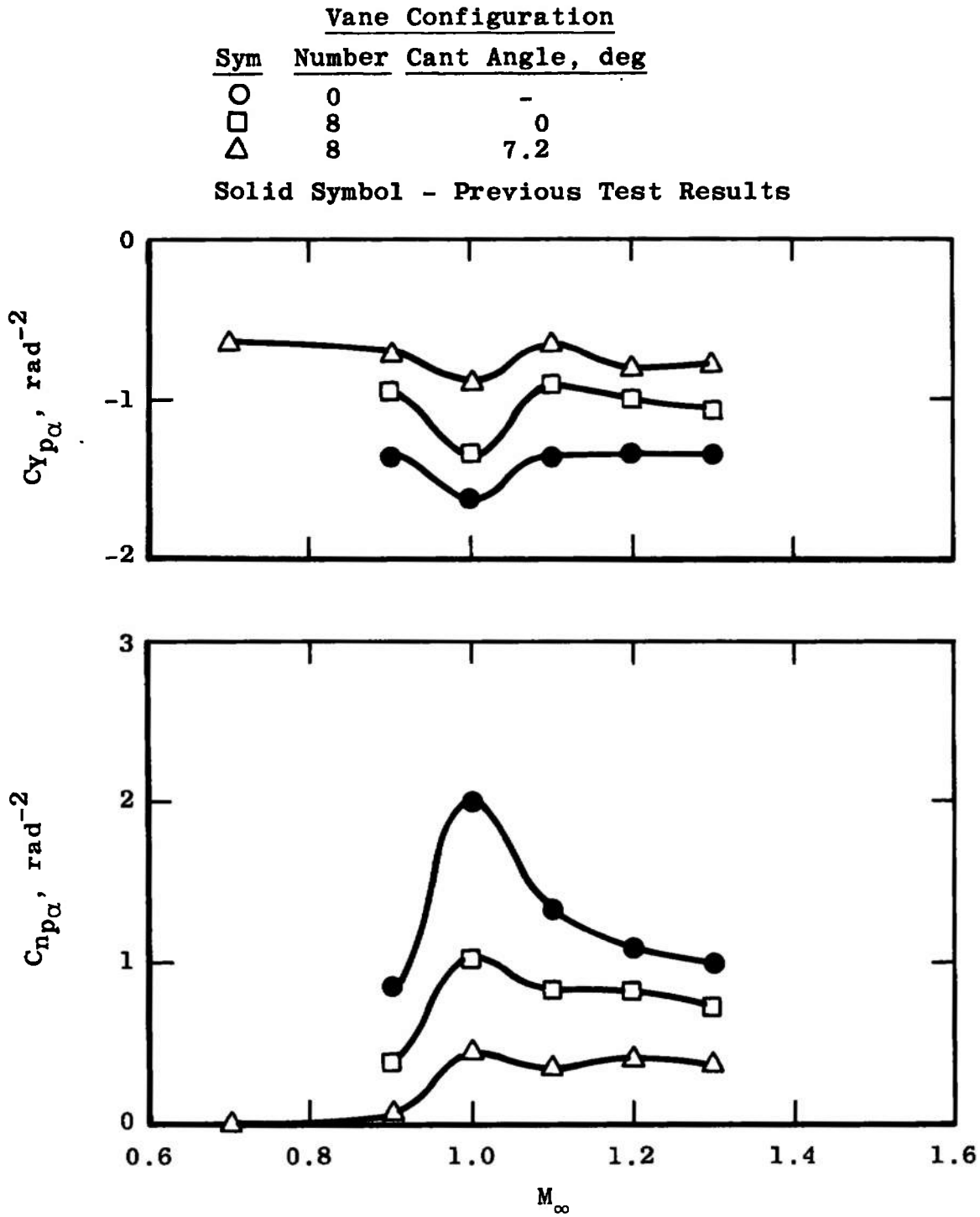

b. Configuration 2
Fig. 21 Continued

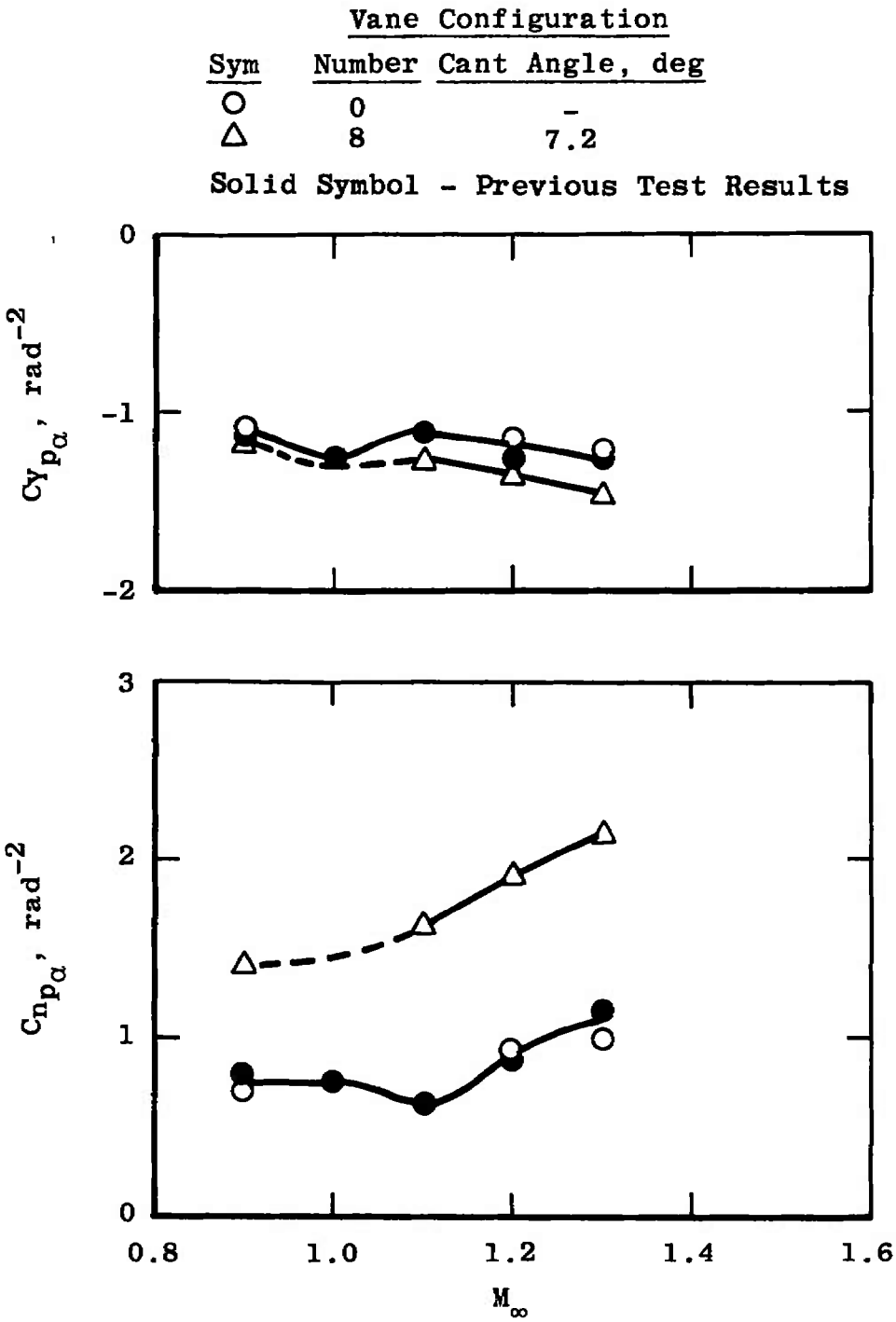

c. Configuration 3
Fig. 21 Concluded

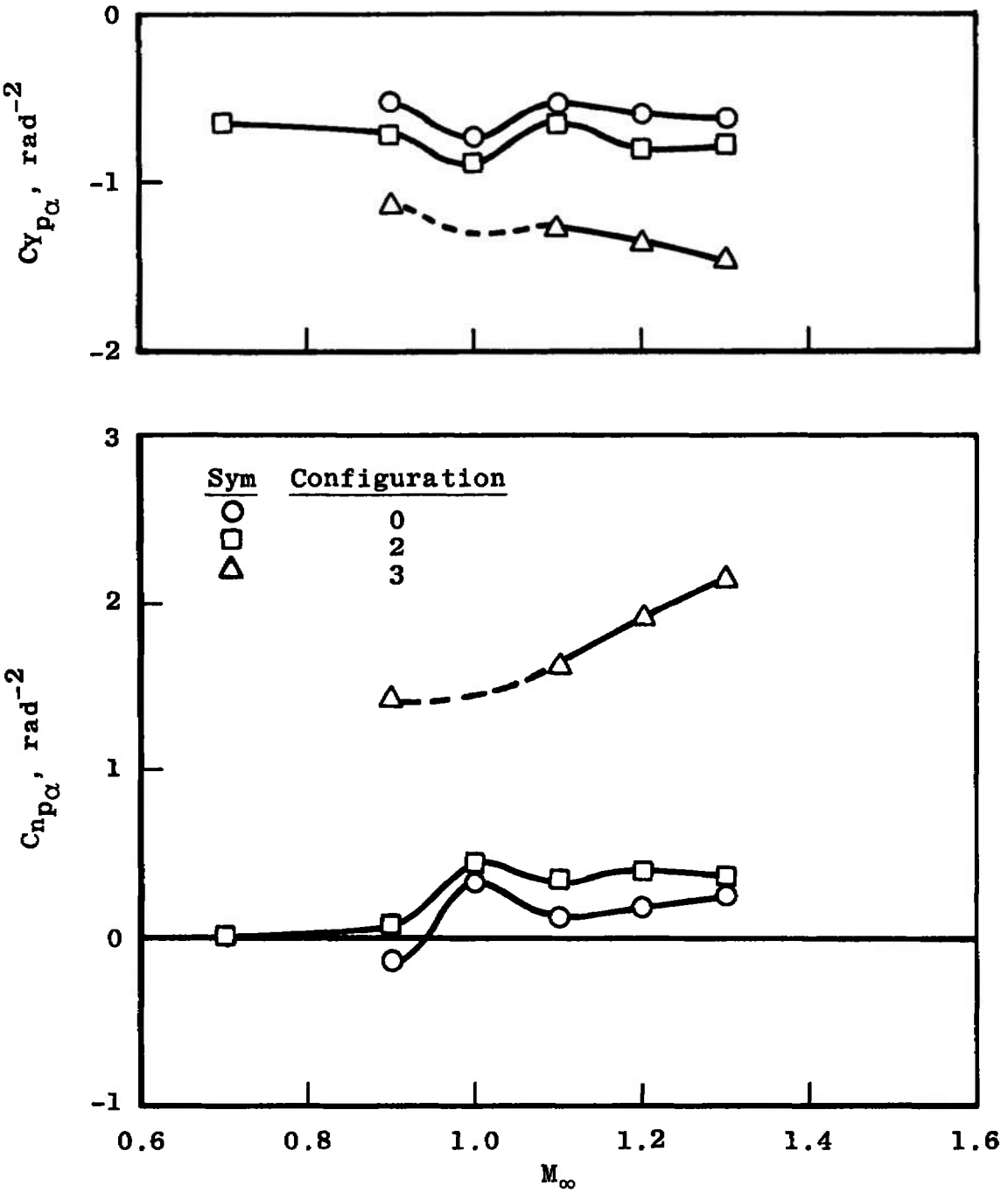

Fig. 22 Comparison of the Variation of $C_{Y_{p_\alpha}}$ and $C_{n_{p_\alpha}}$ with Mach Number for Configurations with Eight Canted Vanes

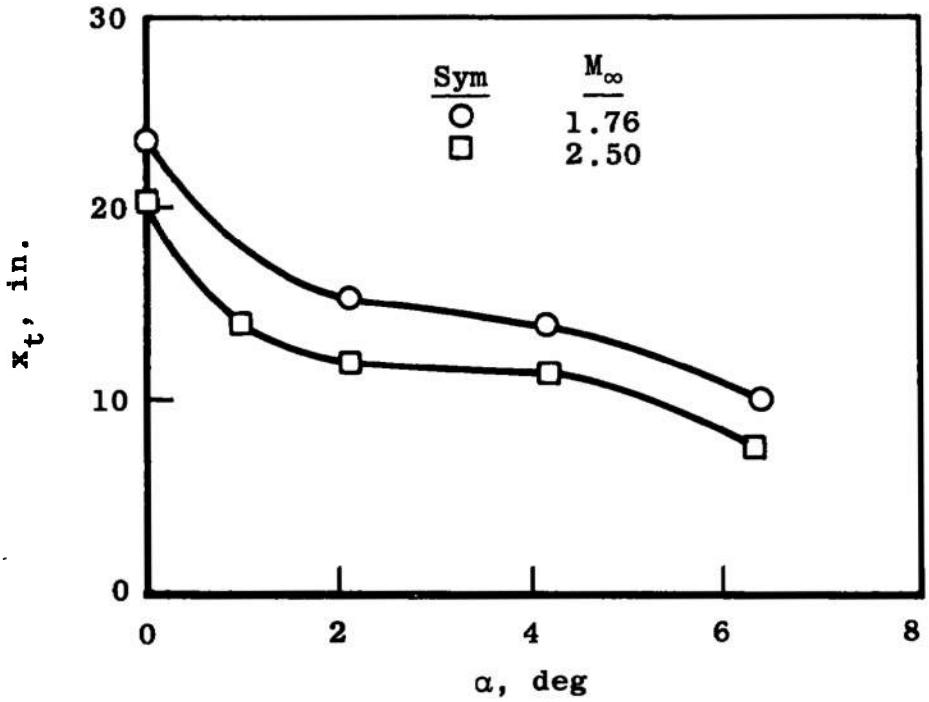

Fig. 23 Onset of Transition on the Leeward Surface of Configuration 0 at Supersonic Mach Numbers in Tunnel A

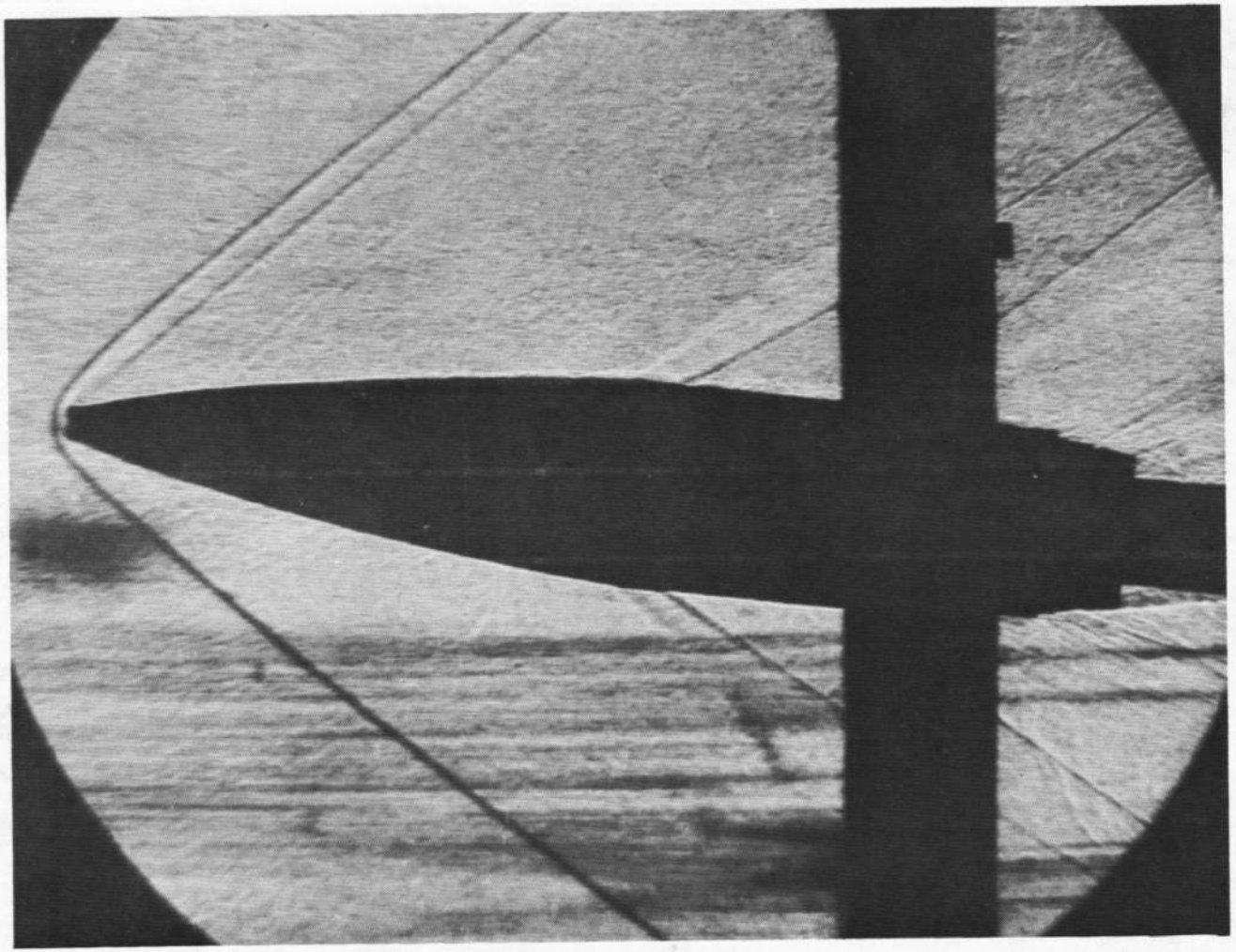

Fig. 24 Typical Shadowgraph of Configuration 0 at M_∞ = 1.76, α = 6.37 (Tunnel A)

UNCLASSIFIED

Security Classification

DOCUMENT CONTROL DATA - R & D

(Security classification of title, body of abstract and indexing annotation must be entered when the overall report is classified)

1 ORIGINATING ACTIVITY (Corporate author)	2a. REPORT SECURITY CLASSIFICATION
Arnold Engineering Development Center Arnold Air Force Station, Tennessee 37389	UNCLASSIFIED
	2b. GROUP N/A

3 REPORT TITLE

EXPERIMENTAL MAGNUS CHARACTERISTICS OF BALLISTIC PROJECTILES WITH ANTI-MAGNUS VANES AT MACH NUMBERS 0.7 THROUGH 2.5

4 DESCRIPTIVE NOTES (Type of report and inclusive dates)

Final Report - February 26 through March 15, 1973

5. AUTHOR(S) (First name, middle initial, last name)

Leroy M. Jenke and Jack B. Carman, ARO, Inc.

6 REPORT DATE	7a. TOTAL NO. OF PAGES	7b. NO. OF REFS
December 1973	94	3

8a. CONTRACT OR GRANT NO.	8a. ORIGINATOR'S REPORT NUMBER(S)
b. PROJECT NO 2547	AEDC-TR-73-126 AFATL-TR-73-150
c. Program Element 62602F	9b. OTHER REPORT NO(S) (Any other numbers that may be assigned this report)
d.	ARO-PWT-TR-73-64

10 DISTRIBUTION STATEMENT

Approved for public release; distribution unlimited.

11 SUPPLEMENTARY NOTES	12. SPONSORING MILITARY ACTIVITY
Available in DDC.	Air Force Armament Laboratory (DLDL), Eglin AFB, FL 32542

13. ABSTRACT An experimental investigation was conducted to determine static-stability and Magnus characteristics of three spin-stabilized ballistic shell configurations with small anti-Magnus vanes on the boattail. The models (slightly larger than full scale) were tested at Mach numbers 0.7 through 2.5 over an angle-of-attack range from -2 to 8 deg. The Reynolds number, based on a model diameter of 5.2 in., was 1×10^6 (for $M_\infty = 0.7$ to 1.3) and 1.7×10^6 (for $M_\infty = 1.76$ to 2.5), and the spin parameter ($pd/2V_\infty$) ranged from 0 to 0.4 radians. Results are presented showing the effects of spin, Mach number, angle of attack, and anti-Magnus vanes. These results show that the vanes were effective in reducing both Magnus force and moment for two of the basic configurations and that the canted (7.2-deg) vanes were more effective than the straight vanes.

DD FORM 1 NOV 65 1473

UNCLASSIFIED

Security Classification

UNCLASSIFIED

Security Classification

14. KEY WORDS	LINK A		LINK B		LINK C	
	ROLE	WT	ROLE	WT	ROLE	WT
ballistic trajectories						
spin-stabilized ammunition						
subsonic flow						
supersonic flow						
Magnus effects						
Reynolds number						
angle of attack						
static stability						

1. Projectiles — —

2 " — — Stability

3 " "

4 Antimagnus vanes.

5 " "

AFSC
Arnold AFS Tenn

UNCLASSIFIED

Security Classification